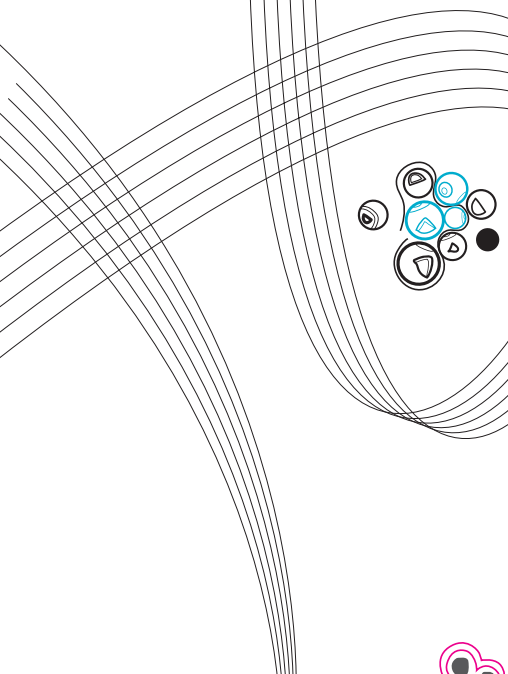


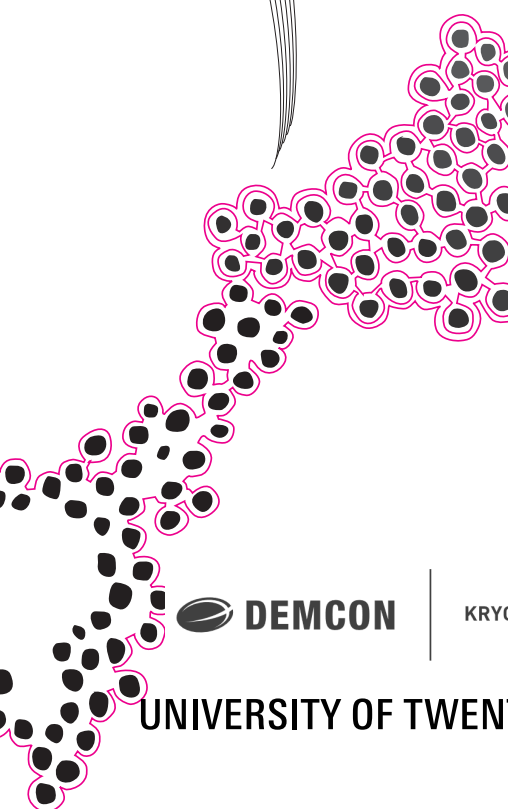
The Design of an In-Orbit Demonstration for a Mini Mechanically Pumped Cooling Loop in a CubeSat

Master Thesis Report

Mick Oude Engberink (S2334240)



Engineering Technology - Thermal and Fluid Engineering
University of Twente
July 2024



This report is the result of a master thesis assignment at Demcon Kryoz in Enschede, lasting from November 2023 to July 2024 (45EC) for the Master Mechanical Engineering.

Student: M. Oude Engberink
Chairman: Prof. Dr. Ing. W. Rohlf's
Internal Member: Dr. M. Mehrali
External Member: Dr. Ir. D. Jafari
Company Supervisor: Ir. G. Giammaria

 **DEMCON**

KRYOZ

UNIVERSITY OF TWENTE.

Acknowledgements

I would like to express my sincere gratitude towards Ir. Guido Giammaria and Prof. Dr. Ing. Wilko Rohlf's for guiding me through my research and for always being available for constructive discussions.

I am thankful towards my colleagues at Demcon Kryoz and in particular Ir. Bart Schepers, Ir. Sander Elvik, and Ir. Mark Arendshorst for being there whenever I needed some experienced guidance to help me overcome obstacles during my research. Additionally, I would like to thank Daan Oude Veldhuis better known as my 'partner in crime' for all the coffee and laughs that we had during the first months of my research.

Appreciation goes out to my mom, my dad, my brother Duuk, my girlfriend Eline and my close friends for their moral support during the entirety of the research, especially when I needed to get my mind off the research to focus on other important things in my life.

Finally, I would like to mention that I appreciate the chances given to me by the University of Twente to improve my skills in the discipline of engineering, which I enjoy to the fullest. I feel ready to start my next journey in life, in which I can only hope to receive the same support that was given to me during this journey.

Abstract

In the rapidly advancing field of aerospace, smallsats are becoming increasingly dominant in their presence in low earth orbit. Additionally, the ever-decreasing size of transistors and microchips in electronics causes the power density of the electronics in these relatively small satellites to increase. These two trends combined cause heat dissipation from satellite structures to become more difficult, making it progressively harder to cool such structures using passive cooling. Active cooling loops offer a solution by using a working fluid to transport heat from the heat-generating electronics to a radiator that dissipates the heat into space, making the cooling process more powerful. These loops require a pump to function, which is why NLR and Demcon Kryoz designed a micro-pump suited for smallsats that induces a flow of fluid using several vibrating piezo elements.

To test the ability of this micro-pump to function in space and to survive the launch loads, an in-orbit demonstration is required. In this report, the in-orbit demonstration experiment is designed in a step-by-step design process. Several components that make up this in-orbit demonstration to test the functionality of the micro-pump are fluidic components that are part of the cooling loop, as well as structural elements to create a rigid design and electrical components to control the pump and the heat inputs of the experiment. The report features the build-up of concepts, detailed design, and finally the system analysis.

This system analysis contains a budget reflection that shows that the design complies with the weight-, volume- and power budget set by the system integrator. Additionally, it features multiple calculations and simulations to mechanically, fluidically, and thermally estimate the performance of the final design of the in-orbit demonstration. From the mechanical analysis, the design is shown to be able to cope with the sine- and random vibrations that the satellite will experience during the launch process with a positive margin on yield strength and relatively small deformations. Moreover, the fluidic components are proven to be able to handle the pressure build-up that might occur due to rising system temperatures. The fluidic analysis shows that the entire cooling loop has a pressure drop of 3.4 mbar in the worst-case scenario, which is a pressure drop that the pump can overcome as shown in several performance tests. The thermal analysis shows that the temperature of the system will not exceed the set temperature range boundaries in both operational mode and idle mode. The percentage of the input heat that is dissipated into space through the radiator is between 50% and 85% depending on the satellite frame temperature and the power rating of the heat source.

The design is shown to conform to almost all requirements set in cooperation with NLR and the system integrator. Improvements that can be made to support the concept design are more thorough vibration analyses, bolt calculations, fatigue calculations and thermal expansion calculations.

Table of Contents

Acknowledgements	i
Abstract	ii
1 Problem Analysis	1
2 Design Assignment	3
3 Design Requirements	5
4 Concept Analysis	8
4.1 Micro-Pump Concept	8
4.1.1 Micro-Pump Design Specifications	9
4.1.2 Micro-Pump Working Fluid	10
4.1.3 Micro-Pump Performance Tests	11
4.2 Drive Electronics Concept	13
4.2.1 Drive Electronics Design Specifications	14
4.2.2 Drive Electronics Performance Tests	14
4.3 Accumulator Concept	15
4.4 Radiator Plate Concept	18
4.5 Heat Exchanger Concepts	20
4.6 Tubing Concepts	22
4.6.1 Tubing Type / Material Selection	22
4.6.2 Fluidic Filling Interface Concept	23
4.6.3 Tube Routing Concept	26
4.6.4 Tubing Connection Method Concept	26
4.7 Housing Concept	28
5 Detailed Design	29
5.1 Radiator Design	29
5.1.1 Energy Balance of the Radiator Plate	29
5.1.2 Radiator Coating Selection	35
5.1.3 Initial Equilibrium Temperature Calculations	35
5.1.4 Mechanical Connection of the Radiator Plate	37
5.2 Heat Exchangers Design	38
5.2.1 Resizing of the Heat Exchangers	38
5.2.2 Thermal Analysis of the Offset-Strip Fin Heat Exchangers	39
5.2.3 Fluidic Analysis of the Offset-Strip Fin Heat Exchangers	41
5.2.4 Performance optimisation of the Heat Exchangers	41
5.2.5 Mechanical Connection of the Heat Exchangers	44
5.3 Tubing Design	45
5.3.1 Fluidic Analysis of the Tubing	45
5.3.2 Mechanical Connection of the Tubing	48
5.4 Accumulator Design	50
5.4.1 Resizing the Accumulator	50
5.4.2 Resizing and Selecting the Accumulator Wick	53
5.4.3 Selecting the Accumulator Heater	55
5.4.4 System Filling Method	60
5.5 Heat Source Selection	60
5.5.1 Heat Source Pre-Selection	60

5.5.2	Heat Source Final Selection	61
5.5.3	Mechanical Connection of the Heat Source	63
5.6	Housing Design	63
5.6.1	Mechanical Connections of the Housing	64
5.6.2	Multi-layer Insulation	67
5.7	Sensor Locations	68
5.8	Final Design Overview	68
6	System Analysis	70
6.1	Budget Reflection	70
6.1.1	Weight Budget Reflection	70
6.1.2	Volume Budget Reflection	71
6.1.3	Power Budget Reflection	72
6.2	Mechanical Analysis	72
6.2.1	Strength Analysis	72
6.2.2	Vibrational Analysis	74
6.3	Fluidic Analysis	79
6.4	Thermal Analysis	81
6.4.1	Theoretical Approach on the System Thermal Analysis	82
6.4.2	FEM Simulations on the System Thermal Analysis	87
7	Conclusion	91
8	Discussion	92
9	References	94
A	Material and Component Properties	98
B	Fluid Properties	99
C	Accumulator Heater Specifications	100
D	3-K Method Loss Coefficients	101

Nomenclature

Symbol	Description	Units
A	Area	[m ²]
D	Diameter	[m]
E	Voltage	[V]
F	View Factor	[-]
G	Intensity	[W m ⁻²]
H	Height	[m]
K	Fluidic Loss Factor	[-]
L	Length	[m]
M	Molecular Mass	[g mol ⁻¹]
P	Power	[W]
Q	Heat Transfer Rate	[W]
R	Thermal- or Electrical Resistance	[K W ⁻¹] or [Ω]
R _g	Universal Gas Constant: 8.314	[J mol ⁻¹ K ⁻¹]
T	Temperature	[K]
V	Volume	[m ³]
a	Albedo Factor	[-]
c _p	Specific Heat Capacity	[J kg ⁻¹ K ⁻¹]
g	Gravitational Constant: 9.81	[m s ⁻²]
h	Heat Transfer Coefficient	[W m ⁻² K ⁻¹]
k	Coefficient of Thermal Conductivity	[W m ⁻¹ K ⁻¹]
m	Mass	[kg]
p	Pressure	[Pa]
v	Velocity	[m s ⁻¹]
α	Angle or Coefficient of Absorptivity	[°] or [-]
β	Angle or Coefficient of Thermal Expansion	[°] or [m ³ m ⁻³ K ⁻¹]
ϵ	Coefficient of Emmissivity	[-]
η	Dynamic Viscosity	[Pa s]
θ	Angle	[°]
ν	Kinematic Viscosity	[m ² s ⁻¹]
ρ	Density	[kg m ⁻³]
σ	Stress or Surface Tension	[Pa] or [N m ⁻¹]
σ_b	Boltzmann Constant: 1.3806e-23	[kg m ² s ⁻² K ⁻¹]
ΔH	Pressure Head	[Pa]
ΔH_{vap}	Heat of Evaporation	[J kg ⁻¹]
ΔT	Temperature Difference	[K]
ΔV	Volume Difference	[m ³]
Δh	Height Difference	[m]
Δm	Mass Difference	[kg]
Δp	Pressure Difference	[Pa]
Δt	Time Difference	[s]
Subscript		
acc	Accumulator	
alb	Albedo	

amb	Ambient
cap	Capillary
con	Contraction
cond	Conduction
del	Drive Electronics
D_h	Hydraulic Diameter
ear	Earth
el	Electrical
exp	Expansion
f	Fluid (Liquid Phase)
frm	Frame
g	Gas
h	Hydraulic
hpt	Housing Plate
ht	Heating
in	Incoming
int	Internal
l	Loss
max	Maximum
min	Minimum
out	Outgoing
phc	Phase Change
pmp	Pump
pr	Pore
rad	Radiator
red	Reduction
res	Resistance
slp	Solar Panel
spc	Space
src	Heat Source
st	Start
stp	Stop
sup	Support
sun	Sun
sys	System
tb	Tube
th	Thermal
tot	Total
vap	Vaporization
vs	Volume to Surface
w	Wick

Dimensionless Numbers

Nu	Nusselt Number	[-]
Pr	Prantl Number	[-]
Re	Reynolds Number	[-]
f	Friction Factor	[-]
j	Colburn Factor	[-]

1 Problem Analysis

In the last several years, the population of satellites in LEO (Low Earth Orbit) has seen exponential growth, which is a trend that is expected to continue during the following decade [1–3]. Low earth orbit is defined as the orbit closest to Earth with an altitude between 500 and 1000 km. On the 4th of May 2023, this orbit contained around 6500 satellites of which most were so-called 'smallsats' [4]. These smallsats are defined as satellites that weigh below 180 kilograms and are used for many different purposes like communication, Earth observation, technology development, navigation, and space science [5].

A branch of smallsats that has gained more popularity in the last few years are CubeSats. These satellites fall within the category of nanosatellites, which is one of five subdivisions of smallsats. CubeSats, as its name suggests, consist of one or multiple cubes of 10 by 10 by 10 cm stacked on top of each other. Every cube is labelled as 1U, which stands for one unit and weighs up to 2.0 kg [6]. Originally developed in 1999 by the California Polytechnic State University in San Luis Obispo and Stanford University, these satellites were used for education and space exploration. However, in more recent years, the CubeSats have gained more capabilities and now provide governments, companies, and academics with an affordable option for space exploration and new technology testing.



Figure 1.1: Example of multiple 1U CubeSats in low Earth Orbit. [7]

Over the years, CubeSats have become more advanced and sophisticated, which has caused them to house increasingly more electronics in a small volume. Although this is advantageous to technological advancement, it also causes the units to generate more heat than in the past due to an increase in their power density. To prevent the electronics from overheating, this energy has to be transferred away from the heat-generating components and sent into space. For some satellites, it might be enough to simply use conduction to directly transfer the generated heat to a radiator attached to the electronics. This radiator heats up and radiates the energy away from the satellite using a surface with high emissivity. However, this method of heat dissipation is not enough for some applications that produce significantly more heat. In these cases, the

electronics have to be actively cooled using a flow of fluid that transfers heat from the electronics to a radiator.

To actively cool electronics within smallsats by inducing a flow of fluid, a pump is required. This pump has to be both relatively small and light to fit within the volume- and weight budget of these specific satellites. Additionally, it has to be robust enough to survive the harsh launch and space conditions that it is exposed to during its lifetime. To overcome these challenges, Demcon and NLR have worked together on a micro-pump that produces a pressure difference using multiple vibrating piezo elements. The main advantage of this pump over more conventional types like a centrifugal- or peristaltic pump is the robust design that features very few moving elements and is still able to function when one of the moving components fails.

Currently, a long-term test is being performed by NLR to check the performance of this pump over a long period. This test is useful to indicate the pump performance over time, but it is limited to the ambient conditions in the test lab of NLR, which are drastically different compared to the actual operating conditions experienced during the satellite launch and in low earth orbit. To prove that the micro-pump is able to operate in a real space environment, which would make the design more attractive to certain customers, an in-orbit demonstration has to be designed. The mechanical design of the in-orbit demonstration is performed by Demcon and is therefore within the scope of this master thesis, while the electric- and software development is performed by NLR and the system integrator. The report is built up in the order of a design process, starting with the requirements, followed by a concept analysis, a detailed design, and finally a system analysis. More information about the in-orbit demonstration can be found in Chapter 2 which dives deeper into the design assignment.

Demcon is a company that works on solutions to social challenges in the areas of aerospace, agriculture & food, defence & security, energy, high-tech systems & materials, life sciences & health, smart industry, and water & maritime. They aim to do so by developing, manufacturing, and supplying high-quality technology and innovative products. The company was founded in 1993 in a small room at the University of Twente and currently employs around 1000 people [8]. Demcon Kryoz, which is a sub-company within the overarching organization of Demcon, is mainly focused on designing thermal systems ranging from sub-ambient temperatures down to -273°C (0 Kelvin). Next to this, Demcon Kryoz also focuses on creating efficient flow control systems and cooling systems within different sectors like semi-con or defense.

**UNIVERSITY
OF TWENTE.**



DEMCON

KRYOZ



2 Design Assignment

The purpose of the in-orbit demonstration, which is introduced in Chapter 1, is to test the performance of the micro-pump developed by Demcon and NLR. In this case, the performance of the pump is defined as its ability to withstand the loads that it is subjected to during all tests and the launch while maintaining its function to transport heat. To realize this test, the in-orbit demonstration should house a mechanically pumped loop, which is schematically visualized in Figure 2.1.

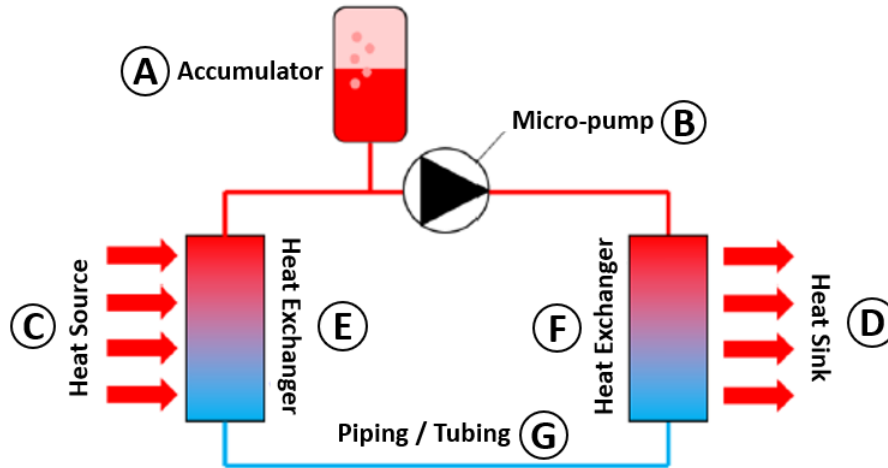


Figure 2.1: Schematic Representation of the mini-MPL that has been created by Demcon and NLR in a previous Project. [9]

At the heart of the mechanically pumped loop stands the micro-pump, depicted by 'B' in Figure 2.1. The accumulator is depicted by 'A' and serves the function of regulating and dampening the pressure in the system whenever the temperature of the fluid fluctuates. Two heat exchangers, depicted in the figure by 'E' and 'F' serve as the interface between the fluid, the heat source, and the heat sink. The heat source itself, depicted by the letter 'C', represents the heat-generating electronics that would be present during a real space mission. The heat sink, depicted by 'D', is a radiator plate with a surface coated in a high emissivity coating to more efficiently radiate heat into space. To fluidically connect all these components, tubing or piping depicted in the figure by 'G' is utilized.

Next to the components that are part of the mini-MPL, the final design has to consist of several structural and electrical components. The structural components should ensure a stiff connection of all components to the satellite frame to make sure that the design can withstand the loads it is subjected to. The electrical components consist of drive electronics, connectors, cables, and temperature sensors. These components are out of the scope of this design assignment but should be taken care of within the weight-, volume-, and power budget of the final design.

All components of the in-orbit demonstration should fit within 1U, which refers to a volume of 10 by 10 by 10 cm. Figure 2.2 shows the 6U frame in which the in-orbit demonstration will be launched. The 6U frame houses six different experiments of which the micro-pump experiment will be placed in the the top row of the frame and the column next to the solar panels as shown in the figure.

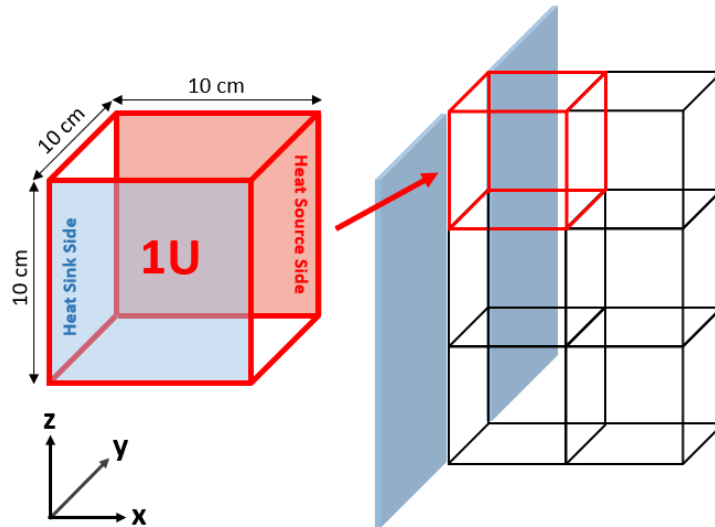


Figure 2.2: Schematic Representation of the 6U Frame that will be used to launch the In-orbit Demonstration.

Something that is also depicted in this figure is the orientation of the coordinate system that is used throughout the entirety of the report. It shows that the heat sink side is located on the opposite side of the heat source side, which indicates that the radiator plate points in the negative y-direction.

Alongside the volume budget of 1U is the weight budget of a maximum of 1.0 kg and a power budget of a maximum of 7.5 Wh per orbit. More detailed requirements are listed in Chapter 3.

3 Design Requirements

The following chapter entails the requirements that are set for the in-orbit demonstration, which can be found in Table 3.1. The requirements have been split into the following four sections: General System Requirements, Accommodation & Structural Requirements & Constraints, Experiment Functional Requirements, and Additional DEIMOS Specifications. Each of these sections has been further split into the actual requirements. Requirements that require further explanation or visualisation have been linked to a figure or table that helps to concretise the requirement.

Table 3.1: Overview of the System Requirements.

Requirement Section	Req. Nr.	Description
1. General System Requirements	1.1	The experiment shall be a mechanically pumped loop according to the scheme in Figure 2.1. It should consist of the following components: <ul style="list-style-type: none"> - Payload (electric heater) - Piping (flexible) with cooling medium (single phase / liquid) - Pump assembly with drive electronics - Accumulator - Temperature sensors - Heat Exchanger (heat source side) - Heat Exchanger (heat sink side) - Radiator
	1.2	The following hardware is third party delivered and shall be integrated into the experiment: <ul style="list-style-type: none"> - Radiator - Heat Exchangers - Drive Electronics
2. Accommodation & Structural Requirements / Constraints	2.1	The experiment shall fit inside a 1U volume compatible with the GOMSpace PC104 form factor.
	2.2	The maximum mass of the payload shall be <1kg.
	2.3	The mounting interfaces of the experiment shall be compatible with the GOMSpace PC104 form factor and/or the GOMSpace 6U Structure Assembly hole patterns.
	2.4	The experiment is currently being accommodated in the first U near the solar panels, which is visualised in Figure 2.2.
	2.5	The hot part of the experiment shall be at the side of the designated U opposite to the radiator.
	2.6	The integration of the radiator should take into account the reduced radiation space due to the hinges of the solar panels.
	2.7	Interfaces to the experiment shall be fail-safe and shall be expected to function with any single bolt missing.

Table 3.1: Overview of the System Requirements.

Requirement Section	Req. Nr.	Description
	2.8	A FEM analysis shall be done to the final design, including interface brackets / frames. The outcome of this analysis shall be provided to DEIMOS.
	2.9	<p>Elements sensitive to fatigue shall be designed to withstand a complete load history including:</p> <ul style="list-style-type: none"> - On-ground Tests (mechanical and thermal tests, at unit level) - Launch Phase - Thermos-elastic Loads in-orbit <p>A positive margin of safety shall be demonstrated with a scatter factor of 4 on the number of cycles.</p>
3. Experiment Functional Requirements	3.1	In stowed (installed in the spacecraft, mounted inside the rocket fairing, awaiting launch and during launch) conditions and under launch environmental factors, the pressure of the experiment shall not exceed 4 bars.
	3.2	<p>The experiment shall be sufficiently strong to survive the following pressures:</p> <ul style="list-style-type: none"> - Pressure build-up caused by direct sunlight on the radiator surface while the pump is offline. (or at least 65 °C) - Pressure build-up caused by heating the accumulator to 95 °C. (Investigate whether pump activity is of any importance in this regard) (Investigate if 95 °C is a correct upper limit)
	3.3	The experiment shall survive and be able to function nominally after being subject to launch load as described in Table 6.4.
	3.4	The experiment shall demonstrate compliance with the launch environment prior to FM experiment delivery.
	3.5	The experiment shall include means for filling and pressurizing the experiment before shipping to spacecraft integrator.
	3.6	The fill / pressurize interface closing shall be reversible during the flight qualification campaign, but have means to be securely fixed to ensure leak tightness during launch preparations and in space operations.
	3.7	The experiment may use an average of 5W continuous power along the whole orbit, which means it may discharge the spacecraft battery for 7.5 Wh during one orbit. (assuming one orbit takes approximately 90 minutes)
	3.8	The allowed peak power is 4 Amps at 12 Volts.

Table 3.1: Overview of the System Requirements.

Requirement Section	Req. Nr.	Description
	3.9	Input for the sizing of the dummy payload heater: <ul style="list-style-type: none"> - The experiment should demonstrate heat transfer to the maximum radiative power of the radiator. - Continuous transfer of this heat should be as long as possible, given the battery constraints in requirement 3.7. - Demonstration of continuous heat transfer for several consecutive orbits is desired.
	3.10	The experiment shall incorporate (at least) three temperature sensors, monitoring: <ul style="list-style-type: none"> - Heat Source Temperature - Heat Sink Temperature - Pump Housing Temperature
4. Additional Deimos Specifications	4.1	The outside surface of the experiment shall be electrically non-conductive, with the exception of the experiment housing mounting holes and bonding stud interfacing with the platform.
	4.2	Experiments shall not need physical adjustments after flight preparation, since it will not be directly accessible after integration in the carrier.
	4.3	The position tolerance of the payloads interface holes to the GOMSpace structure shall be +/- 0.1mm.
	4.4	Stainless steel helicoils shall be used in the case that the mounting holes of the experiment are not stainless steel.
	4.5	All coordinate frames shall be right-handed orthogonal systems to provide consistency across all providers.
	4.6	The payload shall demonstrate a positive margin of safety under yield for the qualification load cases.
	4.7	Any ferromagnetic material used in the payload shall be declared in a comprehensive list.

4 Concept Analysis

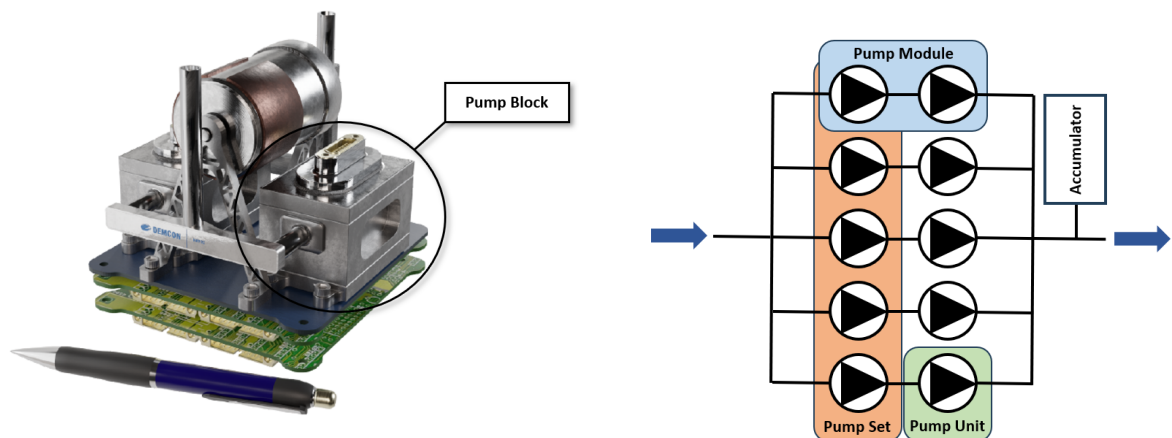
In this chapter, each of the main components in the in-orbit demonstration is conceptually analysed to find the most suitable design options. Some of these components have already been fully or partially designed. For example, the pump and the drive electronics do not require any redesigning, while the heat exchangers and the accumulator only need slight adjustments. These components do not need an entirely new concept analysis, since the concept is already defined. Therefore, these components are merely described in this chapter instead of conceptually analysed.

The components that are completely new to the design of the in-orbit demonstration like the radiator plate, tubing, heat source and housing are fully conceptually analysed to select their best possible concepts. Each of the best concepts will be further designed in the detailed design phase of Chapter 5.

4.1 Micro-Pump Concept

The micro-pump, designed in a previous project stands at the basis of the in-orbit demonstration. Information about the micro-pump that is relevant to this project and that is included in this section are the designed pump specifications, the chosen working fluid and the outcome of several performance tests that have been carried out on the pump.

The multi-parallel micro-pump designed by NLR and Demcon is a mechanical pump that uses multiple piezo elements to induce a flow of fluid. In the previous design, which can be seen in Figure 4.1a, two pump blocks are used that each house ten piezo elements as described in the diagram that is visualized in Figure 4.1b. In this diagram it can be seen that each piezo element represents a 'pump unit', each pair of piezo elements in series represents a 'pump module' and each row of parallel elements represents a 'pump set'. By arranging five pump modules in parallel, a full pump block is formed. In the design of the in-orbit demonstration, only one of these pump blocks is necessary, since one pump block is capable of delivering enough cooling power to the relatively low-power experiment. By placing piezo elements in series, the maximum head of the pump can be increased, while placing the elements in parallel causes the maximum flow rate of the pump to increase.



(a) Image of the Micro-pump in which a single Pump Block is highlighted. (b) Schematic Diagram of the arrangement of the piezo Elements within a single Pump Block.

Figure 4.1: Overview of the Previous Design of a Multi-parallel Micro-pump.

The piezo elements within the pump consist of a small membrane that deforms when the element is subjected to an electric field. The underlying phenomenon that causes this to happen is

the piezoelectric effect. By applying an alternating voltage with a certain frequency to a piezo element, the element will start to vibrate at this given frequency to induce a flow. Within each of the pump modules, the two piezo elements vibrate out of phase. To make sure that the pump has no backflow, the inlet and outlet of each pump chamber are closed off in one direction using check valves. These check valves only allow the fluid to flow from the inlet to the outlet when enough pressure is created in the pump chamber by the movement of the piezo element. Figure 4.2 shows how this effect is utilized within the micro-pump using a frequency of 100 Hz. Based on the frequency at which the piezo elements vibrate, the pump performance will change, which is one of the experimental tests that has been performed in Section 4.1.3.



Figure 4.2: Utilization of the Piezoelectric Effect within Micro-Pump at a Frequency of 100 Hz.

4.1.1 Micro-Pump Design Specifications

In the most current version of the detailed design definition and justification document of the mini-MPL project, the specifications of the micro-pump design are stated [9]. This section will briefly describe the most relevant information in this document to gain an overview of the properties of the micro-pump.

General Dimensions Figure 4.3 shows the general dimensions of the design of the pump block. In this figure, the dimensions of the inlet and outlet pipe are not shown, since this can be changed according to volume needs. Additionally, the size of the holes in the four support feet of the pump are available for small modifications. The other dimensions are not to be changed, which is seen as one of the boundary conditions of the volume budgeting within the design. The reason that other parts of the pump cannot be changed is due to manufacturing implications, elevated costs, and since this might cause the simulations performed during its designing process to become irrelevant.

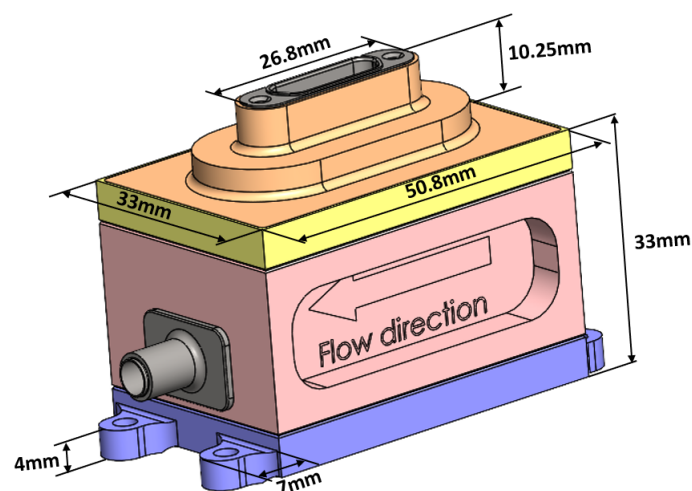


Figure 4.3: General Dimensions of the Pump Block Assembly.

Mechanical Performance The micro-pump has been designed to withstand the vibrational loads stated in Table 6.4. Additionally, it is designed to withstand internal pressures of 3.4 bar during operation and testing, 5.1 without any permanent deformation and 8.5 bar without rupture. It should be able to handle these pressures during operation for a lifetime of at least three years, while being subjected to temperature cycles between 25 °C and 85 °C. All of this is combined with the fact that the pump is designed to have very low outgassing to prevent any of the materials from degrading. During the design of the pump, several mechanical analyses have been performed on different sub-components. A few examples are a strength analysis, an o-ring compression analysis and a stress analysis, a check valve fatigue analysis and a gravity effect analysis.

Fluidic Performance The most important piece of information regarding the fluidic performance of a pump is its pump curve. The pump curve shows the available head that the pump can produce versus its flow rate. The characteristics of such a curve are that it shows its maximum pump head at a flow rate of zero and the maximum flow rate at a pressure head of zero. In the design phase, however, the pump curve is not yet known and can only be estimated based on calculations. The actual performance of the pump can be found in Chapter 4.1.3, in which the performance of the pump has been tested to gain a partial pumping curve.

In the design definition and justification document, it can be read that the dual micro-pump is designed to reach fluid flows of 2.0 - 3.0 $\frac{g}{s}$ and has a maximum pump head of 170 mbar. As has been stated before, the in-orbit demonstration only uses one pump block, which would result in a fluid flow of 1.0 - 1.5 $\frac{g}{s}$ with the same pressure head of 170 mbar. Using a model in Simscape, the internal pressure drop within the pump block has been estimated to be around 11.3 mbar when the fluid is at -40 °C, 7.3 mbar when the fluid is at room temperature and 6.0 mbar when the fluid is at 85 °C [9]. Something that does have to be taken into account is that this pressure drop is calculated using a mass flow rate of around 1.25 $\frac{g}{s}$ per pump block. For lower mass flow rates, these pressure drops will decrease significantly.

4.1.2 Micro-Pump Working Fluid

The working fluid that was selected during the previous project is Galden HT55. The properties of Galden at 25 °C and atmospheric pressure can be found in Appendix B. This appendix also features the viscosity of the Galden fluids as a function of temperature and the operating temperature of the Galden fluids at atmospheric pressure.

In reality, the fluid properties are both dependent on pressure and temperature. However, since the change in properties due to pressure differences is relatively small compared to the change in properties due to temperature differences, the properties are considered constant at varying pressures. Another reason for this is that the pressure differences that occur in the system are negligible compared to the larger temperature fluctuation. The properties that are used in the thermal- and fluidic analysis are specific heat, thermal conductivity, kinematic viscosity, dynamic viscosity, density and vapour pressure. The specific heat and thermal conductivity of the fluid are considered to be constant for varying temperatures since the engineers of the Galden fluids do not provide any information on the temperature dependence of these two properties and because these values do not vary much within the selected temperature range for other better examined and similar engineered fluids. The fluid density at different temperatures is calculate using the equation

$$\rho_{f1} = \rho_{f2}(1 + \beta_f(T_2 - T_1)) = \rho_{f2}(1 + \beta_f\Delta T) \quad (4.1)$$

To calculate the vapour pressure of the liquid at different temperatures equation

$$\ln\left(\frac{P_{vap,1}}{P_{vap,2}}\right) = \frac{\Delta H_{vap}}{R} \left(\frac{1}{T_2} - \frac{1}{T_1}\right) \quad (4.2)$$

is used. In both Equations (4.1) and (4.2), the subscript '1' refers to the known fluid properties at 25 °C, while the subscript '2' refers to the fluid properties at any other temperature. Since the kinematic viscosity of Galden HT55 is given in the technical data sheet and the density has been calculated, the dynamic viscosity can be calculated using the equation

$$\eta_f = \nu_f \rho_f. \quad (4.3)$$

Figure 4.4 shows the temperature dependence of the dynamic viscosity, kinematic viscosity, density and vapour pressure for Galden HT55. For all future calculations that involve fluid properties, these values are used.

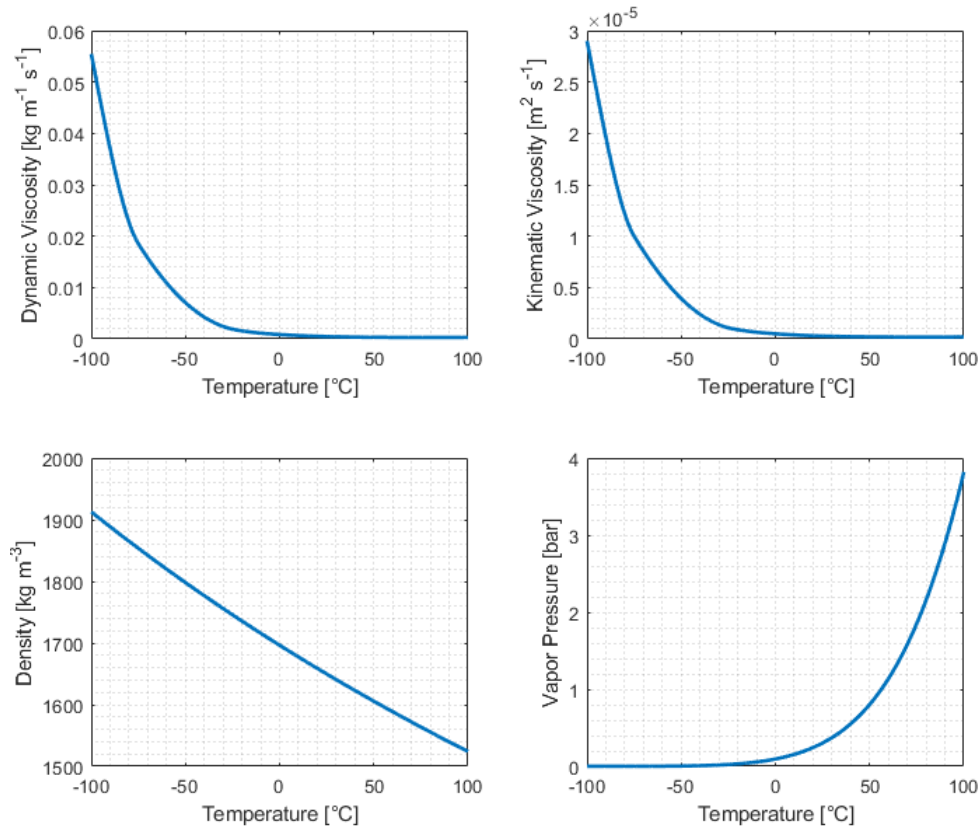


Figure 4.4: Temperature Dependence of several Fluidic Properties of Galden HT55.

4.1.3 Micro-Pump Performance Tests

To assess whether the micro-pump performs to the level it has been designed for, several performance tests are carried out at ambient conditions. These performance tests were carried out when the different components of the pump were not welded together yet, which required a special test setup to be built. The reason for testing the pump without welding is a choice made by Demcon to prevent the pump from being welded before it is proven to function correctly. In the test setup, the components of the pump are held together using a clamping method. This method assures that the o-rings within the pump chambers are correctly aligned and compressed. However, it does not create a fully leak-tight connection between the pump components like one that would be created using welds. To still be able to measure a flow with a certain pump head, the test setup in Figure 4.5 has been built.

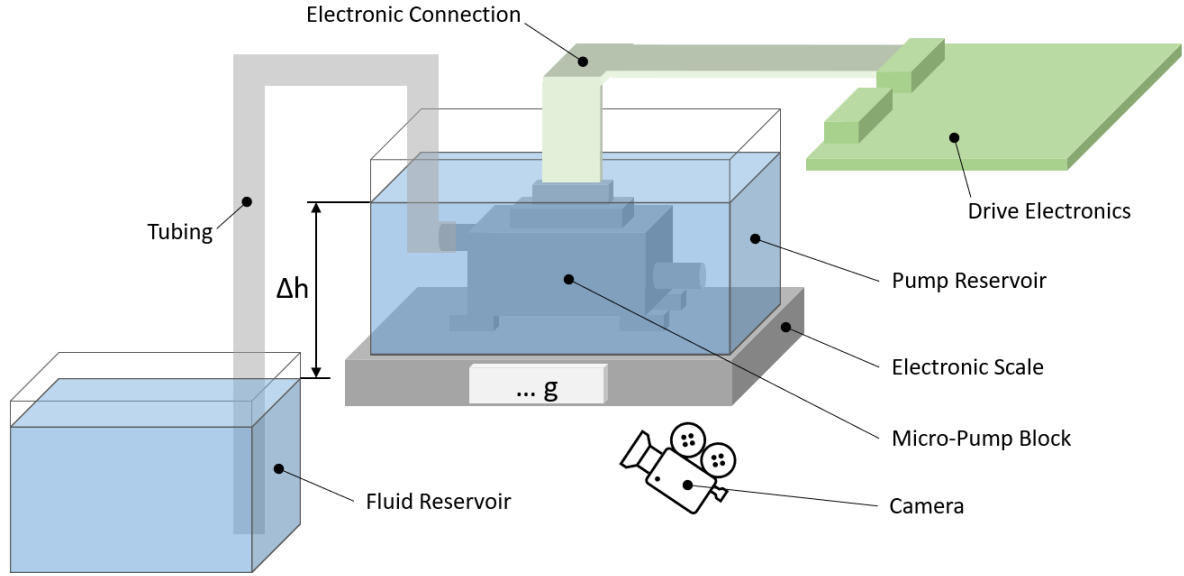


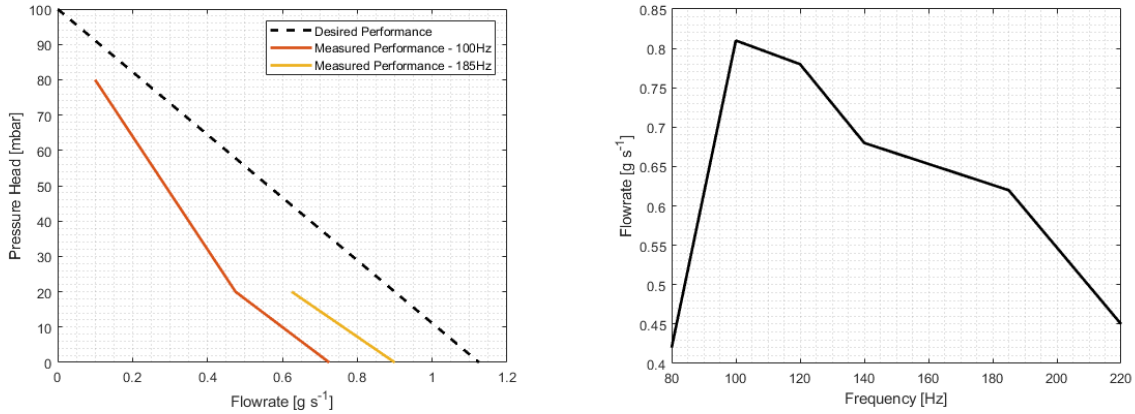
Figure 4.5: Schematic Representation of the Test Setup used to measure the Pump Performance.

In this test setup, the pump is submerged in the working fluid and fluidically connected to another fluid reservoir at its inlet. The pump reservoir is placed on top of an electronic scale to measure the amount of incoming mass flow when the pump is powered on. To power the piezo elements, the pump is electrically connected to the drive electronics, which in itself is connected to a power supply. The exact function of the drive electronics is further explained in Section 4.2.

The goal of the experiment is to show the pump performance in a single graph using the pump curve. The pump curve shows the flow rate that the pump can produce at varying pump heads. At the maximum pump head, the flow rate is zero, while at a pump head of zero, the maximum flow rate is reached. To examine the flow of the pump at different pump heads, the difference in height between the two reservoirs, which is represented by Δh in the figure, is changed between tests. The relation of the pump head with the pump height is described using Equation (4.4).

$$\Delta H = \Delta h g \rho_f \quad (4.4)$$

From the moment that the pump is turned on, a camera tracks the increase in mass using the electronic scale to measure the mass flow that the pump can deliver at a certain pump head. However, the measured mass flow is lower than the actual flow that the pump can deliver, which is caused by the relatively fast evaporation of the working fluid. Therefore, a zero measurement is made where the pump is turned off, to track the rate of evaporation. By adding this evaporation rate to the measured flow of the pump, the effective mass flow is calculated. The results of the tests can be seen in Figures 4.6a and 4.6b.



(a) Partial Pump Curves at two different Operating Frequencies. (b) Flow rate vs. Operating Frequency with a Pump Head of 25 mbar.

Figure 4.6: Results of the Pump Performance Tests.

Something that immediately becomes clear is that the actual pump performance is lower than the designed pump performance. This could have many different reasons for instance the wrong alignment or compression of the o-rings, leakages through the connections between the pump components or wear of the piezo elements. The reasoning behind the difference in performance is out of the scope of this research and is not further looked into. However, the flow rate data gained from these tests is the data that will be used during the detailed design phase and system analysis in Chapters 5 and 6 respectively.

4.2 Drive Electronics Concept

The main function of the drive electronics designed by NLR is to facilitate the piezo elements within the micro-pump with the right voltage at the intended out-of-sync frequency. It does so by receiving a certain voltage from the satellite avionics and transforming this into the required voltage and frequency. Figure 4.7 shows the electrical function diagram of the mini-MPL for two pump blocks. In the in-orbit demonstration, only one pump block is used, which means that only one drive electronics board is used as well.

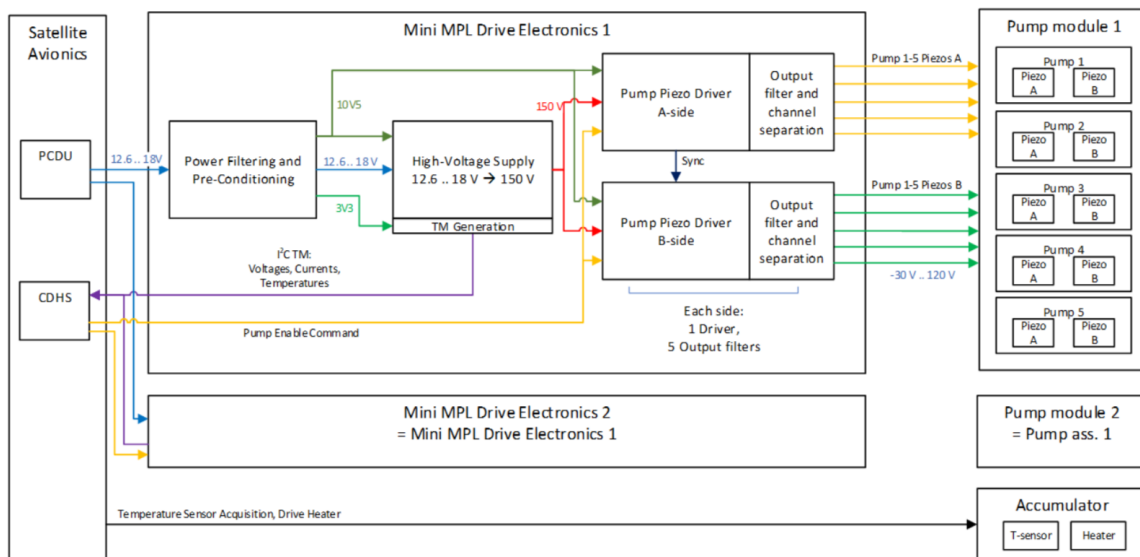


Figure 4.7: Electrical Function Block Diagram of the mini-MPL.

The figure shows in detail what voltage is present after each functional block within the drive electronics and how the connection between the drive electronics and the pump blocks is made. The main function of the first block of the drive electronics, which is the power filtering and pre-conditioning block, is to regulate and distribute different voltages to the subsequent function blocks. Next up is the high-voltage supply of which its main function is to convert the smaller unregulated bus voltage to a regulated 150 V required by the piezo drivers. The last step is the pump piezo drivers and the output filters that generate the intended frequency drive signal using a 50% DC square wave and that enable or disable the drive function based on the pump enable command line.

4.2.1 Drive Electronics Design Specifications

The specifications of the drive electronic design can be found in the most recent version of the design definition and justification document of the mini-MPL project [9]. This section briefly describes the most relevant information in this document to gain an overview of the properties of the drive electronics.

General Dimensions Figure 4.8 shows the general dimensions of the drive electronics board. These dimensions have been selected based on a previous design in which a satellite frame of ISIS space was utilized. During this project, these dimensions cannot be modified, which means that the drive electronics board with its current dimensions has to fit into the design as is.

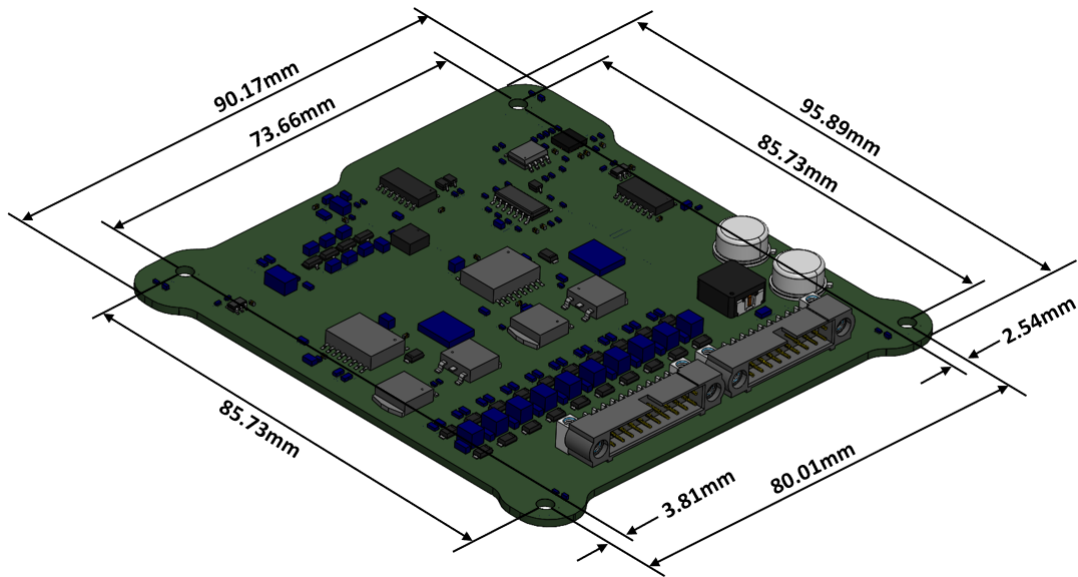


Figure 4.8: General Dimensions of the Drive Electronics Board.

Electrical Performance The drive electronics use a power source of between 12.6 and 18 V to function. In total, the pump and the drive electronics use 0.81 W of nominal power. From this total amount of power usage, the share of the piezo elements inside the pump is estimated to be 50%. The drive electronics board does not feature a current restriction to keep the design simple and compact. To check the performance of the output signal of the drive electronics, a test has been performed, which is documented in Section 4.2.2

4.2.2 Drive Electronics Performance Tests

To test whether the output signal of the drive electronics functions as expected, an oscilloscope is utilized. Oscilloscopes measure and display an incoming voltage signal in waveform, to visualize

the change in voltage over time. In this case, two piezo elements of the same pump module are tested at the same time at 100 Hz to see whether the voltage waves are out of sync as expected. Additionally, the peaks of the voltage waves, which are expected to be at 120 to -30 V, are measured. Figure 4.9 shows a picture that was taken of the oscilloscopes while measuring the output signal of the drive electronics.

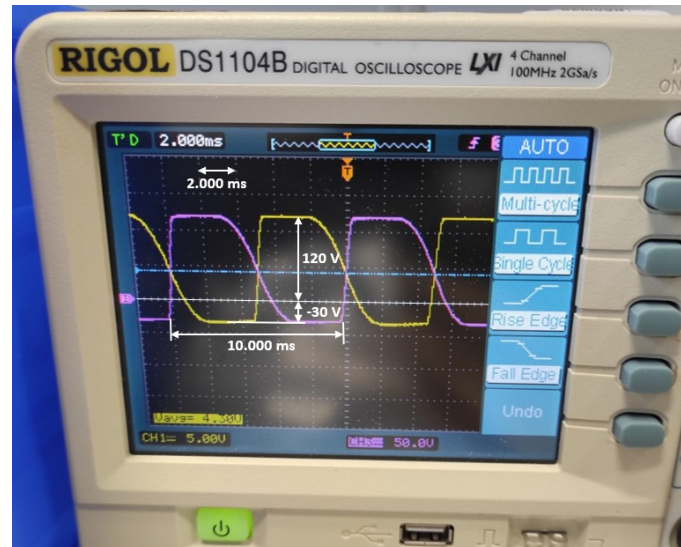


Figure 4.9: Picture taken of the Oscilloscope while measuring the Performance of the Drive Electronics.

The figure shows that the output signal of the drive electronics is measured to be a square wave with a period of 10 ms. This corresponds to the 100 Hz signal that the drive electronics are set to produce. Moreover, the two waves show up to be perfectly out of sync with a voltage peak at 120 and -30 V. Therefore, the drive electronics are shown to be functioning as expected.

4.3 Accumulator Concept

During the experiment of the in-orbit demonstration, the temperature of the fluid in the system fluctuates based on the incoming and outgoing sources of energy. Due to this fluctuation, the fluid in the system thermally expands and contracts. Considering the system has a constant volume, the pressure in the system would massively fluctuate during the thermal expansion or contraction of the fluid, which would most likely lead to damage of several fluidic components. To prevent this from happening, an accumulator is added to the system. In a previous design, which can be seen in Figure 4.10, the accumulator was sized to function with a certain fluid and fluid volume. Since a different fluid will be used in the new design and since the fluid volume in the system will be reduced, the accumulator will have to be resized, which is the main task when it comes to the detailed design phase of the accumulator in Section 5.4.

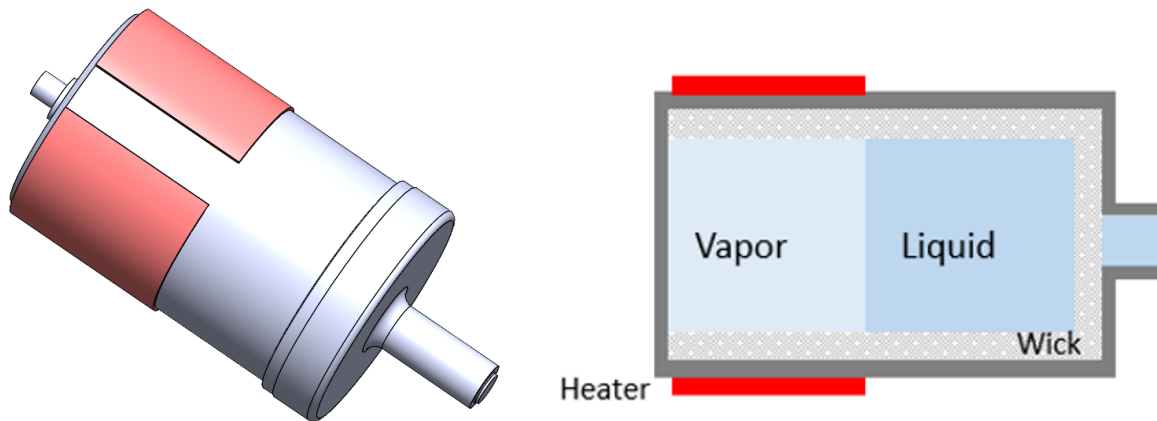


Figure 4.10: Detailed View (left) and Schematic Cross-sectional View (right) of the Previous Accumulator Design. [9]

The working principle of the accumulator is based on the evaporation and condensation of the fluid present in the body of the accumulator. If the fluid within the closed loop decreases in temperature, which causes the fluid to contract, a heater that is attached to the accumulator will heat the liquid within the accumulator to evaporate a certain fraction of the fluid. Since the created gas has a lower density compared to the fluid, the thermal contraction of the fluid will be counteracted by the increase in volume due to evaporation, to keep the pressure in the system constant. After the evaporation of fluid, the heater is supplied with new fluid by the wick. The wick is a thin hollow cylinder made of porous material that fits precisely within the accumulator housing and uses capillary forces to create a flow of fluid towards the accumulator heater. It also serves as a layer that prevents gasses from leaving the accumulator at its inlet. If the temperature in the system increases, the fluid will expand and the gas within the accumulator will increase in pressure. In this case, the heater of the accumulator will be turned off, which will cause heat to escape from the system and start a condensation reaction. This condensation process will balance out the expansion of the fluid within the system to maintain a constant pressure.

Temperature & Pressure Selection After the filling process of the system, the pressure of the fluid in the system is 1.0 atm. At this pressure, the Galden HT55 would evaporate at a temperature of 55 °C, which is expected to be too close to the equilibrium temperature during the operational mode. Therefore, it would be more convenient if the fluid would start to evaporate at higher temperatures. To increase the boiling temperature of a liquid, which is the point at which a liquid starts to evaporate, the pressure of the liquid has to be increased. To accomplish this task, the accumulator heater is powered on to start the evaporation process, which will increase the pressure within the system. This heating process continues until it reaches the selected temperature, which corresponds to a certain vapour pressure. The selected temperature should be higher than the maximum temperature that the system is expected to reach. In this way, the accumulator is able to dissipate heat to the system in case the condensation process has to be initiated. Additionally, in this way, the accumulator will never be able to be elevated in temperature by the system itself, which would increase the pressure in the system. An increase in pressure could result in stress concentrations that surpass the designed burst pressure of several components.

Since the pump is designed to work at a maximum temperature of 85 °C, the temperature in the accumulator should exceed this value. A margin of 5.0 °C has been chosen, which results in an accumulator temperature of 90 °C. In the bottom right graph of Figure 4.4, it can be seen that at this temperature, the vapour pressure of Galden HT55 is equal to 2.89 bar. This pressure is lower than the burst pressure of the pump, which means that no redesign of this component

is necessary. A strength analysis, that simulates whether the fluidic components can withstand the selected pressure, can be found in Chapter 6.

The density of the gas that is created inside the accumulator is based on the set pressure and temperature. By rewriting the ideal gas law to the equation

$$\rho_g = \frac{M p}{R_g T}, \quad (4.5)$$

the density of Galden HT55 gas at the operating temperature and pressure of the accumulator is calculated to be $32.97 \frac{\text{kg}}{\text{m}^3}$. The density of the fluid in the accumulator can be found in Figure 4.4 and is equal to $1539.7 \frac{\text{kg}}{\text{m}^3}$.

Housing Figure 4.11 shows a side view, isometric view and cross-sectional view of the accumulator housing design with the wick and the o-ring inside. The housing of the accumulator is designed to be leak-tight, feature an inlet, have a manner to connect the accumulator to the rest of the design and make sure that the wick is properly placed inside the housing. To fulfil these tasks, the accumulator is designed to consist of two housing bodies, specified as the cap and the cylinder, that can be welded together to become leak-tight. To create a low-weight component, the accumulator is made out of titanium. This also simplifies the process of connecting the accumulator to the pump, which is also made of titanium. Furthermore, an o-ring is placed in between the wick, which is placed inside the housing cylinder, and the housing cap. The purpose of this O-ring is to make sure that the wick is always tightly placed within the accumulator housing, without moving during expansion or contraction. At the rear side of the housing cylinder, a small solid cylinder is located that is used to connect a support structure to the accumulator housing. This support structure connects the accumulator to the rest of the design.

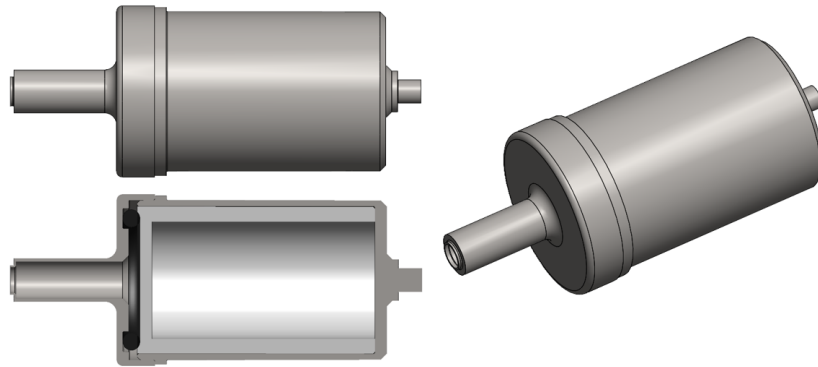


Figure 4.11: Side View, Isometric View and Cross-sectional View of the Accumulator Housing.

Support Structure To mechanically attach the accumulator to the other components in the system, a support structure is used. Figure 4.12 shows a representation of the support structure that can be connected to the solid cylinder on the rear side of the accumulator housing using a weld and a support ring. At the bottom of the support structure, it can be mechanically connected to another component using two bolted connections.

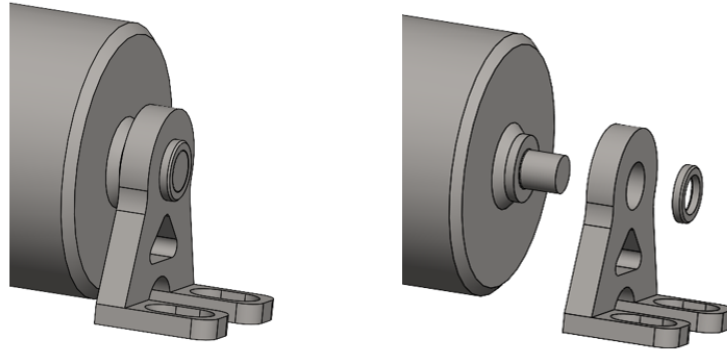


Figure 4.12: Isometric View and Exploded View of a Representation of the Accumulator Support Structure Connection.

Since the accumulator is the hottest component in the system and has to be kept at a constant temperature, it would be favourable to thermally isolate it from the rest of the system to reduce the amount of power that is necessary to keep it at this constant temperature. Therefore, the thermal resistance through the legs of the support structure should be increased by tuning the thickness of the trusses in the structure or by making the total structure longer. Therefore, the final design of the support structure is dependent on its thermal properties and is designed in Section 5.4.3 in the detailed design phase.

4.4 Radiator Plate Concept

In the ultra-high vacuum of low earth orbit, removing heat from a body through conduction or convection is not an option. Therefore, the only remaining method of transferring heat away from a certain structure is through radiation. To radiate energy away, satellites and other space structures use radiators, which are mostly flat structures coated with a layer of high emissivity and low absorbtivity coating. Since the radiator plate is the biggest heat sink of the in-orbit demonstration, it governs the amount of energy that can be dissipated into space. Therefore, the radiative power of the radiator determines the amount of heat that can be put into the system without causing the system to overheat.

The location of the radiator plate in the Cubesat frame can be seen in Figure 4.13. The figure shows that the radiating surface of the radiator is facing in the -y direction. Additionally, it shows that the radiator would have a maximum radiating area of 77 by 77 mm if it were to be placed on the inside of the satellite frame. Based on these observations a brief concept analysis has been made in Section 4.4

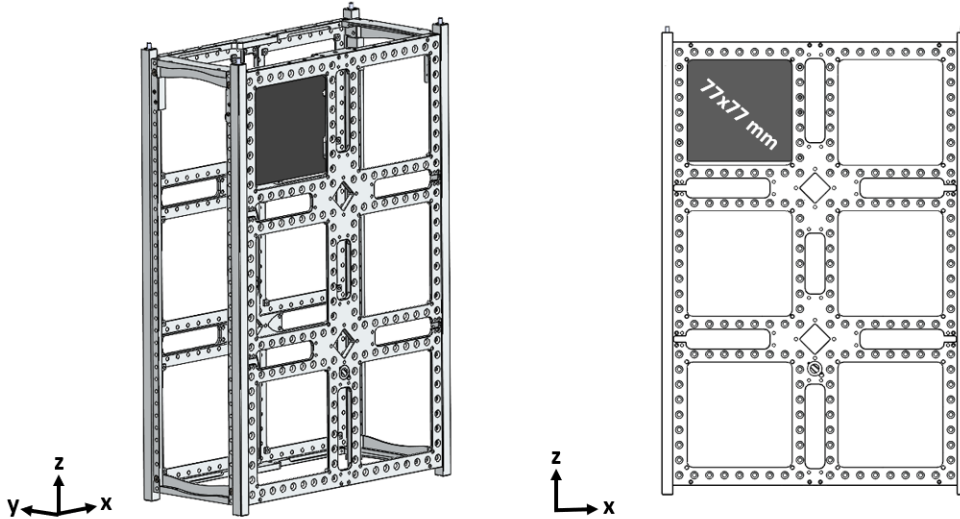


Figure 4.13: Location of the Radiator within the 6U Frame.

Although the radiator plate seems like a relatively simple component, it does require several design choices to be made. The three most important choices to be made are the shape of the radiator plate, the method of connecting the plate to the frame and the connection location of the radiator plate. Table 4.1 shows the different options that can be chosen for each of the design choices.

Table 4.1: Design Choice Options of the Radiator Plate.

Design Choice	Option 1	Option 2	Option 3
Radiator Shape	Simple Rectangle	Rectangle with leafsprings	-
Connection Method	Self locking nut	Internal nut & glue	Rivet nut & glue
Connection Location	Inside frame	Outside of frame	-

Connection Location To connect the radiator plate to the satellite frame, there are two possible options, which are on the inside or the outside of the frame. On the outside of the frame, the radiator would be able to have a higher radiating area than the 77 by 77 mm and could be connected to the four small holes in the corners of the square frame opening. However, by attaching the radiator plate on the outside of the frame while having the rest of the system on the inside of the frame, the design cannot be assembled within the satellite frame as one body. This insinuates that the system integrator, who is responsible for assembling the in-orbit demonstration along with other systems into the satellite frame, will have to walk through more complex steps of attaching the system to the frame. Together with the system integrator this is considered to be the less favourable option, since it could lead to wrong interpretations and mistakes. Therefore, attaching the radiator plate on the inside of the satellite frame is reasoned to be the better option.

Radiator Shape The shape of the radiator has two possible options that are functional. The reasoning behind this is that the volume of the in-orbit demonstration is a cube within a satellite frame that has square hole patterns. Therefore, other options like circular or triangular shapes are not taken into account.

The two remaining options are a simple rectangle or a rectangle with leaf spring connections. The main advantage that the leaf springs add to the design is that the connection of the entire experiment to the frame has more freedom to move in the normal direction of the plate, which

prevents the system from being overdetermined. If the system is overdetermined, it is hard to predict where the highest stresses in the system will occur, which could lead to unexpected failures during vibrational loads. Moreover, a simple rectangle would require more material to be added to the system, which increases the weight of the design. Taking both points into account, the best option is considered to be a radiator plate shaped like a rectangle with leaf springs.

Connection Method The connection of the radiator plate is made using a countersunk screw since the holes in the satellite frame are also countersunk. Because of the unknown contact area of a countersunk screw with the clamped part, it is near impossible to correlate the amount of torque that has to be applied to create the desired clamping force. Therefore, the only method to make sure that the connection will not get loosened during vibrations is by adding either a self-locking nut or glue.

The three available options that are defined are a bolted connection with a self-locking nut, an internal nut combined with glue or a rivet nut combined with glue. The first option is the only option of the three that cannot be used to attach the radiator plate to the satellite frame without having to access the inside of the frame. By discussing with the system integrator, it is considered more convenient to perform the assembly from the outside of the satellite frame, which is the reason for taking option one out of the equation. Out of the latter two options, the internal nut is found to be the most suitable option, since a rivet nut would create a new interface and take more space compared to the internal nut. Furthermore, an internal nut can be simply manufactured by tapping a thread in a through hole, while a rivet nut has to be pressed into the hole with a special tool.

Radiator Concept Figure 4.14 shows a schematic representation of the chosen radiator concept, which will be further worked out in Chapter 5.

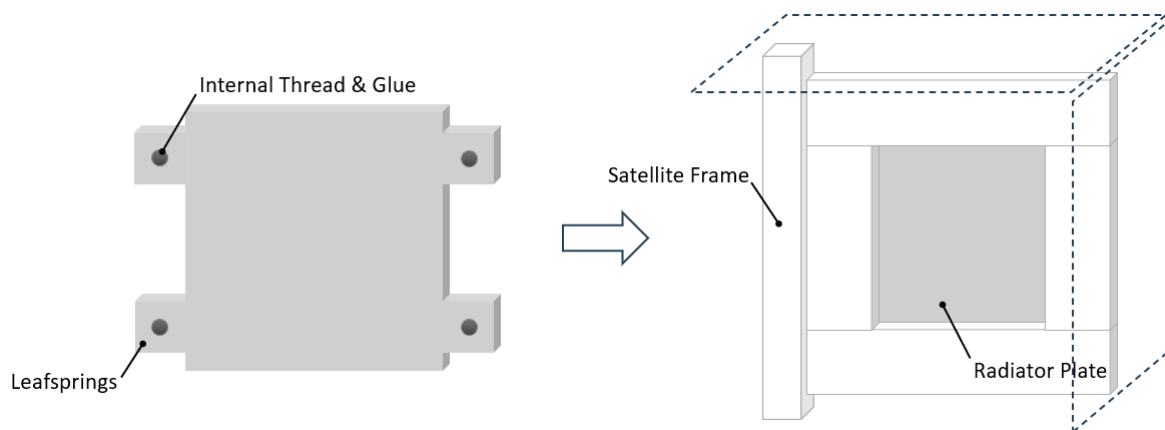


Figure 4.14: Schematic View of the Radiator Concept.

4.5 Heat Exchanger Concepts

The in-orbit demonstration features two fin-strip heat exchangers. One of these heat exchangers is attached at the heat source side to transport the heat produced by the heater into the working fluid, while the other heat exchanger is attached at the heat sink side to transport heat from the working fluid to the radiator plate. Figure 4.15 shows a previous design, that has already been manufactured by NLR. It was manufactured of AlSi10Mg using a 3D printing method. Since the heat transfer properties of this exchanger are already experimentally tested, the same type of heat exchanger will be used in the current design. The design choices that remain are the main body sizing, the fin geometry sizing, the mounting method of the heat exchangers to the housing or radiator plate and the layout of the inlet and outlet. However, the sizing of the heat

exchangers as well as the sizing of the fin geometries inside the heat exchanger can be seen as detailed design and will therefore be performed in the detailed design phase of Chapter 5.

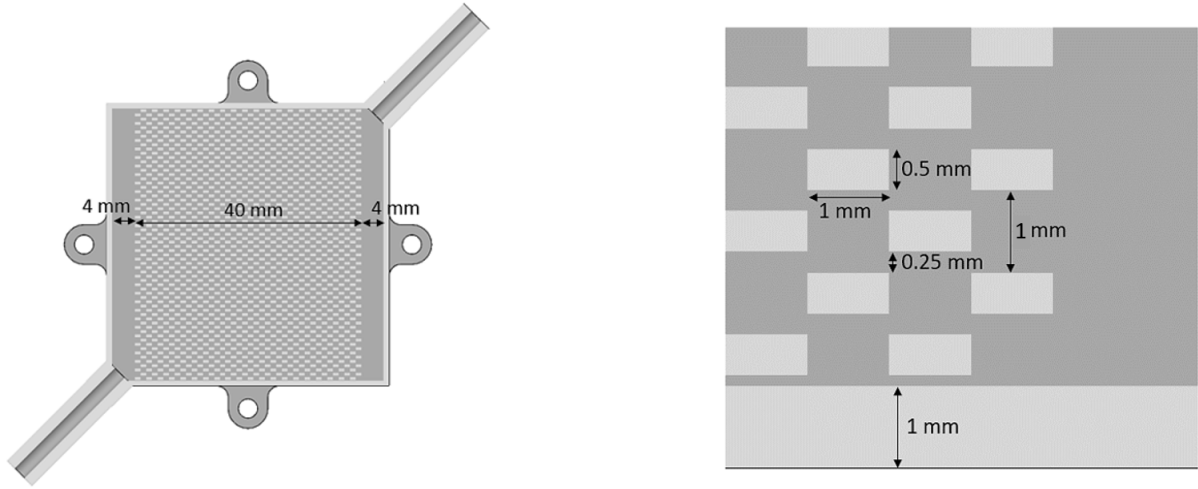


Figure 4.15: Cross-sectional View of the Heat Exchanger of NLR that visualizes the Fin Structure on the Inside.

The possible options for the remaining design choices can be found in Table 4.2. In this table, the connection method of the heat exchangers to the housing plate or the radiator plate are split, since these connections might be chosen differently.

Table 4.2: Concept Design Choice Options of the Heat Exchangers.

Design Choice	Option 1	Option 2	Option 3
Connection Method (Heat Sink)	Bolted connection	Welded connection	3D printed
Connection Method (Heat Source)	Bolted connection	Welded connection	-
Inlet / Outlet Layout	Parallel tubes	Perpendicular tubes	-

Connection Method - Heat Source On the heat source side of the in-orbit demonstration, the heat exchanger will be connected to a housing plate that is connected to the satellite frame. Since it is not favourable to lose too much heating power to conduction into the satellite frame, it would be best to thermally isolate this heat exchanger from the housing plate. A bolted connection is generally easier to isolate when compared to a welded connection. Therefore, this heat exchanger will be connected to the housing plate using a bolted connection.

Connection Method - Heat Sink On the heat sink side of the experiment design, the heat exchanger has to receive its power from the fluid in the loop and transport it into the radiator plate. On this occasion, the thermal resistance should be as low as possible to allow for efficient heat transfer between the components. The best possible option when it comes to heat transfer between two components is to maximize their thermal contact area. When using a bolted connection or a welded connection, the roughness of the materials will always cause an imperfect thermal connection. In this case, the radiator plate could be 3D printed together with the already 3D-printed heat exchanger. This option allows for perfect thermal contact, resulting in the most optimal heat transmission. Therefore, the heat exchanger on the heat sink side will be 3D printed as one piece together with the radiator plate.

Inlet / Outlet Layout To fluidically connect the heat exchangers to the rest of the fluidic system, the inlet and outlet have to be designed such that this connection can be effectively made. The biggest advantage of the inlet and outlet being parallel would be that the heat exchangers take up the least amount of space. However, a parallel connection would make it significantly more difficult to create an effective connection to the rest of the system, since it would require an extra bend to be made using another component. Therefore, the most suitable option seems to be to have the inlet and outlet perpendicular to the surface of the heat exchanger. Normally, this would be much more complex to produce, but since the chosen production method is 3D printing, this shape should not cause any manufacturing problems.

Heat Exchanger Concepts Figure 4.16 shows a schematic representation of the chosen heat exchanger concepts, which are further worked out in Chapter 5. On the left in the figure, the heat exchanger on the heat sink side can be seen attached to the radiator plate, while on the right it shows the heat exchanger on the heat source side, which will be connected using a bolted connection.

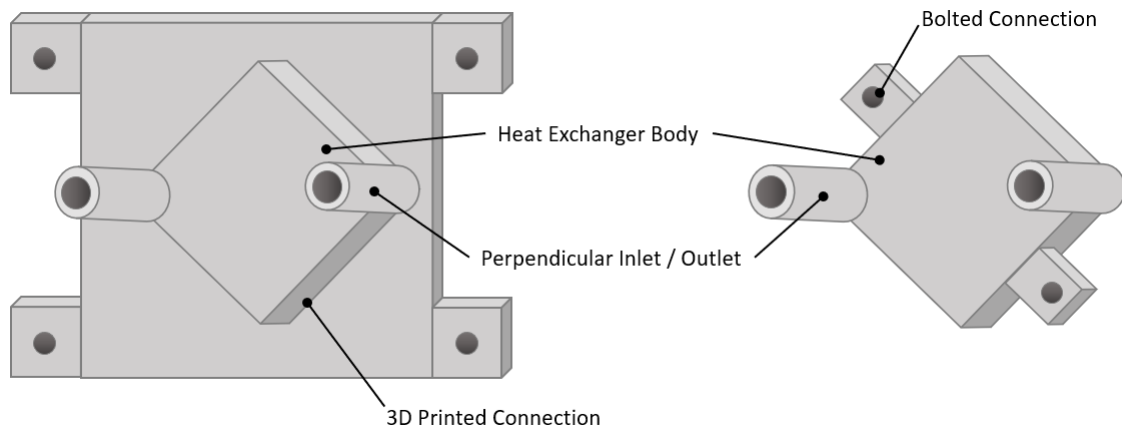


Figure 4.16: Schematic View of the Heat Exchanger Concepts.

4.6 Tubing Concepts

To create a closed fluidic loop, the heat exchangers, pump and accumulator have to be connected. This section analyses the different types of tubing that can be used, as well as the different routing possibilities and connection methods. In addition, a brief selection process is made for the filling process of the system for which a filling interface is designed.

4.6.1 Tubing Type / Material Selection

The two main types of tubing that can be used in this situation are flexible tubing and rigid tubing. Flexible tubing used in space applications is mostly made of Teflon, which is known for its low outgassing, high chemical resistance and broad operating temperature range. Rigid tubing is made of different types of metal like stainless steel, titanium or aluminium. To choose the best option in this case, the advantages and disadvantages of both options are taken into account.

The two main advantages of flexible tubing when compared to rigid tubing are that flexible tubing weighs less and is more flexible during assembly and thermal expansion. During assembly, this flexibility is advantageous, since it lowers the need for a tolerance analysis and reduces internal stresses during thermal expansion.

The main advantage of rigid tubing is that it adds extra stiffness to the system, which is advantageous to the rigidity of the system when subjected to vibrations. Since the rigid tubing is

made of metal, it does not show any significant amount of outgassing, is chemically inert and has a broad operating temperature range. Metal tubing also allows for connection methods to the other metal components in the system like welding and soldering that cannot be utilized with the flexible polymer tubing. These types of connections are strong and rigid options and offer great leak tightness.

By weighing the advantages and disadvantages of both options, rigid tubing has come out as the most useful option in this experiment. The main reasoning behind this is that a connection has to be made between the pump and the heat exchangers, which are made from titanium and an aluminium alloy respectively. By using flexible tubing, a third material would be introduced in this connection, which would introduce a relatively large challenge for creating a leak-tight connection within the given volume.

Moreover, the extra stiffness that the rigid tubing adds to the system is considered to be of importance when it comes to the survival of the structure during vibrational loads. Flexible tubing would add significantly less stiffness to the system and its dynamics are harder to predict.

Other reasons for selecting rigid tubing are that they are less permeable, the fittings used for metal tubing are more leak-tight and metal tubing is less vulnerable to UV light.

4.6.2 Fluidic Filling Interface Concept

Before the cooling system can operate, the entire system has to be filled with liquid. To make sure that the entire volume of the system is filled, a filling station will be used. This separate station can be connected to the in-orbit demonstration to first create a vacuum after which the system can be filled with fluid. This section discusses the concept of a filling station with its filling sequence. Additionally, it reviews the different possible options that can be used to interface the closed loop to the filling station.

Filling Station The filling station should be able to create a vacuum and fill the system with fluid while preventing air from flowing into the system and while preventing fluid from flowing into the vacuum pump. Additionally, the filling station should be able to measure and display the pressure in the system to firstly measure if the system is leaking and secondly show if the vacuum within the system is high enough to be filled with fluid. Figure 4.17 shows a schematic representation of the concept of the filling station.

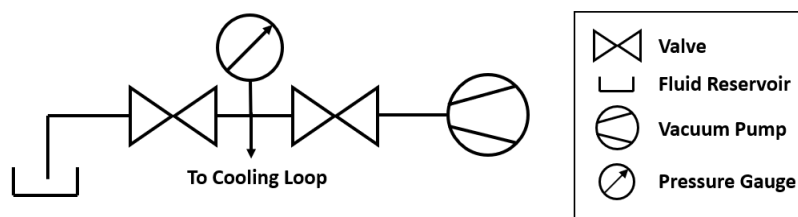


Figure 4.17: Schematic Representation of the Concept of the Filling Station.

The figure shows a fluid reservoir on the left, a vacuum pump on the right and two valves that serve as the interfaces between the reservoir, the pump and the cooling loop. Moreover, the pressure gauge is placed between the valve and is directly connected to the system using a connection method, which is selected in the 'Connection Method' paragraph of this section. By doing this, it is made sure that the pressure gauge always measures the pressure in the system during the filling process.

Filling Sequence Figure 4.18 shows the filling sequence that will be used to safely fill the system with fluid while preventing air from entering the cooling loop and while preventing fluid

from entering the vacuum pump.

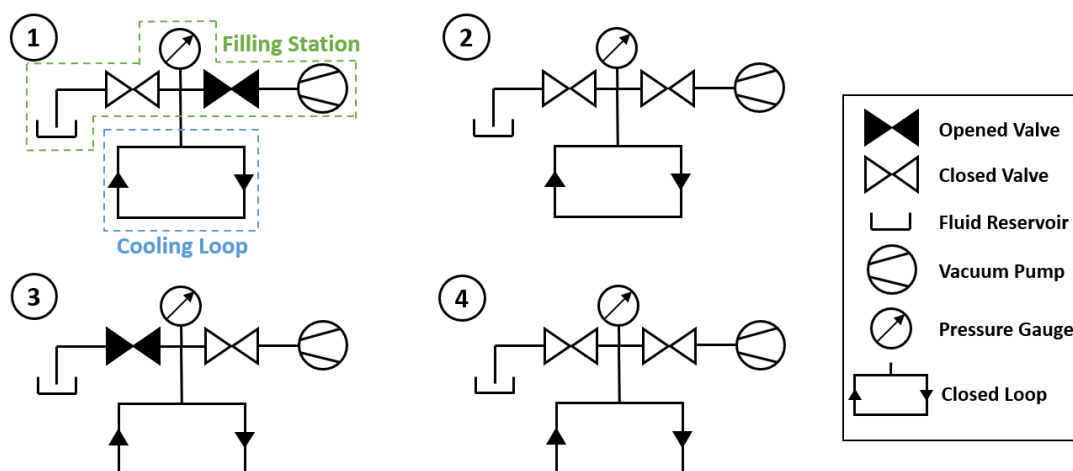


Figure 4.18: Schematic Representation of the System Filling Sequence.

In step one, only the valve to the vacuum pump is opened. The pump is powered on until a steady vacuum is reached in the closed loop. In step two, the valve to the vacuum pump is closed off to ensure no fluid will enter the pump when the valve to the fluid reservoir is opened. The pressure gauge makes it possible to determine whether there are big leaks in the system since the pressure should stay constant if the system is in a vacuum and closed off by both external valves. In step three, the valve to the fluid reservoir is opened. This will cause the atmospheric pressure at the fluid reservoir to push the fluid into the vacuum of the closed cooling loop. During this step, the operator has to make sure that the tube at the fluid reservoir stays under the fluid surface level to prevent any air from entering the system. Additionally, the valve to the cooling loop has to be opened gradually to prevent the fluid from rushing in too quickly, which could damage the piezo elements or electrical connections inside the pump. In the final step, all valves are closed and the in-orbit demonstration can be decoupled from the filling station. Additional information about the filling sequence after the process in Figure 4.18 has been completed can be found in Section 5.4.4. This additional information is important to make sure that vapour has formed in the accumulator before fully closing the system. If this step is not executed, temperature fluctuations might cause pressure build-up in the system which could lead to high internal stresses and eventually failure of certain components.

Connection Method To be able to connect the system to the filling station, a filling interface should be added to the in-orbit demonstration. The first step in doing so is by creating an outlet that is not part of the closed loop. The three selected methods to create a leak-tight connection are a valve, a quick disconnect pin or a threaded connection. A schematic representation of each connection method is shown in Figure 4.19.

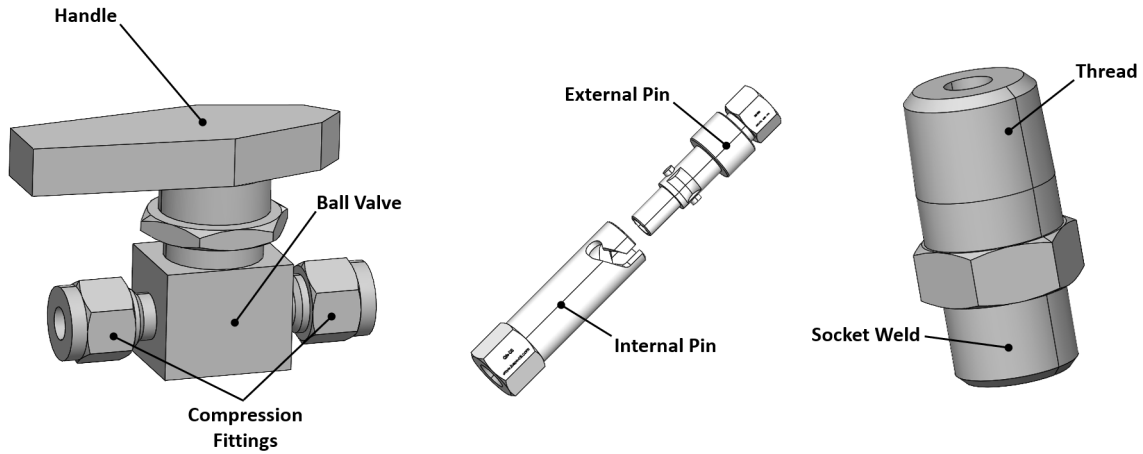


Figure 4.19: Schematic Representation of the Possible Connection Methods of the Filling Station to the mini-MPL. [10–12]

Table 4.3 shows a decision matrix that is used to select the most suitable option based on several relevant properties. These relevant properties are weight, size, leak tightness, practicality and outgassing. Each of the properties is assigned a weight factor based on relevancy to the performance of the component. Then, each of the three possibilities is given a score from one to five for each of the properties to finally find the best solution. The outgassing criterion is rated a one if the method is proven to show too much outgassing, a three if the method is known to be an outgassing risk and a five if the method is proven to have a CVCM lower than 0.1% and a TM lower than 1%.

Table 4.3: Decision Matrix for the Connection Method of the Cooling Loop to the Filling Station.

Criteria	Weight Factor	Ball Valve	Quick-Connect Pins	Threaded Connection
<i>Weight</i>	0.15	2	4	4
<i>Size</i>	0.25	1	2	4
<i>Leak Tightness</i>	0.25	4	4	3
<i>Practicality</i>	0.2	3	4	4
<i>Outgassing</i>	0.15	3	3	5
Total	100%	2.6	3.35	3.9

Using the decision matrix in Table 4.3, the choice for a threaded connection is made. The ball valve connection has been given the lowest score mainly because it is too heavy and too big to fit in the 1U volume next to all other components. The quick-disconnect pins came in second, mainly due to their low score on size. At first, the size of the quick-disconnect pins seems to be concise and slender, but after further investigation, this type of connection is relatively long and would require a long stretch of space to be reserved. Moreover, both the ball valve and the quick-disconnect pins are made from other materials than only metal, which might cause these components to be vulnerable to outgassing if for instance the wrong o-rings are used. The threaded connection does not have this problem, since it is fully made of metal. This connection type fits well into the rest of the system and can be welded to another part of the tubing to create a leak-tight and rigid connection to the rest of the system. The only downside to a threaded connection is the leak tightness, which could make it difficult to create a vacuum that is sufficient to fill the entire system. However, to fill the system, a vacuum of only 10^{-3} mbar is required, as has been found in previous filling sequences performed in the lab of Demcon Kryoz and NLR. This vacuum pressure can be reached using a threaded connection and Teflon tape.

4.6.3 Tube Routing Concept

Within the confined space that is available, the routing of the tubing has a large influence on the placement of the system components. Figure 4.20 shows three different routing concepts for the tubing. The location of the filling point is depicted by a small wave located at the connection of the heat source and heat sink. In all three concepts, the pump and the accumulator have been placed side by side to make sure that the connector of the pump is not blocked or hard to reach. This configuration also leaves enough space on top of the components to connect the heat source to the heat sink, which is the longest connection in the system. From these three options, the most suitable one is selected based on relevant factors like volume, alignment and ease of assembly.

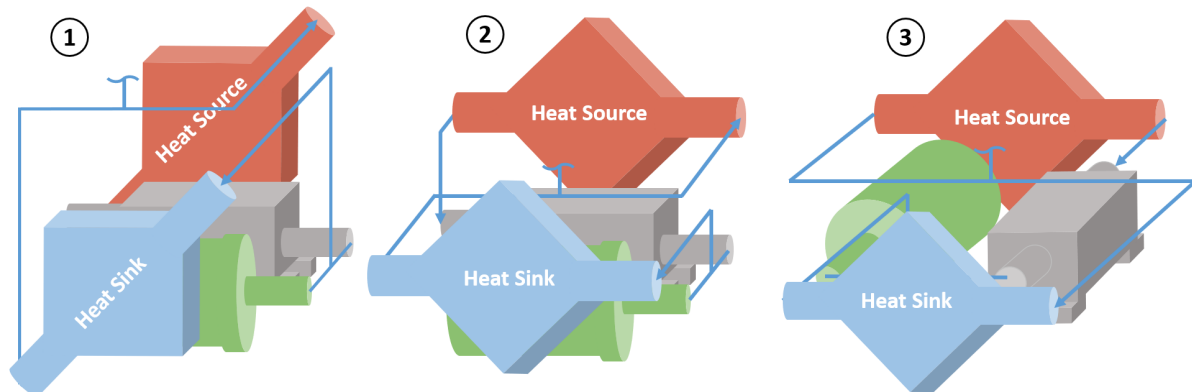


Figure 4.20: Schematic Representations of the three Routing Concepts.

The difference between concept one with concept two and three is that the heat exchangers in concept one are oriented diagonally, while in concept two and three they are oriented horizontally. The difference between concept three with concepts one and two is the orientation of the pump and accumulator with respect to the heat exchangers.

The concept that has the most potential based on volume, alignment and ease of assembly is selected to be concept two. Volume-wise, this concept offers the most efficient use of space, since it takes the shortest route to connect the components. It also leaves enough space for possible fittings or other connection methods on the sides perpendicular to the heat exchangers. Concepts one and three on the contrary both have at least one connection location that does not leave much space to create a connection, which might lead to volume issues later in the design phase. Additionally, the orientation of the pump and accumulator in concept three might not be optimal, since the length of these components is turned in the direction that also includes the thickness of the heat exchangers. When taking into account the ease of assembly, concept one might cause issues, since the connection points of the heat exchangers that are located at the bottom of the volume could be hard to reach during assembly. Taking all arguments into account, concept two is considered to be the most suitable routing option.

4.6.4 Tubing Connection Method Concept

The components that have to be connected to create a closed cooling loop are made of several different materials, which complicates the challenge of creating leak-tight connections. This section discusses the different connections that have to be made, as well as the possible options for solving them. Figure 4.21 shows the location of each of the connections that have to be made.

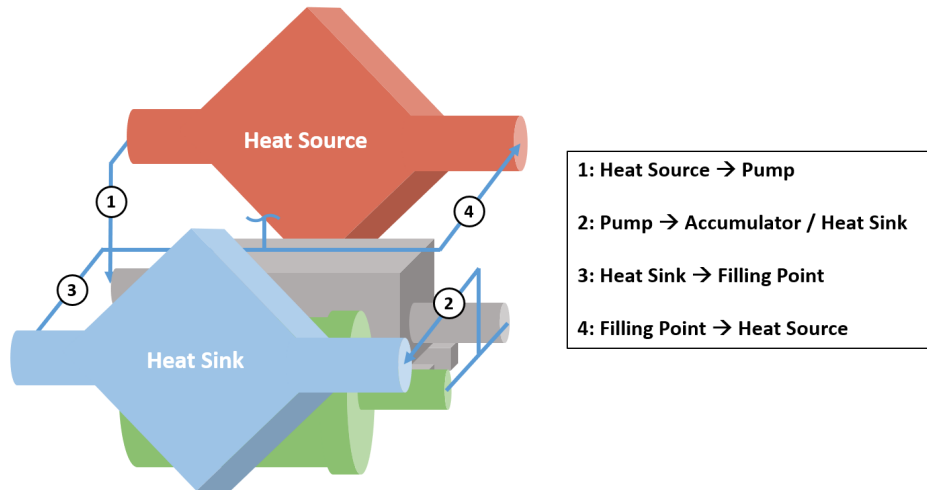


Figure 4.21: Schematic Representation of the different Connections of the Tubing in the System.

The most tight connections within the system are connections one and two. To facilitate these connections, two sharp turns have to be made in a confined space. Additionally, connection two is a three-way connection, since it needs to connect the pump to both the accumulator and the heat sink. The most logical option in this case would be to use a manifold, which is a custom-made fluid distribution body. Since the part is custom-made, the design is highly flexible in geometry and can be created such that the awkward and tight connections of the heat exchangers to both sides of the pump becomes more convenient. Because the pump and the accumulator are both made of titanium, it would be beneficial to manufacture the manifolds from the same material, to allow for a welding connection.

When the manifolds are in place, the challenge of connecting the heat exchangers, which are made of AlSi10Mg, to the titanium manifolds remains. To solve this problem, multiple options are considered. The option of welding the parts together is taken out of the equation considering the inconsistencies that occur when welding two parts of different metal types together. The four options that are taken into account are compression fittings, threaded fittings, metal glue and soldering. Table 4.4 shows the decision matrix that is used to select the best connection option. In this decision matrix, each connection method is rated from one to five based on the criteria of weight, size, leak tightness, practicality and outgassing. Each of these criteria is assigned a weight factor based on their importance to the design. The outgassing criterion is rated a one if the method is proven to show too much outgassing, a three if the method is known to be a risk and a five if the method is proven to have a CVCM lower than 0.1% and a TM lower than 1.0%.

Table 4.4: Decision Matrix for the Connection Method of the Heat Exchangers to the Pump Manifolds.

Criteria	Weight Factor	Compression Fitting	Threaded Fitting	Metal Glue	Soldering
<i>Weight</i>	0.15	2	2	5	4
<i>Size</i>	0.15	2	1	5	5
<i>Leak Tightness</i>	0.2	5	4	3	4
<i>Practicality</i>	0.1	4	4	3	2
<i>Outgassing</i>	0.2	5	5	3	5
Strength	0.2	5	5	2	3
Total	100%	4.0	3.65	3.4	3.95

From this decision matrix, the compression fitting and the soldering method have come out to be the best solutions. The compression fitting is seen as more robust, while the soldering method is seen as a more volume and weight-efficient option. Moreover, compression fittings are specifically designed to withstand dynamic loads. To make sure that the in-orbit demonstration can survive the vibrations during launch, the robust option is seen as the most valuable of the two, which is why this option is selected to be worked out in the detailed design phase of Chapter 5.

4.7 Housing Concept

To create a coherent design, that can be assembled into the satellite frame as a singular rigid body, a housing design is used. This housing is a simple piece of sheet metal to which the different components in the system like the heat exchangers, pump and accumulator are attached. Additionally, the housing itself is attached to the satellite frame. Figure 4.22 shows the three concepts of the housing frame that are considered. In these concepts, the housing plate can be seen as the bent sheet metal plate to which the heat source, which is shown as the red cuboid, is attached. Moreover, the radiator plate is shown as the opaque sheet metal plate to which the blue cuboid is attached.

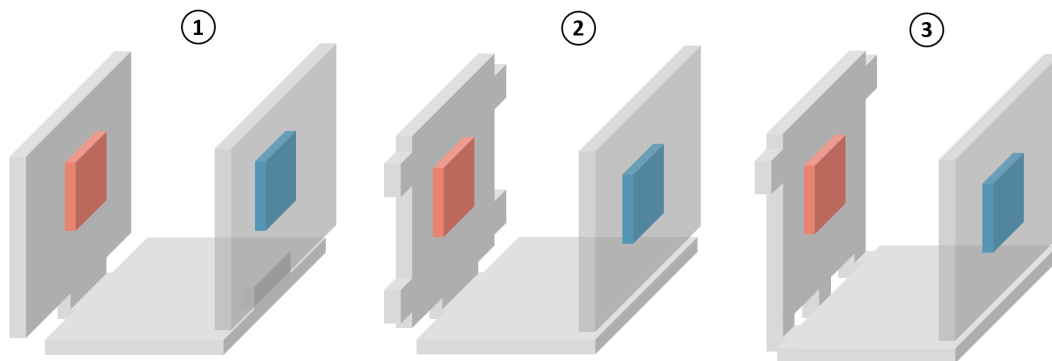


Figure 4.22: Schematic Representation of the three created housing concepts.

An important difference between concept one with concepts two and three is that concept one is a simple square, while concepts two and three feature a slightly more complex shape that acts as leaf springs when attached to the satellite frame. The leaf springs act as a local decrease in stiffness, which enables the possibility of locating and calculating the maximum stress in the housing plate.

In concept one, the housing plate is connected to the radiator plate, while concepts two and three have no direct connection between the two components. The main advantage of adding this connection is rigidity, while the main disadvantage is that thermal energy could be conducted into the radiator plate through a different route than through the fluidic loop.

The difference between concepts two and three is that in concept two the connection point of the two sheet metal plates is made in the middle, while concept three connects the plates in two locations on the outsides of the plate. Concept two features four connection points with two on each side, while concept three features three connection points on three different sides.

By examining each of the concepts based on relevant factors like rigidity, thermal insulation and overdetermination, the most suitable concept is selected to be concept three. This concept combines rigidity through the two connections between the sheet metal plate with thermal insulation from the radiator plate the best. Next to that, it also utilizes leaf springs to be able to locate the stress concentrations. Finally, this concept features a leaf spring connection on three different sides which distributes the stresses and deformations over the entire plate.

5 Detailed Design

This Chapter of the report entails the detailed design process of the in-orbit demonstration. It features calculations and simulations that are utilized to turn the concepts of Chapter 4 into a final design. At the end of this chapter, a brief overview of the final design layout can be found.

5.1 Radiator Design

The radiator plate, which is the most relevant heat sink in the system, governs the amount of energy that can be removed from the system. This directly affects the amount of energy that can be put into the system without causing it to overheat. To estimate the radiating power and system equilibrium temperature, this section features an overview of the incoming and outgoing energies, a radiator coating selection, and a simplified equilibrium temperature analysis. Next to these thermal analyses, it also includes a section that looks further into the mechanical connection of the radiator plate to the satellite frame.

5.1.1 Energy Balance of the Radiator Plate

In space, the concentration of gasses is so low, that even in low Earth orbit an ultra-high vacuum of only $5.0 \cdot 10^{-10}$ torr can be measured. This abundance of gasses makes it impossible for significant amounts of heat to be transferred to the surroundings of the CubeSat using conduction or convection. Knowing this, the only method of energy dissipation to the environment that remains is radiation.

All surfaces with a temperature above absolute zero (0 K) emit thermal radiation in the form of electromagnetic waves with a wavelength between approximately 0.1 and 100 μm . The heat transfer rate of a perfectly emitting body can be determined using the equation

$$\dot{Q} = \sigma_b AT^4, \tag{5.1}$$

which is known as the Stefan Boltzmann law. Every real surface on Earth emits less than the ideal surface of a black body. This difference in emissivity is represented by the emissivity factor, which is a factor that divides the amount of energy that a surface emits by the amount of energy that it would emit if it were to be a black body. By multiplying by this emissivity factor like in the equation

$$\dot{Q} = \epsilon \sigma_b AT^4, \tag{5.2}$$

the actual output radiative heat transfer rate of a body can be determined. In the ideal situation, the radiator would only absorb energy from the flow of fluid and radiate it into space. However, in reality, the radiator is subjected to other energy inflows like radiation from the sun, Earth, and space. These values vary during the orbit of the CubeSat, depending on the location and orientation of the satellite with respect to the sun and the Earth. Figure 5.1 shows a schematic overview of the different types of radiation sources that the satellite is exposed to during its orbit.

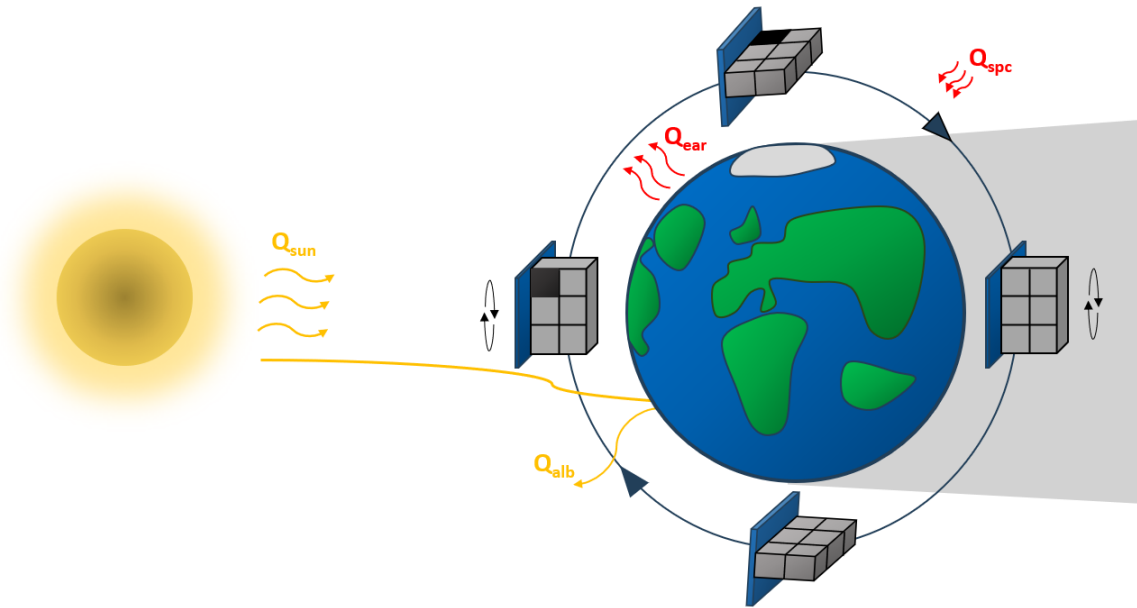


Figure 5.1: Schematic Representation of the different Scenarios of incoming Radiation during the Satellites Orbit.

The incoming external energy sources at the radiator plate are direct sun radiation, reflected sun radiation, IR Earth radiation, and IR space background radiation. The only outgoing energy source is the radiation from the radiator itself into space [13]. Both the incoming- and outgoing radiation sources depend on the location and orientation of the radiator with respect to Earth and the sun. Figure 5.2 shows the satellite orbit that is plotted in Matlab using information provided by the system integrator. The blue vector in this figure shows the direction of the sun, while the red vector represents the normal vector of the radiator surface. This orbit is used in further radiator calculations.

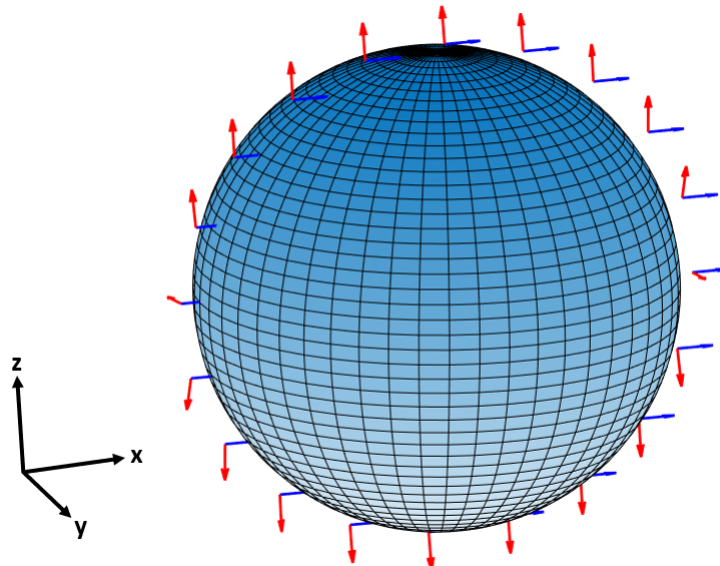


Figure 5.2: Orbit of the Satellite, with the Blue Arrows pointing in Sun Direction and the Red Arrows showing the Normal Vectors of the Radiator.

The figure shows that the normal vector of the radiator surface mostly points in the $+z$ or $-z$ direction, which is advantageous to the temperature control of the radiator since the vector is

pointing away from the Earth and perpendicular to the sun vector. The satellite remains in its sun-pointing orientation during daylight while it points nadir during eclipse. When the satellite approximately reaches the equator, it rotates 180 degrees over the x-axis, as shown in Figure 5.2, to rotate the radiator's normal vector away from Earth again. In this section, all different incoming radiation sources are separately discussed and calculated to finally gain more insight into the system temperature during consecutive orbits.

Sun Radiation In our solar system, the main source of radiation is sun radiation. It is one of the most important sources of life on Earth and provides the Earth with a power intensity between 1326 and 1418 $\frac{W}{m^2}$ depending on the location of Earth with respect to the sun. The energy gained from the sun consists of a large spectrum of wavelengths reaching from ultraviolet to infrared, which is visualised in Figure 5.3.

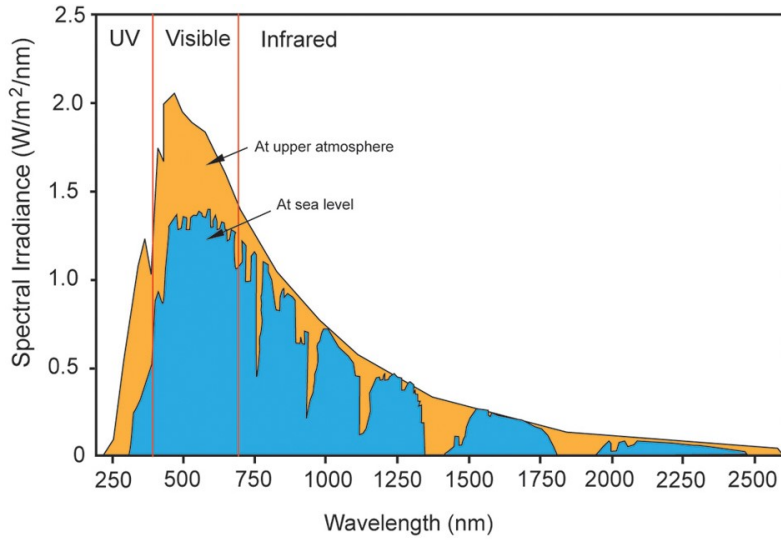


Figure 5.3: The Spectral Irradiance $[\frac{W}{m^2 \cdot nm}]$ of the Solar Spectrum in the upper Atmosphere and at Sea-level.

The amount of energy that is received from direct sunlight by an object close to Earth is calculated using the equation

$$\dot{Q}_{\text{sun}} = \alpha_{\text{rad}} A_{\text{rad}} G_{\text{sun}} \cos(\theta). \quad (5.3)$$

In this equation the angle θ refers to the angle that the normal vector of the surface of the radiator makes with the sun vector. When taking a closer look at Figures 5.1 and 5.2, it becomes clear that the radiator normal is almost always at an angle of 90 degrees with the sun vector which would reduce Equation (5.3) to be zero. Moreover, during the full orbit of the satellite, the radiator surface is shaded by the solar panel that is attached to the front of the satellite. Due to these two observations, it is safe to assume that the radiator will never be hit with direct sunlight.

Next to direct sunlight, there is also sunlight that is reflected from Earth into space, which could be directed to the radiator's surface. The phenomenon of a surface reflecting a certain percentage of the incoming sunlight intensity is called the Albedo effect. Some surfaces have a higher Albedo than other surfaces due to the difference in solar absorptivity and reflectivity. For instance, a white surface like snow will reflect relatively more light back into space when compared to a patch of grass, due to the higher reflectivity of the snow. To simplify the calculation of light that is being reflected from Earth back into space, the Earth is considered to have an overall

Albedo of 0.3 [14]. The amount of energy received by the radiator plate surface as a result of the Albedo effect is given by the equation

$$\dot{Q}_{\text{alb}} = \alpha \alpha_{\text{rad}} A_{\text{rad}} G_{\text{sun}} F_{\text{ear}} \cos(\beta), \quad (5.4)$$

in which the albedo factor, the absorptivity of the radiator coating, the radiator area, the sun intensity, the view factor of the radiator plate towards Earth, and the angle of the Earth with the center of the radiator surface are taken into account. Figure 5.4 schematically shows how the angles of θ and β which are used in Equations 5.3 and 5.4 are derived.

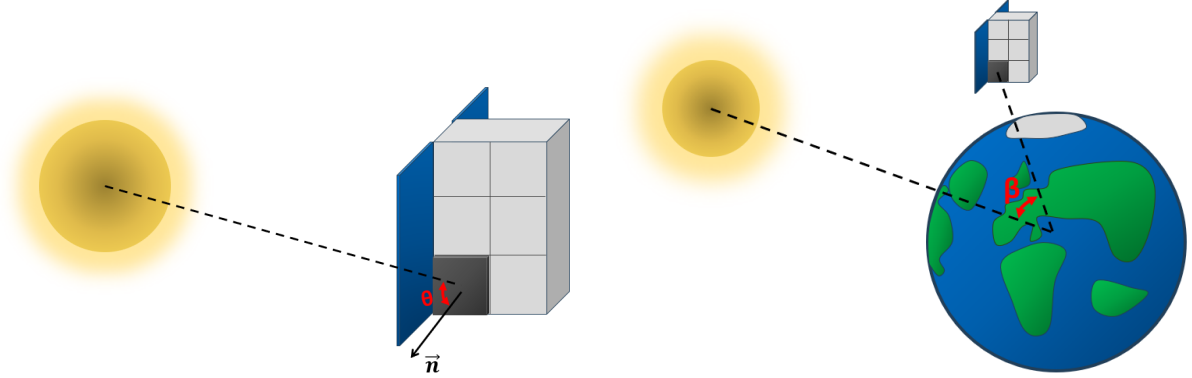


Figure 5.4: Schematic Representation of the Derivation of the angle θ and β . [15]

In Equation (5.4), the factor F_{ear} refers to the view factor of the radiator towards Earth which can be compared to the view factor for the backside of a small planar surface tilted to a sphere. Figure 5.5 shows a schematic representation of the situation along with important dimensions.

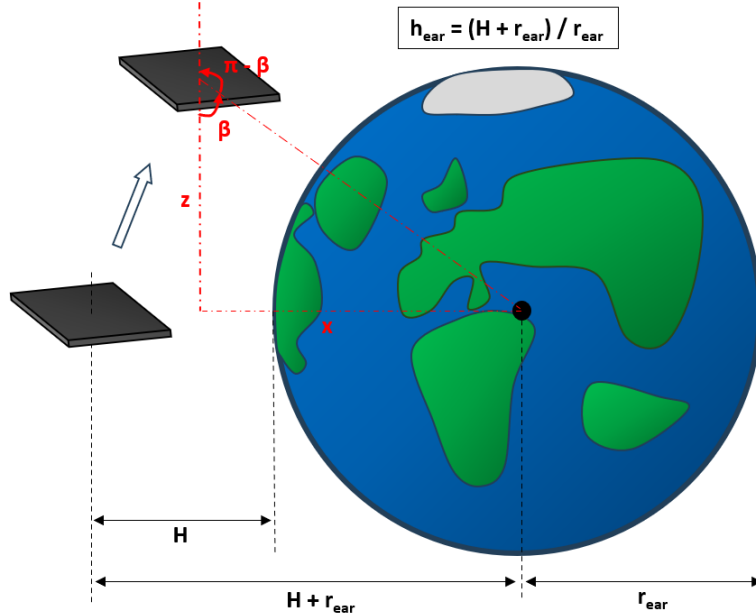


Figure 5.5: Schematic Representation of the View Factor Calculation of a Small Planar Surface tilted to a Sphere. [16,17]

If the aim was to calculate the view factor of the panel face that is pointing towards Earth, the angle β in Figure 5.5 would be used. However, since the radiator's normal vector is always pointing in the $+z$ or $-z$ direction, the calculation has to be performed for the backside of the panel surface. In this case, the angle of $\pi - \beta$ has to be used during the view factor calculations.

If the plane of the radiator surface does not intersect with the sphere, which in this case is Earth, the view factor of the back of the plane to Earth is equal to zero. If this plane does intersect with Earth, the view factor is calculated using the equation

$$F_{\text{ear}} = \frac{1}{\pi h_{\text{ear}}^2} \left(\cos(\beta) \arccos(y) - x \sin(\beta) \sqrt{1 - y^2} \right) + \frac{1}{\pi} \arctan \left(\frac{\sin(\beta) \sqrt{1 - y^2}}{x} \right), \quad (5.5)$$

in which $x = \sqrt{h_{\text{ear}}^2 - 1}$ and $y = -x \cot(\beta)$. Using Equations 5.3, 5.4, and 5.5, the incoming solar radiation can be calculated at all given satellite positions during its orbit.

Infrared Earth Radiation As stated before, all bodies with a temperature above 0 Kelvin radiate infrared radiation to their surroundings. This rule also applies to the surface of Earth, which covers a large portion of the field of view of the satellite. The amount of infrared radiation that is radiated from Earth towards the radiator surface is calculated using the equation

$$\dot{Q}_{\text{ear}} = \epsilon_{\text{rad}} A_{\text{rad}} G_{\text{ear}} F_{\text{ear}} \frac{4\pi r_{\text{ear}}^2}{4\pi (H + r_{\text{ear}})^2}. \quad (5.6)$$

In this equation, the view factor calculated using Equation (5.5) is used again. Moreover, the intensity of the infrared radiation at the surface of Earth is multiplied by the surface area of Earth and divided by the surface area of a sphere with a radius that is equal to the radius of Earth plus the orbital altitude of the satellite. Figure 5.6 shows a representation of the decrease in intensity due to the increase in altitude of the satellite.

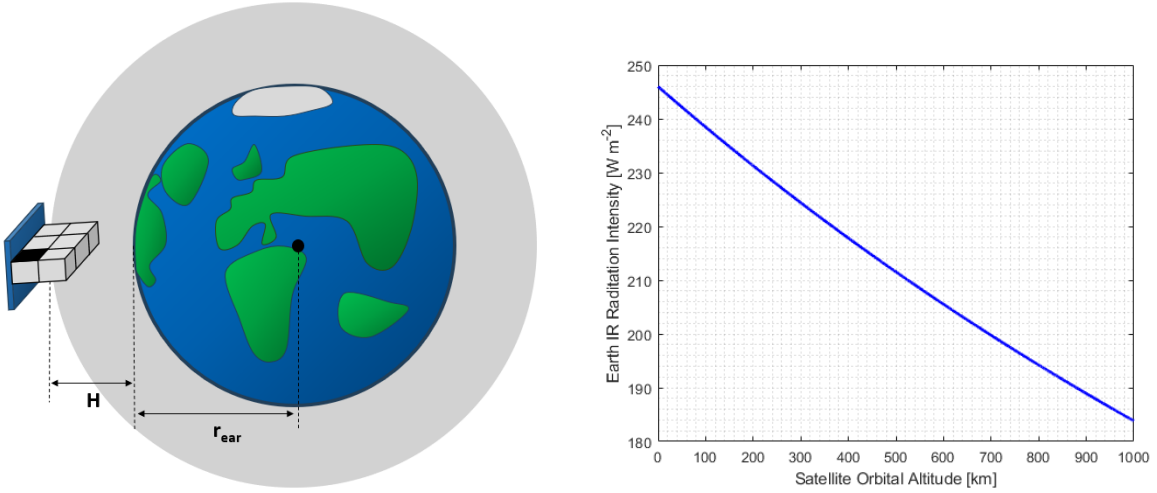


Figure 5.6: The Earth IR Radiation Intensity with respect to the Satellite Orbital Altitude.

Internal Radiation Next to radiation observed from external bodies, the radiator also receives radiation from another component within the system. In this particular case, the radiator receives radiative energy from the solar panel, that is attached to the front of the CubeSat. The radiative heat transfer that takes place between the two surfaces is calculated using the equation

$$\dot{Q}_{\text{slp}} = \epsilon_{\text{rad}} \epsilon_{\text{slp}} \sigma_b A_{\text{rad}} F_{\text{slp}} (T_{\text{slp}}^4 - T_{\text{rad}}^4), \quad (5.7)$$

in which the emissivity of both the solar panel and the radiator plate are taken into account. Additionally, the area of the radiator plate, the view factor of the radiator plate to the solar panel, and the temperatures of both surfaces are included. The view factor F_{slp} can be compared

to the calculation of the view factor of two perpendicular rectangular surfaces. Figure 5.7 shows a representation and important dimensions that are used to calculate this view factor.

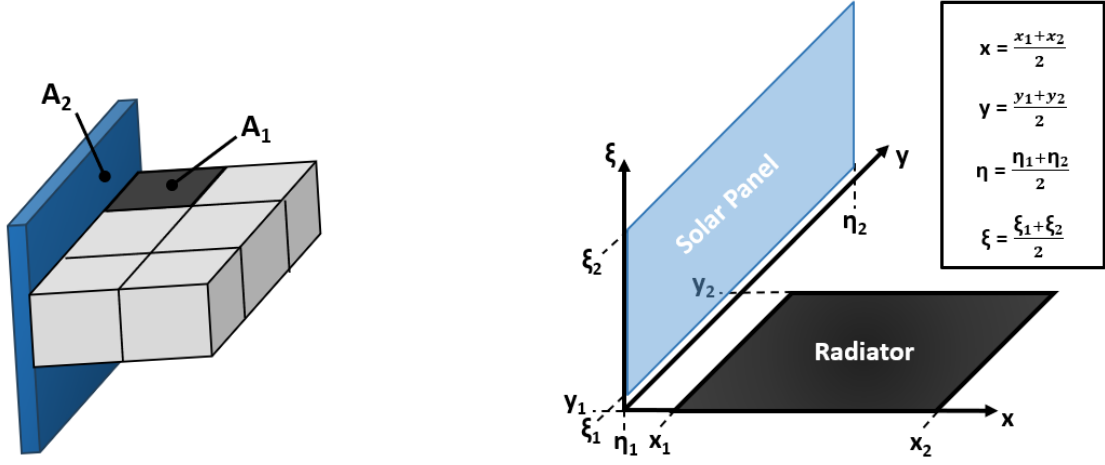


Figure 5.7: Representation and Dimensions for the Calculation of the View Factor of the Radiator to the Solar Panel. [16,17]

The view factor between the radiator plate and the solar panel is calculated using the equation

$$F_{slp} = \frac{1}{2\pi A_1} \sum_{l=1}^2 \sum_{k=1}^2 \sum_{j=1}^2 \sum_{i=1}^2 [(-1)^{(i+j+k+1)} B(x_i, y_j, \eta_k, \epsilon_l)], \quad (5.8)$$

in which $A_1 = (x_2 - x_1)(y_2 - y_1)$ and

$$B(x_i, y_j, \eta_k, \epsilon_l) = (y_j - \eta_k) C \arctan(D) - \frac{C^2}{4} (1 - D^2) \ln[C^2(1 + D^2)]. \quad (5.9)$$

In Equation 5.9, $C = \sqrt{x_i^2 + \epsilon_l^2}$ and $D = \frac{y_j - \eta_k}{C}$. Since the position and orientation of the radiator with respect to the solar panel do not change during operational use, the view factor stays constant during its full orbit. A simplification is made by assuming a constant solar panel temperature of 120 °C, which is a worst-case scenario in a simplified study performed by the system integrator [18]. Using the view factor, Equation 5.7 can be filled in to calculate the radiative heat transfer that takes place between the surface of the radiator plate and the solar panel.

Radiator Radiation To dissipate the energy that is gained from all external sources mentioned earlier in this chapter as well as the internal heat generation, the radiative properties of the radiator are used. The outside surface of the radiator is coated in a paint that has a low absorptivity and a high emissivity to lose heat as efficiently as possible. As has been stated in Section 4, the area of the radiator that is aimed at deep space is 77 by 77 mm. This is the area that is used in further calculations to approximate the temperature of the radiator during multiple consecutive orbits. To calculate the amount of energy that is dissipated into space through the radiator plate the equation

$$\dot{Q}_{rad} = \epsilon_{rad} \sigma_b A_{rad} F_{rad} (T_{rad}^4 - T_{spc}^4), \quad (5.10)$$

in which the emissivity of the radiator, the view factor of the radiator into deep space, and the temperatures of the radiator and deep space are used.

The view factor F_{rad} , which is calculated using the equation

$$F_{rad} = 1 - F_{slp}, \quad (5.11)$$

is assumed to include the entire view of the radiator plate into space, except for the directions in which it views the solar panel. It could be argued that this view factor should also take into account the directions in which the radiator has Earth inside its viewing range. However, the amount of energy that is absorbed by Earth is already taken into account using Equation (5.6), which means that the view factor of the radiator towards Earth can be included in the view factor that stares into deep space.

5.1.2 Radiator Coating Selection

The function of the radiator plate is to dissipate energy into space through radiation. To increase the efficiency of this process, the radiator surface is covered in a coating that is used to increase the surface emissivity and decrease its absorptivity to the solar spectrum shown in Figure 5.3.

To survive the lifetime of the experiment, which is three years, the coating should be able to cope with atomic oxygen erosion and UV degradation during many thermal cycles.

Atomic oxygen erosion occurs when molecular oxygen is split into single oxygen molecules by a process called photo-dissociation. At an altitude of 400 km, which is within the boundaries of low Earth orbit, these single oxygen molecules make up about 96% of the present gasses [19]. When these single oxygen molecules collide with a surface on the structure in low Earth orbit, they are capable of breaking chemical bonds of the material in question, which causes the material to erode [20]. When the coating erodes, this may alter its optical properties, which in turn causes the thermal control of the system to be disrupted.

In low Earth orbit, around 8% of the solar constant, which is defined as the total energy produced by the sun over all wavelengths, falls within the range of approximately 0.1 - 0.4 μm . This range of wavelengths is known as solar ultraviolet radiation, which harbours enough energy to break certain organic bonds. Breaking these bonds causes certain coatings to degrade, which alters their optical properties.

In two separate researches performed by NASA, several different types of radiator coatings have been exposed to light that represents the solar spectrum at elevated temperatures to test the degradation of the coating material and the change in their optical properties [21, 22]. The research shows that zinc oxide/potassium silicate is found to be the coating with the best resistance to UV degradation of the tested coatings. The superior resistance to UV degradation is shown by the relatively low increase of solar absorption and the relatively low decrease of thermal emittance of the zinc oxide/potassium silicate coating [22].

A coating that has been used on the international space station for over ten years is AZ-93. This white inorganic zinc oxide/potassium silicate coating is thoroughly tested and has shown only 0.01 overall degradation in solar absorbance after a flight of 5.8 years on the long-duration exposure facility [23]. Table A.2 gives an overview of the properties of the AZ-93 coating. These properties are used in the initial equilibrium temperature calculations of Section 5.1.3 as well as in the thermal system analysis in Chapter 6.4.

5.1.3 Initial Equilibrium Temperature Calculations

During the experiment of the in-orbit demonstration, two operating modes are defined. The first mode is known as operational mode, while the second mode is known as idle mode. In operational mode, the heat source, the accumulator heater, the drive electronics, and the micro-pump are all powered on to show the heat transfer capabilities of the experiment. In idle mode, only the accumulator heater and the drive electronics are powered on, to make sure that the accumulator always stays at the required temperature. For this initial equilibrium temperature calculation, only the worst-case scenario for cooling, which is the operational mode, is analysed. To perform this calculation, the assumption is made that the system is a cube with a volume

of 1U, a mass of 1.0 kg and the specific heat capacity and thermal conductivity of titanium. The selected weight is based on the maximum allowed weight of the design and the specific heat capacity and thermal conductivity are selected since the main components are made of mainly titanium. Moreover, the only radiative area of this cube is considered to be the radiator surface, since the rest of the cube sides are assumed to be covered in multi-layered material (MLI) that functions as a shield to radiation. More information on the topic of MLI can be found in Section 5.6.2.

Using all incoming and outgoing energy sources found in Section 5.1.1, and adding the internally generated energy, the energy balance over the radiator surface is described in by the relation

$$\dot{Q}_{\text{tot}} = \dot{Q}_{\text{in}} - \dot{Q}_{\text{out}} = \dot{Q}_{\text{sun}} + \dot{Q}_{\text{alb}} + \dot{Q}_{\text{ear}} + \dot{Q}_{\text{slp}} + \dot{Q}_{\text{int}} - \dot{Q}_{\text{rad}}. \quad (5.12)$$

The internally generated energy consists of multiple different energy sources like the heater, the accumulator heater, the drive electronics and the pump. During the simulation, all of these components are assumed to be powered on during the entire orbit, which is known as the operational mode. Additionally, the simulation assumes that all power that is produced by these heat sources reaches the radiator plate, which means that no heat losses throughout the loop are assumed. In the real case scenario, the system will also lose heat throughout other parts in the loop due to conduction into the satellite frame. Therefore, the actual equilibrium temperature is lower than the one found in the simulation. In addition, the time that it takes for the system to reach its equilibrium temperature will differ from reality, since the actual design will consist of multiple different materials with different geometries. Therefore, this simulation can only be used as an estimation to calculate the equilibrium temperature in the worst-case scenario, while it only gives a rough estimation of the time it takes for the system to reach this temperature. When the system is in equilibrium, \dot{Q}_{tot} is equal to zero.

If the energy balance is calculated for all locations in the orbit, in small time steps, the equation

$$\frac{dT}{dt} = \frac{\dot{Q}_{\text{tot}}}{m_{\text{sys}}c_p}, \quad (5.13)$$

helps in finding the change in temperature during a specific timestep. The smaller the time increments are, the more accurate the simulations are. Equation 5.13 assumes a uniform change in temperature over the entire cube of material. Such an analysis is called a lumped system analysis and can only be justified if the Biot number is below 0.1. The Biot number is a dimensionless number that is calculated using the equation

$$\text{Bi} = \frac{h L_{\text{vs}}}{k}, \quad (5.14)$$

in which the external heat transfer of a body is compared to the internal heat transfer of a body. If the internal heat transfer of the body is at least ten times higher than the external heat transfer of the body, it is safe to assume that the temperature throughout the body is approximately uniform. In this equation, h represents the external heat transfer coefficient, k represents the internal heat transfer coefficient, and L_{vs} represents the volume of the body divided by the area of the body, which is known as the characteristic length. In this specific case, it is found that the Biot number stays well below 0.1 throughout the full orbit of the satellite, which is common for relatively small bodies of metal in the vacuum of space. Therefore, the lumped system analysis is justified and has been used for further analysis into the equilibrium temperature of the system.

Since the radiator is the only component in the system that is used to dissipate significant amounts of energy, it therefore decides the amount of energy that can be put into the system

without overheating. This means that the power rating of the heater within the mini-MPL is selected mainly based on the specifications of the radiator. Figure 5.8 shows the final results of the simulation that has been created using Matlab to calculate the equilibrium temperature of the system for several different heater input energies. The simulation starts at the selected initial temperature of $-40\text{ }^{\circ}\text{C}$ and ends after 10 orbits, which is found to be enough time for the system to reach its equilibrium temperature in the simulation.

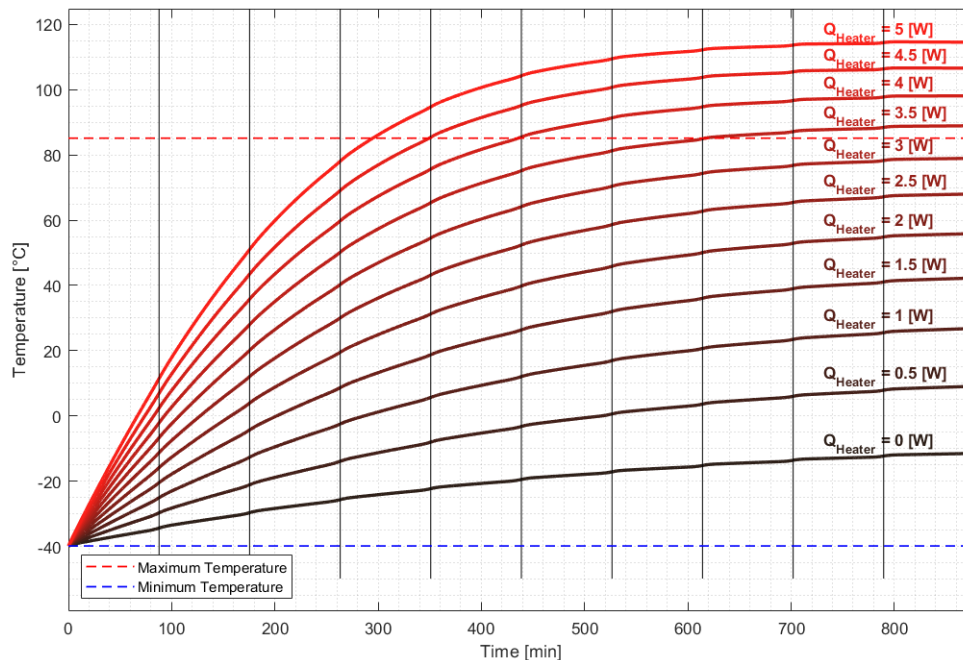


Figure 5.8: Temperature Simulations of the Radiator for different Heater Input Powers.

From the thermal analysis, it is found that the radiator plate stays within the minimum and maximum temperature with a heat source of a maximum of 3.0 W if no heat is lost throughout the system. This information does not directly exclude higher heater powers due to the limitations of this simulation but is taken into account during the heat source selection in Section 5.5.

5.1.4 Mechanical Connection of the Radiator Plate

To mount the radiator to the Frame of the CubeSat, multiple bolted connections are used. Figure 5.9 shows the availability of the holes to connect the radiator plate to the satellite frame. Highlighted in red are all holes that are not available to be used. The column of holes on the left is unavailable due to the connection of the solar panel to the frame. This connection utilizes hinges that block three of the holes on the left in the figure. The four smaller holes in each corner are also unavailable to be used since these holes are meant to attach panels to the outside of the frame. Moreover, the four holes in the top and bottom row that are marked yellow can best be avoided, since they are hard to reach. The difficulty in reaching these holes is created by the small 2.14 mm holes that feature a heightened surface on the inside of the frame. Since the radiator is mounted on the inside of the frame, this surface might cause interference if the 2.9 mm holes in the corners are used.

All holes that are not highlighted in red or yellow can be used to attach the radiator plate to the satellite frame. Figure 5.10 shows the design of the radiator plate. The bolted connections that facilitate the connection have been selected and analysed in Section 5.6.

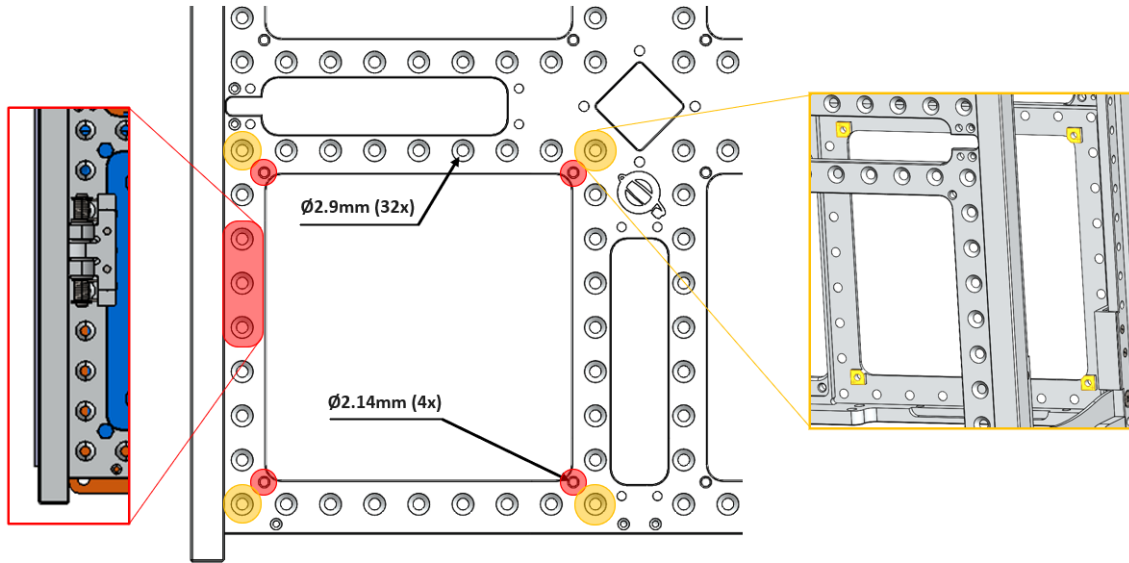


Figure 5.9: Available Holes to connect the Radiator to the Frame.

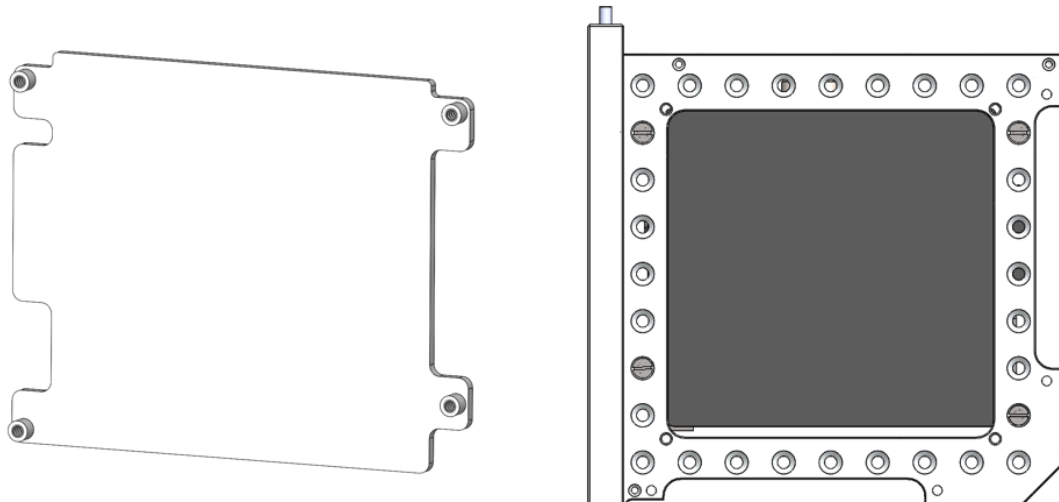


Figure 5.10: Design of the Radiator Plate and its connection to the Satellite Frame.

5.2 Heat Exchangers Design

This section entails the detailed design of both the heat exchanger on the heat source- and the heat sink side. Firstly, the heat exchangers are resized to fit within the in-orbit demonstration. Secondly, a brief thermal- and fluidic analysis is performed based on the model of NLR [24], to show the workings of the offset-strip heat exchanger dependent on the fin geometry. Then, the fin geometry is designed based on an optimisation for the heat transfer coefficient and pressure drop. Finally, the mechanical connections of the heat exchangers are designed to fully integrate the component into the system.

5.2.1 Resizing of the Heat Exchangers

The previously designed heat exchanger of NLR has been designed to transport approximately 40 - 100 W of power. In the current design, a heat source of a maximum of 5.0 W is used, which significantly reduces the amount of power that the heat exchanger has to transport. Therefore, the heat exchanger can be scaled down to reduce the volume and weight of this component, while

still being able to transport the required amount of thermal energy. However, two drawbacks of decreasing the size of the heat exchanger are that the pressure drop will increase and the contact area of the heat exchanger with the radiator plate will decrease. This second drawback might cause a temperature concentration on the radiator plate, which reduces the efficiency of the radiator.

After a concise optimisation, the outer dimensions of the heat exchanger are selected to be 30 by 30 mm. This choice has been made to ensure that the heat exchangers fit within the in-orbit demonstration, while still leaving space to be able to make a fluidic connection. Figure 5.11 shows rough dimensions of the externals of the new design.

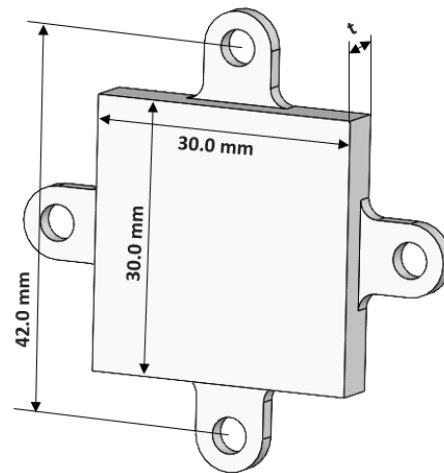


Figure 5.11: General Dimensions of the Heat Exchangers.

The dimensions that have not yet been selected are the thickness of the heat exchanger as well as the dimensions of the fins within the heat exchangers. These dimensions are selected using an optimisation that is found in Section 5.2.4.

5.2.2 Thermal Analysis of the Offset-Strip Fin Heat Exchangers

In this section, the offset-fin strip heat exchanger is thermally analysed based on fin dimensions. Figure 5.12 shows the geometry and geometric ratios α , δ , and γ that play an important role in the calculation of the heat transfer coefficient for offset-strip fin strip heat exchangers.

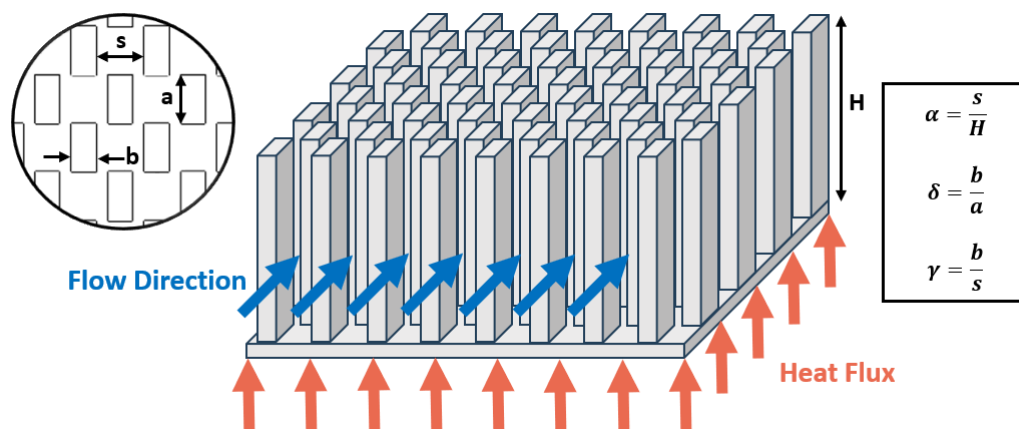


Figure 5.12: Important Geometrical Parameters to calculate the Heat Transfer Coefficient of an Offset-Strip Fin Heat Exchanger. [25]

To calculate the thermal resistance of any heat exchanger, the relation

$$R = \frac{1}{hA}, \quad (5.15)$$

can be used. In this equation, the R represents thermal resistance, h represents the heat transfer coefficient and A represents the area over which the heat transfer takes place.

The area of convective heat transfer is considered to be the area of the fins together with the area of the internal walls of the heat exchanger. The heat transfer coefficient 'h', is calculated using the equation

$$h = \text{Nu}_{D_h} \frac{k_f}{D_h}, \quad (5.16)$$

and is dependent on many different factors like the heat exchanger geometry, fluid velocity, fluid properties, and heat exchanger material properties. In Equation 5.16, k_f represents the thermal conductivity of the fluid. The Nusselt number, calculated using the equation

$$\text{Nu}_{D_h} = j \text{Re}_{D_h} \text{Pr}^{\frac{1}{3}}, \quad (5.17)$$

is a dimensionless number that describes the non-dimensional temperature gradient at the interface of the solid fins and the working fluid [25, 26]. In this case, the Nusselt number, along with the Reynolds number are calculated using the hydraulic diameter, which for the offset-strip fins can be calculated using the equation

$$D_h = \frac{4sHa}{2(sa + Ha + bH)}. \quad (5.18)$$

In Equation (5.17), the factor j is known as the Colburn factor. In the case of an offset-strip fin heat exchanger, this factor can be calculated using the relation

$$j = 0.6522 \text{Re}_{D_h}^{-0.5403} \alpha^{-0.1541} \delta^{0.1499} \gamma^{-0.0678} (1 + 5.269 \cdot 10^{-5} \text{Re}_{D_h}^{1.340} \alpha^{0.504} \delta^{0.456} \gamma^{-1.055})^{0.1}, \quad (5.19)$$

and is dependent on the geometry of the heat exchanger and the Reynolds number [25]. The two factors that remain are the Reynolds number and the Prandtl number. The Reynolds number is a dimensionless number that is calculated using the equation

$$\text{Re}_{D_h} = \frac{\rho_f \langle v_f \rangle D_h}{\eta_f} = \frac{\langle v_f \rangle D_h}{\nu_f}, \quad (5.20)$$

and that describes the ratio of inertial forces to viscous forces within a fluid to determine whether a fluid behaves as laminar, transitional, or turbulent. The Prandtl number, which is also a dimensionless number described by the relation

$$\text{Pr} = \frac{\eta_f c_p}{k_f}, \quad (5.21)$$

describes the ratio of momentum transfer of the fluid to the thermal conductivity of the fluid. The average fluid velocity in Equation (5.20) is determined by dividing the volume flow of fluid by the free flow area between the fins within the heat exchanger. By combining Equations (5.16) - (5.21), the heat transfer coefficient and the thermal resistance of the heat exchanger can be calculated. This method is used in Section 5.2.4 to optimize the heat exchanger design.

5.2.3 Fluidic Analysis of the Offset-Strip Fin Heat Exchangers

The geometry in an offset-strip fin heat exchanger causes the fluid to follow a specific path through the heat exchanger. The pressure drop over the heat exchanger is calculated using the equation

$$\Delta p = \frac{\rho_f \langle v_f \rangle^2}{2} \left((K_{\text{con}} + 1 + \sigma^2) + f \frac{4a}{D_h} - (1 - \sigma^2 - K_{\text{exp}}) \right), \quad (5.22)$$

which is a specific relation that describes the pressure drop for an offset-strip fin heat exchanger with the dimensions explained in Figure 5.12 [26]. In this equation $\sigma = \frac{s-b}{s}$. K_{con} represents the coefficient of abrupt contraction and is calculated using the equation

$$K_{\text{con}} = -0.4446\sigma^2 + 0.0487\sigma + 0.7967, \quad (5.23)$$

while K_{exp} represent the coefficients of abrupt expansion and is calculated using the equation

$$K_{\text{exp}} = 0.9732\sigma^2 - 2.3668\sigma + 0.9973. \quad (5.24)$$

The last unknown that remains in Equation (5.22) is the friction factor. This factor is calculated using the equation

$$f = 9.6243 \text{Re}_{D_h}^{-0.7422} \alpha^{-0.1856} \delta^{0.3053} \gamma^{-0.2659} (1 + 7.669 \cdot 10^{-8} \text{Re}_{D_h}^{4.429} \alpha^{0.920} \delta^{3.767} \gamma^{0.236})^{0.1}, \quad (5.25)$$

and represents the pressure loss of the fluid through the heat exchanger [25, 26]. By using Equation (5.22) - (5.25) the pressure drop within the heat exchangers can be calculated. This method is used in Section 5.2.4 to optimize the heat exchanger design.

5.2.4 Performance optimisation of the Heat Exchangers

To find the most efficient fin geometries for the selected heat exchanger size, a performance optimisation is carried out using Matlab. As an input for the optimisation, a range of lengths, widths, and heights of the fins are selected. Using these values, the simulation calculates the pressure drop and the heat transfer coefficient of the heat exchanger using the thermal- and fluidic analyses described in Sections 5.2.2 and 5.2.3 respectively. All analyses are carried out with a mass flow of $0.7 \frac{\text{g}}{\text{s}}$, which is based on the pump performance tests described in Section 4.1.3.

The geometry limitations of this optimisation are based on the tolerance of the metal 3D printer that is used to manufacture both heat exchangers and on the size and weight limitation of the component within the in-orbit demonstration. Figure 5.13 gives an overview of several constraints of the optimisation simulation. The constraints of the optimisation are that the length of a fin should be larger than the width of the fin, the distance between fins in the same row should be twice the width of the fins and the distance between fins in adjacent rows should be half the width of the fins. Therefore, the smallest dimension within this arrangement is the distance between two fins in adjacent rows, which is given as dimension 'c' in Figure 5.13. To prevent these two fins from touching and closing the flow path with the worst-case tolerance scenario, this distance has to be equal to or larger than 0.25 mm. This also affects the minimum fin width and the minimum distance between fins in the same row. Considering all these constraints, the dimension ranges for the length and width of the fins are selected to be between 0.5 - 2.0 mm. The range of fin heights that has been selected is between 1.0 - 5.0 mm. Selecting a height below 1.0 mm would cause the pressure drop of the heat exchangers to increase significantly while selecting a height above 5.0 mm would increase the volume and weight of the heat exchangers without causing a relevant decrease in the thermal resistance.

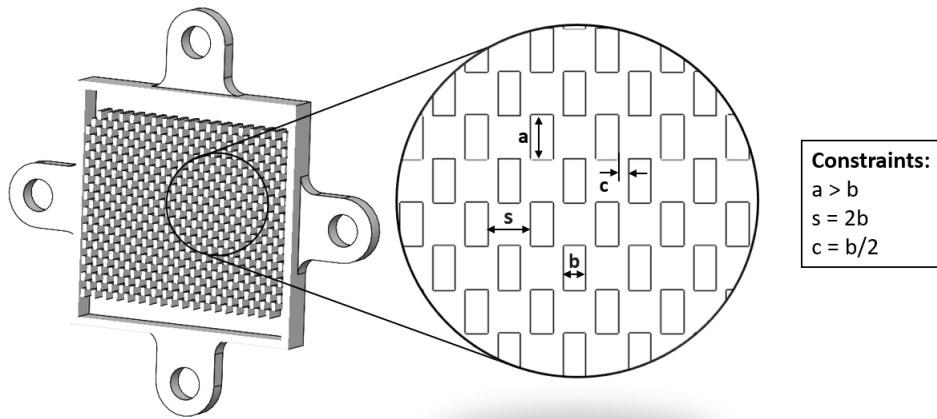


Figure 5.13: Overview of several Simulation Constraints.

Within the selected fin geometry constraints, an optimisation simulation has been performed. This simulation calculates both the pressure drop and the thermal resistance of the heat exchanger for each combination of fin geometries at ambient temperature. In Figure 5.14, the heat exchangers' pressure drop and thermal resistance are shown. The 4D plots show the length of the fins on the x-axis, width on the y-axis, and height on the z-axis. The colour bar on the right of each plot shows the pressure drop and the thermal resistance for each of the combinations of dimensions.

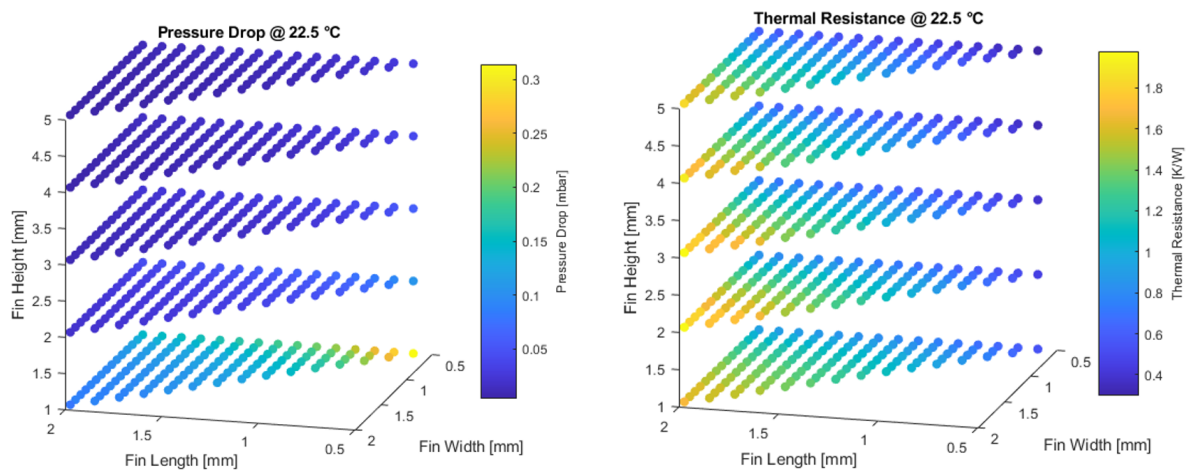


Figure 5.14: Pressure Drop and Thermal Resistance of the Heat Exchangers for different Fin Geometries at Ambient Temperature.

The figures show that smaller fin geometries cause the pressure drop to increase, while it causes the thermal resistance to decrease. Additionally, the pressure drop increases for a decreasing temperature, while the thermal resistance increases for a decreasing temperature.

The selected mass flow of the pump corresponds to a pressure drop of a maximum of 25 mbar. Since the maximum pressure drop that is found using the simulation is lower than 0.5 mbar, the heat exchangers do not have a significant share in the total pressure drop of the system. On the other hand, the thermal resistance has to be as low as possible to make sure that the thermal energy that is produced by the heat source does not experience much resistance to flow

into the radiator plate. Therefore, the thermal resistance is selected as the leading factor in the optimisation.

From the heat source to the heat sink of the system, the thermal resistance should be as low as possible. The thermal resistance between these two points in the system consists of the thermal resistance of the fluid, which is calculated using the equation

$$R_f = \frac{1}{\dot{m}_f c_p}, \quad (5.26)$$

and the thermal resistances of the two heat exchangers. To make sure that the heat exchangers do not have a large influence on the thermal resistance from the heat source to the heat sink, the combined thermal resistances of both heat exchangers are designed to be lower than half the thermal resistance of the fluid. Since this resistance is estimated to be $1.48 \frac{\text{K}}{\text{W}}$ at ambient temperature, the thermal resistance of the two heat exchangers combined should be lower than $0.74 \frac{\text{K}}{\text{W}}$. By applying this filter to the data gathered by the optimisation simulation, several fin geometry combinations are found to be matching. Table 5.1 shows the six found possibilities.

Table 5.1: Possible Fin Geometry Options.

Option	Length [mm]	Width [mm]	Height [mm]	Pressure Drop [mbar]	Thermal Resistance [$\frac{\text{K}}{\text{W}}$]	Mass [g]
1	0.6	0.5	3	0.060	0.365	4.5
2	0.6	0.5	4	0.041	0.321	6.0
3	0.7	0.5	4	0.036	0.362	6.0
4	0.6	0.5	5	0.031	0.287	6.0
5	0.7	0.5	5	0.027	0.325	7.5
6	0.8	0.5	5	0.024	0.355	7.5

From these six possibilities, the second option is selected as the most suitable. The reasoning behind this is that this option has the second lowest thermal resistance of all options while weighing less and taking up less volume. The pressure drop of option two is the second worst, but the differences are relatively small compared to the allowed total system pressure drop of 25 mbar.

To gain knowledge of the pressure drop and thermal resistance of the selected heat exchanger for the full temperature range, an extra analysis has been performed. Figure 5.15 shows the Reynolds number, pressure drop, heat transfer coefficient, and thermal resistance of the heat exchanger from -40 to 85 °C.

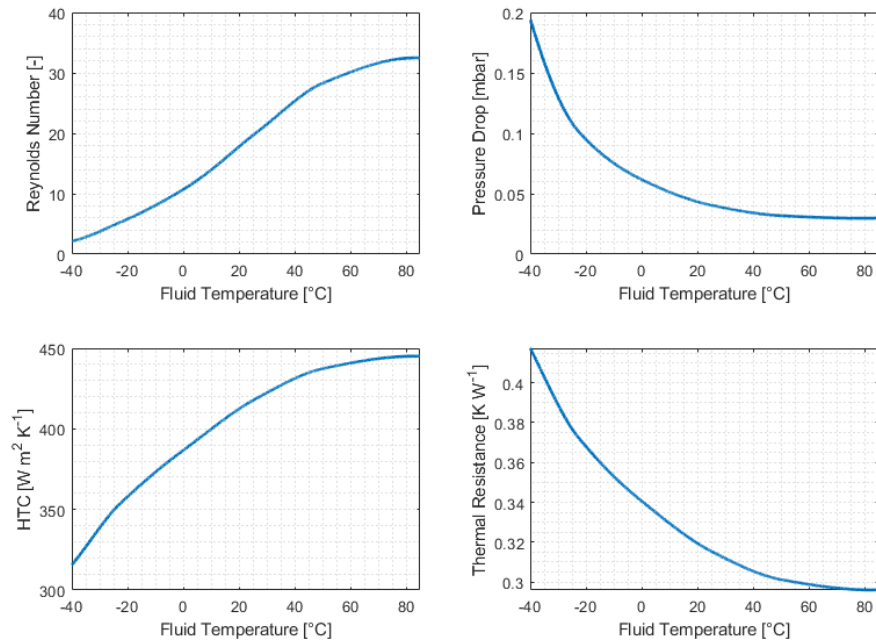


Figure 5.15: Relevant Performance Parameters of the Heat Exchangers for the full Temperature Range of the System.

From the top left graph, it becomes clear that the Reynolds number never exceeds a value of 40, which means that the flow in the heat exchangers will never become turbulent. This will prevent any unexpected vibrations from occurring. The pressure drop over the heat exchangers, which is visualized in the top right graph, shows that the pressure drop does become three times higher at $-40\text{ }^{\circ}\text{C}$ when compared to ambient temperature. However, since the allowed pressure drop over the entire system is 25 mbar, the maximum found pressure drop of around 0.19 mbar would still only amount to a small fraction of the requirement.

The two bottom graphs show the heat transfer coefficient and the thermal resistance of the heat exchangers. Something that becomes clear is that the thermal resistance is around 22% higher at $-40\text{ }^{\circ}\text{C}$ when compared to ambient temperature. Although this would cause the system to become slightly less efficient in transporting heat from the heat source to the heat sink, the increased thermal resistance is only a small fraction compared to the total thermal resistance between these two points in the system.

5.2.5 Mechanical Connection of the Heat Exchangers

The mechanical connections of the heat exchangers on the heat sink and heat source side are made differently. On the heat sink side of the in-orbit demonstration, the heat exchanger is 3D printed together with the radiator plate. This ensures a perfect thermal and mechanical connection. By adding chamfers along the edges of the heat exchanger, the effect of a heat spreader can be mimicked to a certain extent, to get closer to a uniformly distributed temperature over the radiator plate. There is no relevant downside to this connection.

On the heat source side of the in-orbit demonstration, the heat exchanger is connected to the housing, which is designed in Chapter 5.6. To facilitate this connection, the heat exchanger is equipped with two holes that are used to make a bolted connection. The disadvantage of this is that the bolted connection of the heat exchanger with the housing has to be thermally isolated. Additionally, bolted connections could detach due to vibrations if not properly designed.

Figure 5.16 shows the design of the heat exchanger on the heat sink and heat source side respectively. This figure also shows the inlet and outlet tube that are used to make a fluidic connection to the rest of the system. A more detailed explanation of the fluidic connection of the

heat exchangers and the pressure drop within the inlet and outlet tube are covered in Chapter 5.3

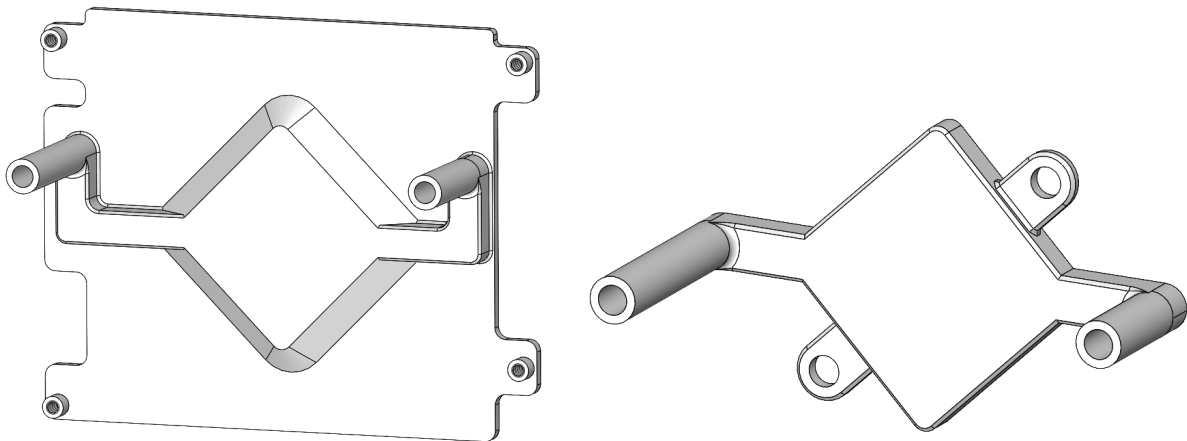


Figure 5.16: Mechanical Connection of the Heat Exchanger on the Heat Sink Side (left) and the Heat Source Side (right).

5.3 Tubing Design

Heat is transferred from the heat source to the heat sink using a working fluid that flows between components through the tubing. In this section, the routing and connecting of the tubing is designed based on a fluidic analysis.

5.3.1 Fluidic Analysis of the Tubing

Routing & Interfacing Figure 5.17 shows how the components in the system are fluidically connected and what type of bends are present in the tubing. The figure summarizes the decisions that have been made during the concept analysis in Chapter 4 that features the selection of rigid tubing, compression fittings, manifolds, and tube routing.

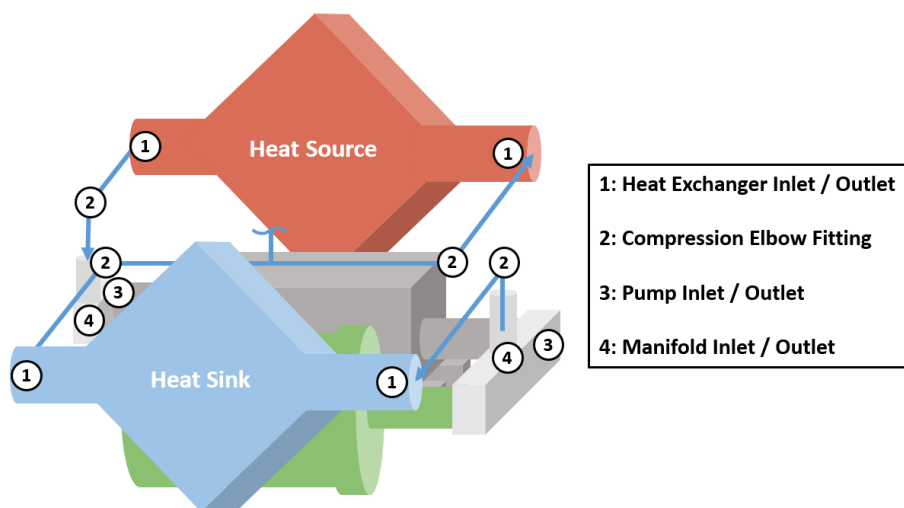


Figure 5.17: Routing of the Tubing between the different Components.

The bends at the heat exchangers are round bends with a bending radius equal to the channel diameter. Compression tube elbow fittings have been selected to connect the aluminium alloy of the heat exchangers to the titanium inlet and outlet of the pump. Inside the fittings is a

mitred bend with two welds of 45 degrees. At the inlet and outlet of the pump, a manifold is used to connect both the pump and the accumulator to the heat sink and heat source. When the fluid flows in and out of the pump it has to make a bend of 90 degrees to flow in or out of the manifold. This bend is considered to be a one-weld, mitred bend. The same type of bend is considered to be present on the inlet and outlet of the manifold, only with a different tube size. Figure 5.18 shows schematic images of the inside geometries of the bends.

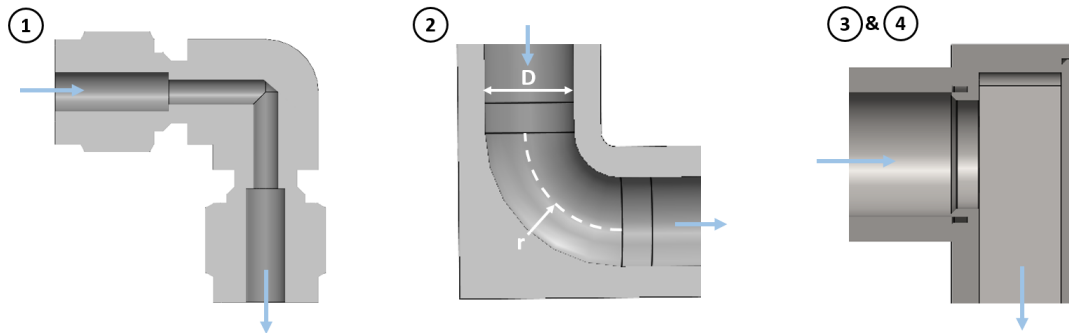


Figure 5.18: Types of Bend Geometries that are present in the System.

Tube Sizing In the ideal situation, the tubing would have an inner diameter that is as small as possible, to be able to transport the fluid quickly between components using the set mass flow, and to reduce the amount of fluid that is present in the system. Additionally, tubing with a relatively small diameter is easier to bend, which is beneficial to designing the tubing in a confined space. Two disadvantages to using tubing with a small inner diameter are an increase in pressure drop and an increase in Reynolds number. An increase in pressure drop could result in a lower flow rate of the pump and an increase in Reynolds number could result in turbulent flow, which might cause unexpected vibrations to occur within the cooling loop. Additionally, a turbulent flow would require the heat exchanger optimisation to be performed differently, since Equations 5.19 and 5.25 are only applicable for laminar flow. The Reynolds number is calculated using Equation (5.20). The pressure drop in a straight tube is calculated using the equation

$$\Delta p = f \frac{L_{tb}}{D_h} \frac{\rho_f \langle v_f \rangle^2}{2}, \quad (5.27)$$

in which the friction factor f is described by the relation $f = \frac{64}{Re_{D_h}}$ for a circular pipe.

Figure 5.19 shows the pressure drop per meter and the Reynolds number of a straight tube with a flow rate of $0.7 \frac{g}{s}$ and a varying inner diameter. Each line represents a different fluid temperature ranging from the minimum operating temperature of the system of $-40 \text{ }^\circ\text{C}$ to the maximum operating temperature of $85 \text{ }^\circ\text{C}$.

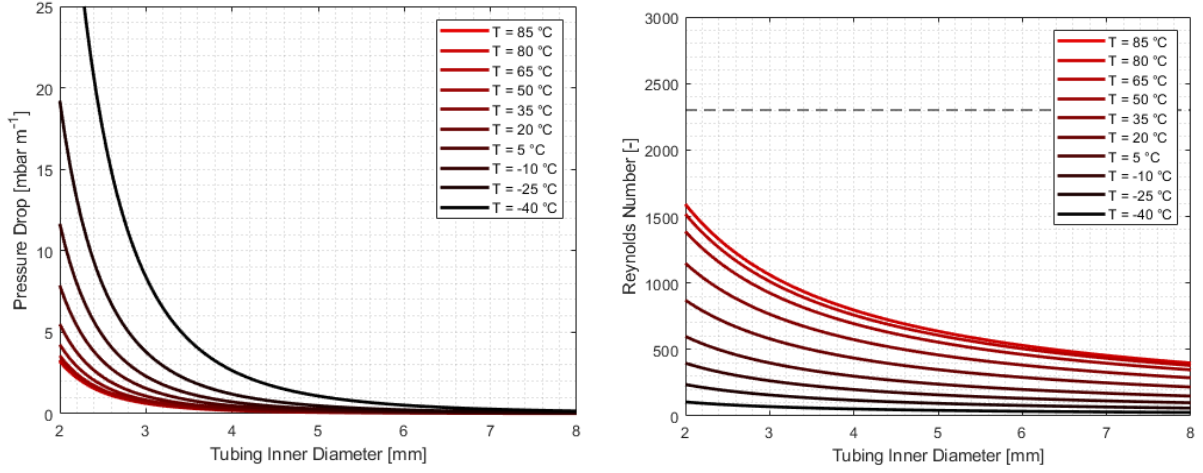


Figure 5.19: Pressure Drop per Meter (left) and the Reynolds Number (right) vs. Tubing Inner Diameter at different Fluid Temperatures.

These two graphs serve as an indicator in the selection process of the right tubing size. It can be seen that the pressure drop increases drastically at smaller tube inner diameters. Moreover, the pressure drop increases with a decreasing temperature due to a higher fluid viscosity at low temperatures. A decrease in the inner tube diameter and an increase in the fluid temperature cause an increase in the Reynolds number. The Reynolds number should stay below 2300 at the equilibrium temperature to make sure that the system does not operate within the transition- or turbulent flow regime, during normal operation. Using this information, a selection of possible tube sizes is made.

The three most suitable tube outer diameters are the 1/8, 3/16 and 1/4 inch tubing. The reasoning behind this is that a smaller tubing would most likely have a pressure drop that is too high and a bigger tubing would not fit inside the limited available space.

As can be seen in Figure 5.17, the total tubing within the system consists of several bends and straight tubing sections. To select the most suitable tubing size, a more thorough calculation is performed that estimates the total pressure drop over the entire tubing. The pressure drop over the bends in the system is calculated using the equation

$$\Delta p = K_L \frac{\rho_f \langle v_f \rangle^2}{2}, \quad (5.28)$$

in which K_L represents the loss factor of the bend, which can be calculated using several different methods. The most accurate and suitable method when performing calculations on laminar flow in relatively small piping is either the 2-K or the 3-K method [27]. The 3-K method, represented by the equation

$$K_L = \frac{K_m}{\text{Re}_{D_h}} + K_i \left(1 + \frac{K_d}{D_h^{0.3}} \right), \quad (5.29)$$

has been developed by Ron Darby as an improvement of the 2-K method and is used in further calculations. The factors K_m , K_i and K_d depend on the type of bend through which the fluid flows. Table D.1 in Appendix D shows the three factors for variations of different kinds of fittings. To calculate the total pressure drop over the cooling loop, the pressure drops over all bends and straight tubing should be summed as shown in the equation

$$\Delta p_{\text{tot}} = \sum K_L \frac{\rho_f \langle v_f \rangle^2}{2} + \sum f_{L_{\text{tb}}} \frac{\rho_f \langle v_f \rangle^2}{2}. \quad (5.30)$$

Figure 5.20 visualizes the total pressure drop of the different sizes of tubing at -40 °C on the left and 85 °C on the right. In this calculation, the system is estimated to feature 40 cm of

straight tubing, which is most likely an overestimation of the actual straight tubing length. For simplicity, the pressure drops caused by expansion or reduction of the flow path are not considered. A more accurate calculation of the total pressure drop in the system can be found in Section 6. This calculation also features the pressure drop over the heat exchangers and a more accurate calculation of the pressure drop within the manifolds and fittings.

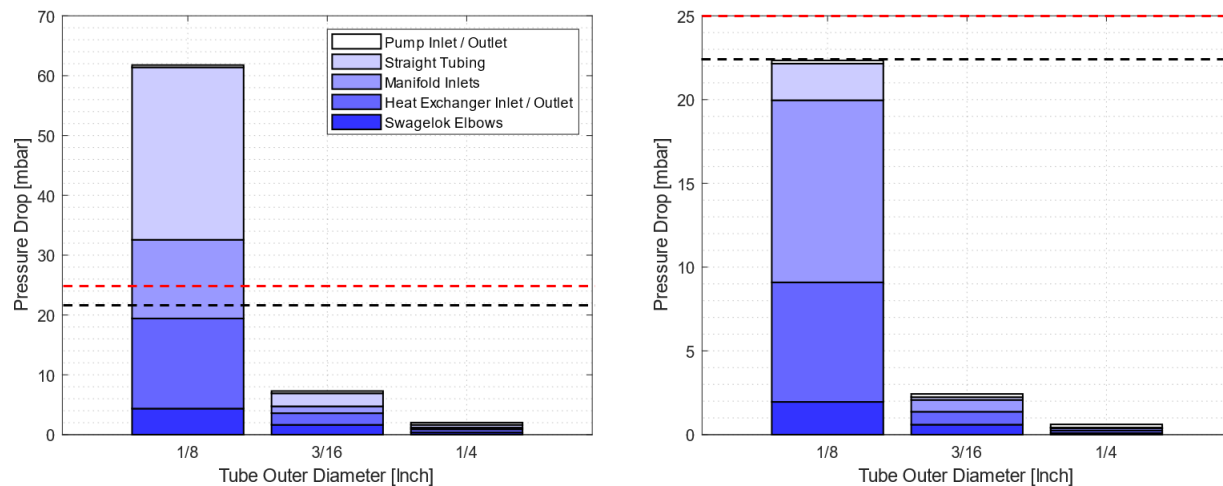


Figure 5.20: Total Pressure Drop of the Tubing at a Fluid Temperature of $-40\text{ }^{\circ}\text{C}$ (left) and $85\text{ }^{\circ}\text{C}$ (right).

To compare the two bar graphs, a black dotted line that represents the maximum value of the pressure drop at $85\text{ }^{\circ}\text{C}$ is drawn in both figures. The red dotted line represents the maximum allowed pressure drop of 25 mbar for which the cooling loop has to be designed. Figure 5.20 shows that the pressure drop significantly increases if the tube size is decreased. Additionally, a decrease in fluid temperature causes an increase in pressure drop due to the increase in fluid viscosity at lower temperatures. An increased viscosity results in more friction of the fluid with the walls of the fluidic components and with itself. The tubing with an outer diameter of 1/8 inch is not suitable for this design, since the pressure drop in Figure 5.20 is shown to exceed the limit of 25 mbar at a temperature of -40 ° . Both the tubing with an outer diameter of 3/16 and 1/4 inch would cause the system to be within specifications for the two most extreme temperatures. Therefore, either one of the two or a combination of these tubing sizes is used in the final design. The tubing with an outer diameter of 1/4 inch is preferred to make sure that the pressure drop stays well below 25 mbar in the coldest possible operating temperature. However, a pressure drop of slightly more than 25 mbar, would not necessarily be a problem, since it would quickly drop below this value when the system starts to heat up.

5.3.2 Mechanical Connection of the Tubing

Tube Fittings As has been stated before, the heat exchangers are connected to the other tubing components using compression elbow fittings. The specific elbow fittings that have been chosen in this design, which can be seen in Figure 5.21, feature a tube compression fit on one side and a socket weld on the other side. The compression fitting is used to connect the fittings to the heat exchanger, since the aluminium alloy of which it is made cannot be welded to the titanium components of the system. To connect the fittings to the pump, the socket weld side of the fitting is used to weld the fitting to the inlet and outlet manifold. Since these manifolds are made of titanium, the fittings are also made of titanium to create a reliable weld.

To reduce costs, the filling interface is made of stainless steel, which means that the fittings that connect the heat exchangers to the filling interface should also be made of stainless steel. All fittings are compatible with a tube size of 1/4 inch.



Figure 5.21: 1/4 Inch Elbow Fitting with Compression Fitting on one side and a Socket Weld on the other side. [28]

A leak-tight compression tube connection works using a female body, a male nut, a front ferrule and a back ferrule. Figure 5.22 shows these four components and the way they are connected to create a connection. It can be seen that the nut connection applies force to both ferrules. The front ferrule is pushed into the small space between the body and tubing to create a gas seal. The back ferrule uses a hinging grip that causes the front ferrule to stay in position during static and dynamic load cases.

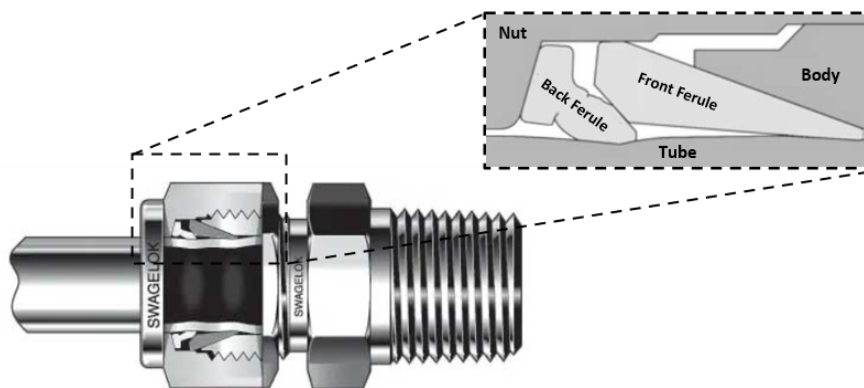


Figure 5.22: Visualisation of the Working Principle of Compression Tube Fittings. [29]

Manifolds To connect the inlet of the pump to the heat source and to connect the outlet of the pump to the heat sink and the accumulator, two manifolds are used. These manifolds are particularly useful for making tight connections that would not be possible using fittings or by bending the tubing. The manifolds consist of a shell body, a lid, multiple hole connection points and a tube connection point. These components are welded together to create the manifold assembly. The design of the inlet and outlet manifold can be seen in Figure 5.23.

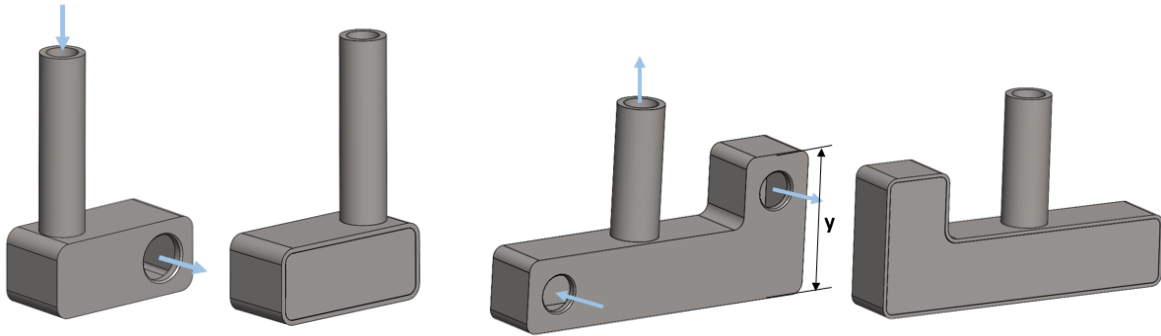


Figure 5.23: Design of the Inlet- (left) and Outlet (right) Manifold.

The manifolds are made from titanium grade 5, which is the same material as the pipes of the pump and accumulator. In this way, the manifolds can be welded to the pump and accumulator to create a leak-tight and rigid connection. However, since the sizing of the accumulator is performed at a later stage in the designing process, the dimension 'y' in Figure 5.23 is yet to be decided. The tube connections on top of the manifolds are connected to the heat exchangers using the previously mentioned elbow fittings.

Final Tubing Design Figure 5.24 shows the tubing components and the placement of the tubing design in the satellite frame.

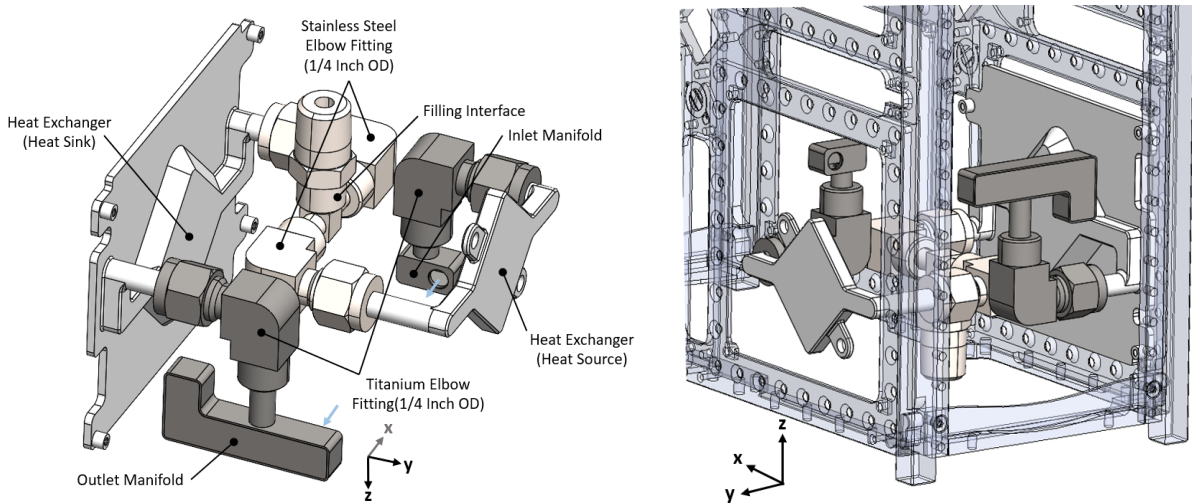


Figure 5.24: Overview of the Tubing Design Components and Placement within the Satellite Frame.

5.4 Accumulator Design

This section includes the resizing of both the accumulator body and the wick inside the accumulator. Additionally, it selects a heater based on the required power that the accumulator needs to function.

5.4.1 Resizing the Accumulator

The fluid in the accumulator serves as a buffer to regulate the pressure in the system. To make sure that the accumulator is sized appropriately without adding too much weight to the system,

several factors like fluid expansion, phase changes, leakages, and safety margins are taken into account.

Fluid Expansion / Contraction The most important factor in sizing the accumulator is the expansion and contraction of the total fluid in the system. An estimation of the total fluid volume in the system is made using the CAD models of the components that have been designed in the previous sections of Chapter 5. This includes the fluid volumes within both heat exchangers, the tubing, the fittings, both manifolds and the pump. Table 5.2 shows the contribution of each of these components to the total fluid volume and the total thermal expansion within the system. To calculate the thermal expansion of the fluid, the equation

$$\Delta V_{\text{exp}} = \beta_f V_{\text{sys}} \Delta T, \quad (5.31)$$

is used, in which β_f refers to the thermal expansion coefficient of Galden HT55 and V_{sys} refers to the total fluid volume in the system except for the fluid in the accumulator itself. The temperature range ' ΔT ' used in this equation is from -40 °C to 85 °C, since this is the temperature range in which the system should operate. In reality, the system is filled up at ambient temperature, which causes the actual temperature range to be approximately half of the selected temperature range. This decision creates a first safety margin for the amount of fluid within the accumulator.

Table 5.2: Overview of the Thermal Expansion of the Fluid within the System.

Component Name	Fluid Volume [mL]	Temperature Range [K]	Thermal Expansion [mL]
Heat Exchangers	4.76	125	0.65
Tubing / Fittings	2.14	125	0.29
Manifolds	3.34	125	0.46
Pump	24.43	125	3.36
Total	34.67	-	4.77

Phase Change When evaporation takes place inside the accumulator, a portion of the fluid is used for this evaporation. An extra amount of fluid is added to the accumulator to account for this phase transition. During the phase transition, the mass stays constant, but the volume increases. To find the amount of fluid that has to be evaporated to compensate for the contraction of the fluid when the system is cooled down from the maximum temperature to the minimum temperature is calculated using the equation

$$\Delta V_{\text{phc}} = \Delta V_{\text{exp}} \frac{\rho_g}{\rho_f}. \quad (5.32)$$

The density of the fluid and gas that are used in this calculation are based on the densities at 90 °C and a pressure of 2.89 bar, which are the accumulator operating temperature and pressure. The extra fluid that has to be added to the accumulator to account for this phase transition is found to be 0.1 mL.

Leak Rate The system is required to operate at a constant pressure for a time span of approximately three years. In this lifetime, the system will experience multiple types of leakage through the welds, fittings and porous components. To prevent the accumulator of running dry due to leakages, an extra volume margin should be added.

Table 5.3 shows an overview of the leakage specs of the heat exchangers, the compression tube fittings and the weld lines. The reason that the heat exchangers contribute significantly to the leakage of the system is because they are 3D printed, which has a negative effect on the leak

tightness of a product. All leak rates are given for helium gas, since helium was used to leak test the components, which is a common practise.

Table 5.3: Overview of the dominant Leak Sources in the System measured using Helium Gas.

Leak Source	Number of Components	Leak Rate [$\frac{\text{mbar L}}{\text{s}}$]	Source
Heat Exchangers	2	$1.0 \cdot 10^{-6}$	NLR Tests
Compression Tube Fittings	4	$<1.0 \cdot 10^{-9}$	Terry,1998 [30]
Welds	10-20	$1.0 \cdot 10^{-9}$	-

The leak rate for Helium gas is different than the leak rate for Galden HT55 due to a difference in fluid viscosity and molecular mass. To account for the contrast in fluid properties, a conversion factor r_{conv} is applied using the equation

$$r_{\text{conv}} = \frac{9.5 \frac{\eta_g}{\eta_f} \Delta p}{p_{\text{sys}} \left(p_{\text{sys}} + 31 \frac{\eta_g}{D_{\text{cap}}} \sqrt{\frac{T}{M_f}} \right)}. \quad (5.33)$$

In this equation, Δp refers to the pressure difference between the inside and the outside of the system [31]. Table 5.4 shows a clear overview of the total leakage in the system over a period of three years, which is used as an addition for the total amount of fluid that should be stored in the accumulator.

Table 5.4: Overview of the total Leakage in the System at an operating Pressure of 2.89 bar over a Period of three Years.

Leak Source	Number of Components	Converted Leak Rate [$\frac{\text{mbar L}}{\text{s}}$]	Total Leak Rate [mL]
Heat Exchangers	2	$1.49 \cdot 10^{-8}$	0.975
Compression Tube Fittings	4	$1.49 \cdot 10^{-11}$	$1.95 \cdot 10^{-3}$
Welds	10-20	$1.49 \cdot 10^{-11}$	$9.76 \cdot 10^{-3}$
Margin	-	-	200 %
Total	-	-	2.96

Total Volume Sizing The total volume of the accumulator is a result of previously mentioned factors like fluid expansion and contraction, the phase transition and the leak rate within the system. Another addition that is made to this volume is an extra 3.0 mL, which acts as a minimum level of accumulator volume when the fluid in the system is at its coldest temperature. To make up for any last minor calculation errors or unforeseen circumstances, an additional 10 % of margin is added to the total volume of the accumulator. A complete overview of the accumulator volume is visualized in Table 5.5.

Table 5.5: Overview of the Total Volume Calculation of the Accumulator.

Volume Section	Required Volume [mL]
Expansion / Contraction	4.77
Phase Change	0.1
Leakages	2.96
Minimum Level	3.0
Subtotal	10.83
Margin	10 %
Total	11.91

5.4.2 Resizing and Selecting the Accumulator Wick

As discussed before, the wick serves the purpose of supplying the heater with a constant flow of fluid to make sure it never runs dry during the evaporation process. It is capable of supplying this flow using capillary forces that pull the fluid through the porous material. In this case, the porous material is selected to be sintered stainless steel. Additionally, the wick serves as a layer that covers the entrance of the accumulator, to ensure that gasses cannot escape the component. Figure 5.25 shows a schematic representation of the accumulator that visualizes the function of the wick.

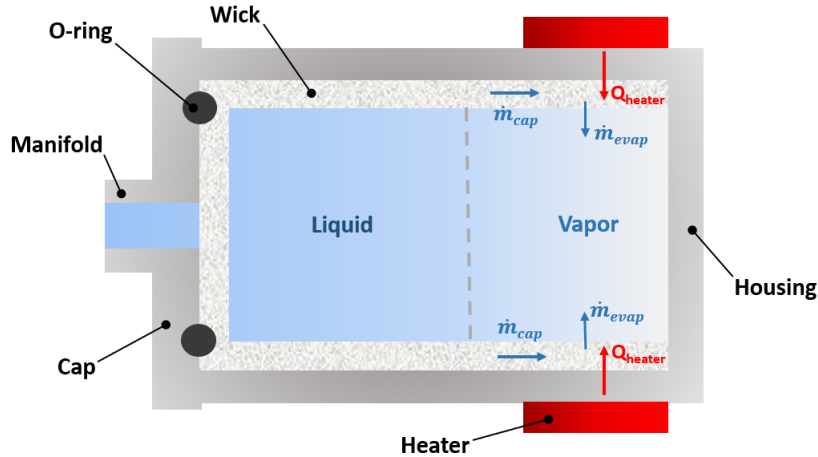


Figure 5.25: Schematic Representation of the Function of the Wick within the Accumulator.

The inside volume of the wick should be equal to the volume that is calculated in Table 5.5. First, a diameter is selected based on the available standard production diameters of the chosen supplier. Using these standard diameters, the required length of the wick is calculated based on the minimum required accumulator volume. Table 5.6 gives an overview of the available wick diameters and the corresponding required length.

Table 5.6: Available Wick Dimensions and their corresponding required Length.

Inner Diameter [mm]	Wall Thickness [mm]	Outer Diameter [mm]	Required Length [mm]
20.0	2.5	25.0	37.91
26.0	3.0	32.0	22.43

The wick inner diameter of 20.0 mm has been selected as the most suitable option since its smaller diameter is optimal for the placement of the accumulator in the system. Moreover, its longer length provides a thermal buffer for the heat to escape the accumulator from the heater directly to the accumulator manifold. The length also acts as a buffer for the gas from reaching the outlet of the accumulator, which makes it even harder for gas to escape if the wick does not function as a barrier properly. The length is rounded up to 38.0 mm, which adds an extra small buffer to the total fluid volume in the accumulator.

To calculate whether the wick supplies the heater with sufficient fluid during the evaporation process, the 'resistance' pressure is calculated using the equation

$$\Delta p_{\text{res}} = \frac{Q_{\text{vap}}^2}{2\rho_f^2 A_w^2 \Delta H_{\text{vap}}^2} + \frac{Q_{\text{vap}} \mu_f L_w}{\rho_f A_w K_{\text{pr}} \Delta H_{\text{vap}}} + \rho_f L_w g, \quad (5.34)$$

which represents the pressure that the capillary forces have to overcome to make flow into the wick possible. In this equation, the first term equates to the dynamic fluid resistance, the second term to the viscous resistance, and the third term to the hydrostatic pressure as a result of gravity. All wick-related calculations are performed using fluid properties at 90 °C, which represents the constant temperature of the accumulator. In Equation (5.34), the porous permeability is represented by K_{pr} , which is a function of the radius of the pores within the material. The capillary pressure that is generated by the wick is calculated using the relation

$$\Delta p_{\text{cap}} = \frac{2\sigma_f \cos(\theta)}{r_{\text{pr}}}, \quad (5.35)$$

in which σ_f represents the surface tension of the fluid and θ represents the wetting angle. In this case, a perfect wetting is assumed, which indicates that $\cos(\theta)$ is equal to 1. If the capillary pressure is found to be higher than the resistance pressure, the fluid will start to flow through the wick towards the heater side of the accumulator. Using the Darcy's Law, which is formulated as

$$\dot{m}_{\text{max}} = A_w \rho_f K_{\text{pr}} \frac{(\Delta p_{\text{cap}} - \Delta p_{\text{res}})}{\eta_f L_w}, \quad (5.36)$$

the maximum mass flow due to capillary forces can be calculated. Figure A.3 in Appendix A shows the available wick material properties, which vary in pore size, permeability, porosity and strength. Figure 5.26 shows the permeability of the material for different pore sizes and the maximum mass flow that can be reached with these various materials based on Equations 5.34 and 5.35.

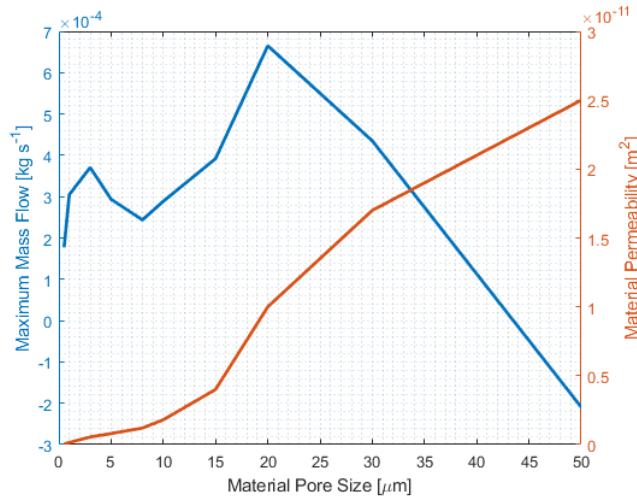


Figure 5.26: Maximum Mass Flow and Material Permeability vs. Material Pore Size.

The wick that has been selected has a pore size of $5\mu\text{m}$ and a permeability of $0.8 \cdot 10^{-12} \text{ m}^2$. This wick has been selected to make sure that the maximum mass flow would always be enough, even if the material pore size would be slightly larger due to possible manufacturing tolerances. Additionally, a wick with a smaller pore size is found to be stronger, which adds extra structural strength to the design. The resulting mass flow that this wick can deliver to the heater is $1.96 \cdot 10^{-3} \frac{\text{kg}}{\text{s}}$, which is significantly higher than the evaporation rate during cooldown of $4.15 \cdot 10^{-8} \frac{\text{kg}}{\text{s}}$. This implies that the wick is certainly capable of supplying the heater with sufficient fluid during the evaporation process.

5.4.3 Selecting the Accumulator Heater

To be able to evaporate fluid and keep the temperature of the accumulator constant, a heater is required. This heater is located on the opposite side of the accumulator inlet to prevent any vapour from escaping the accumulator. The power that is required by the heater depends on several different factors like required evaporation energy, heat losses, required energy to maintain a constant temperature when cold fluid enters the accumulator and gained energy during condensation.

Maximum Temperature Change During the start-up and the cooldown process of the system, the largest temperature fluctuations, defined as a temperature change per second, take place. These temperature changes cause the fluid to expand or contract, which is when the function of the accumulator becomes most important. In the worst-case scenario during start-up, all heat that is put into the system using the heat source will flow directly into the fluid without entering any other bodies of thermal mass like the heat exchangers, tubing, fittings, manifolds or the pump. This is considered the worst-case scenario since it will cause the quickest fluid temperature change. Although this scenario will not occur in real life, it does suffice in estimating the maximum power that is required for the accumulator heater. To calculate the maximum temperature change at the system start-up, the equation

$$\frac{dT}{dt} = \frac{\dot{Q}_{\text{src}} + \dot{Q}_{\text{pmp}}}{m_f c_p}, \quad (5.37)$$

is used. The equation sums the maximum input power of the heat source with the power produced by the pump, which are the two heat sources that directly contribute to heating the fluid in the cooling loop. The maximum allowable input power of the heat source in the worst-case scenario is around 3.0 W, which can be found in Section 5.1. The heat produced by the pump is approximately 0.41 W, which is analysed in Section 4.1. The total power is then divided by the thermal mass of the fluid to find the temperature change. Using Equation 5.37, the temperature change per second during the start-up process is found to be $4.54 \cdot 10^{-2} \frac{\text{°C}}{\text{s}}$.

Thermal Losses Since the accumulator is the hottest component in the system, it will always lose some of its thermal energy. In the vacuum of space, convection can be neglected. Radiation will also be neglected since the accumulator is wrapped in MLI (Multi-layer Insulation). This insulation will make sure that the radiation of the accumulator is not able to travel away from the component, thus keeping the thermal energy for itself. The only two manners through which the accumulator will lose heat are by conduction through the tube that connects the accumulator to the manifold and by conduction through its support structure. Both of these thermal leaks are analysed to gain a better understanding of the total heat loss of the accumulator.

Figure 5.27 shows schematic representations of the accumulator inlet tube and support structure that are used to calculate the amount of heat that the accumulator loses to the system.

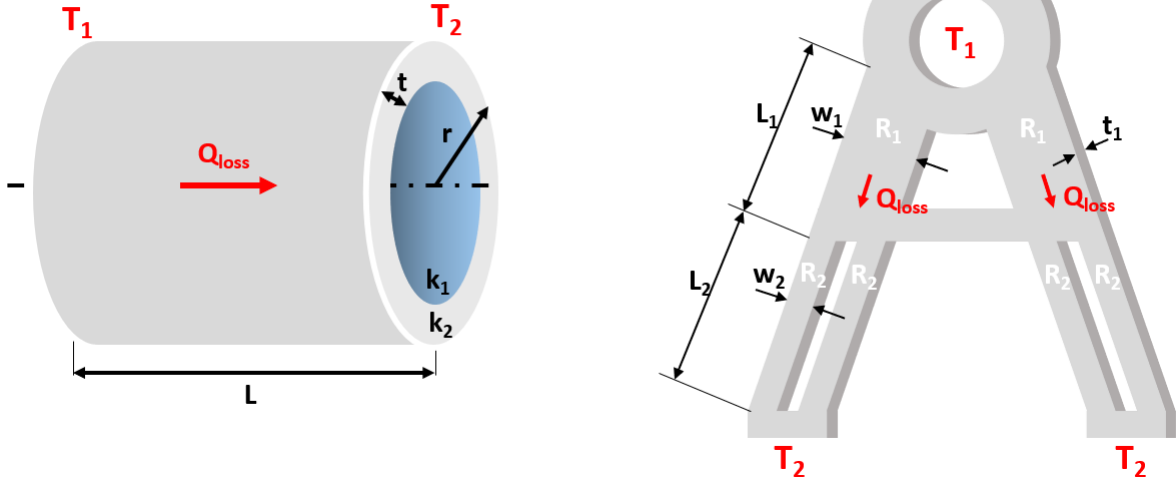


Figure 5.27: Schematic Representation of the Thermal Losses of the Accumulator through its inlet tube (left) and Support Structure (right).

In these figures, T_1 represents the operation temperature of the accumulator, while T_2 represents the temperature of the rest of the system. For this estimation it is assumed that the temperature is uniform throughout the entire system. To calculate the total amount of heat that is lost from the accumulator through conduction, the equation

$$\dot{Q}_l = \dot{Q}_{tb} + \dot{Q}_{sup} = \frac{T_1 - T_2}{R_{tb}} + \frac{T_1 - T_2}{R_{sup}} \quad (5.38)$$

is used. The thermal resistance R_{tb} can be calculated by adding the thermal resistances of the fluid and the tube wall of the accumulator using a parallel system, as stated in the equation

$$\frac{1}{R_{tb}} = \frac{1}{R_1} + \frac{1}{R_2} = \frac{k_1 A_1}{L} + \frac{k_2 A_2}{L}. \quad (5.39)$$

In this equation, R_1 represents the thermal resistance of the fluid in the inlet tube, while R_2 represents the thermal resistance of the tube wall.

The thermal resistance of the support structure R_{sup} is estimated using a simplified version of the actual structure, which is visualized in Figure 5.27. The simplified structure consists of two sections of which the first section consists of two legs and the second section consists of four legs. to calculate the total thermal resistance of the structure, the equation

$$R_{sup} = \frac{R_1}{2} + \frac{R_2}{4} = \frac{L_1}{2k w_1 t_1} + \frac{L_2}{4k w_2 t_1} \quad (5.40)$$

is used. In this equation, R_1 represents the thermal resistance of a single leg in the first section, while R_2 represents the thermal resistance of a single leg in the second section of the support structure.

By combining Equations (5.38), (5.39), and (5.40), the total thermal loss of the accumulator can be calculated for the full range of system temperatures. The maximum temperature loss will occur during start-up and the minimum temperature loss will occur when the temperature is operating at its equilibrium temperature. Figure 5.28 shows the total thermal losses of the accumulator for different values of the system temperature T_2 .

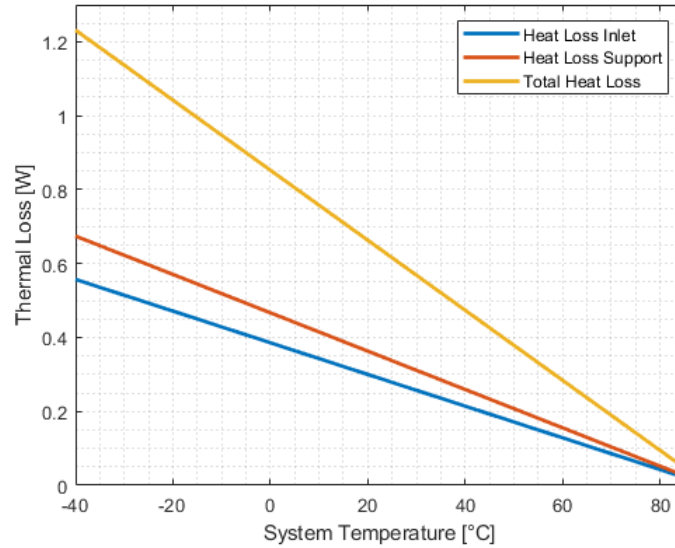


Figure 5.28: Total Heat Loss of the Accumulator for the full Range of System Temperatures.

In a worst-case scenario, the system start-up temperature is $-40\text{ }^{\circ}\text{C}$. In this situation, the temperature difference between the system and the accumulator is at its highest, which causes the thermal loss to be at a maximum of around 1.23 W for the final support structure in Figure 5.29. Compared to the estimated power range of the heat source, this is a significant amount of heat loss. However, when the system heats up to reach its equilibrium temperature, the heat loss of the accumulator decreases substantially. Additionally, the connection of the support structure of the accumulator could be further isolated using for instance thermal washers, which is taken into account during the accumulator heater selection and during the final thermal analysis in Section 6.4.

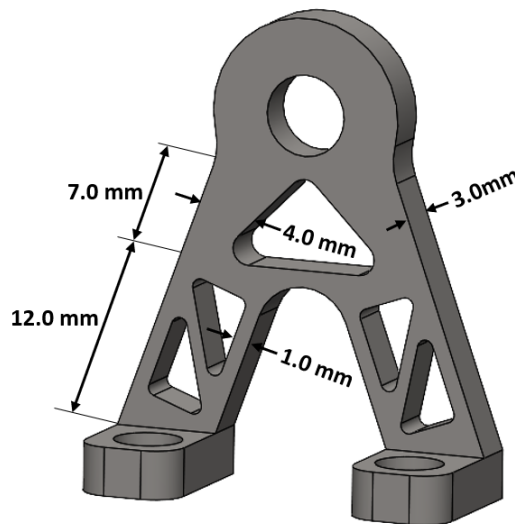


Figure 5.29: Final Design of the Accumulator Support Structure with approximate Dimensions used in the Simplified Thermal Analysis.

Accumulator Heater Power To decide the power of the heater, an energy balance is made for the system during start-up and during cooling down from its equilibrium temperature. During start-up, the fluid in the system heats up and thus starts expanding. This will cause some of the fluid that was first located within the system to flow into the accumulator at a temperature of $-40\text{ }^{\circ}\text{C}$. This flow is heated from this starting temperature up to the operating temperature of

the accumulator. The inflow of cold fluid into the accumulator and the energy that is required to heat this fluid to the accumulator temperature is calculated using the equation

$$\dot{Q}_{ht} = \dot{m}_{in}c_p\Delta T_{acc} = \frac{dT}{dt}\rho_f V_{sys}\beta_f c_p\Delta T_{acc} = \frac{dV}{dt}\rho_f c_p\Delta T_{acc}. \quad (5.41)$$

The equation calculates the mass flow that flows into the accumulator at start-up by multiplying the maximum temperature change at start-up by the total system fluid volume, the coefficient of thermal expansion and the fluid density. This mass flow is then multiplied by the amount of energy required to heat the fluid from $-40\text{ }^\circ\text{C}$ to $90\text{ }^\circ\text{C}$, represented by ΔT_{acc} times the specific heat of the fluid. Using this method, the amount of power that is required to heat the mass flow of fluid Galden HT55 at startup is calculated to be 0.488 W .

Due to the expansion of the fluid, the gas in the accumulator will start to condense to keep the pressure in the system constant. The energy that is produced within the accumulator due to the condensing vapour during the start-up process is calculated using the relation

$$\dot{Q}_{cond} = \dot{m}_{cond}\Delta H_{vap} = \frac{dV}{dt}\rho_g\Delta H_{vap}, \quad (5.42)$$

and is found to be $7.1 \cdot 10^{-3}\text{ W}$. The final step in calculating the required heater power during start-up is making an energy balance.

During start-up, the heater should be able to keep the accumulator at a constant temperature by overcoming the heat losses and heating the incoming fluid to $90\text{ }^\circ\text{C}$. The condensation process will produce heat, which can be subtracted from the heat that the heater needs to produce during start-up. Taking all energy flows into consideration, the equation

$$\dot{Q}_{st} = \dot{Q}_l + \dot{Q}_{ht} - \dot{Q}_{cond} \quad (5.43)$$

is used to calculate the required heater power of the accumulator heater at start-up. Using this equation, the required power in the worst-case scenario is calculated to be 1.712 W .

When cooling the system down from its equilibrium temperature, the fluid in the system will start to contract. To keep the pressure constant, the accumulator will start to evaporate fluid into gas. Equation (5.42) can be used again to calculate the amount of heat required to evaporate the fluid. The reason that the same equation can be used is because the temperature change over time is the same during cooldown, which results in the same volume change and thus the same evaporation energy. Due to the contraction of the fluid, some of the hot fluid within the accumulator is released into the system. This extra heat will not cause the system's temperature to increase, since the heat source is turned off at this point. The required accumulator heater power during cooldown is calculated using the equation

$$\dot{Q}_{stp} = \dot{Q}_l + \dot{Q}_{vap}. \quad (5.44)$$

Since the thermal losses of the accumulator are generally much higher than the energy that is required for evaporation, it can be assumed that the required power during cooldown is lower than during start-up. Therefore, the selection of the heater is based on the required power during start-up.

Final Accumulator Heater Selection The type of heater that has been selected for the accumulator is a flexible heater manufactured by Zoppas. The main advantages of this heater within this project are that they are lightweight, flexible, easy to install, proven to be space compatible, and they are readily available at Demcon. The operating temperatures of this heater are between -65 and $150\text{ }^\circ\text{C}$, which is within the temperature range of the experiment.

More specifications of this heater can be found in Table C.1 in Appendix A. Figure 5.30 shows the build-up of these types of heaters and the dimension definitions. The heater should be able to deliver close to the maximum required power of 1.712 W.

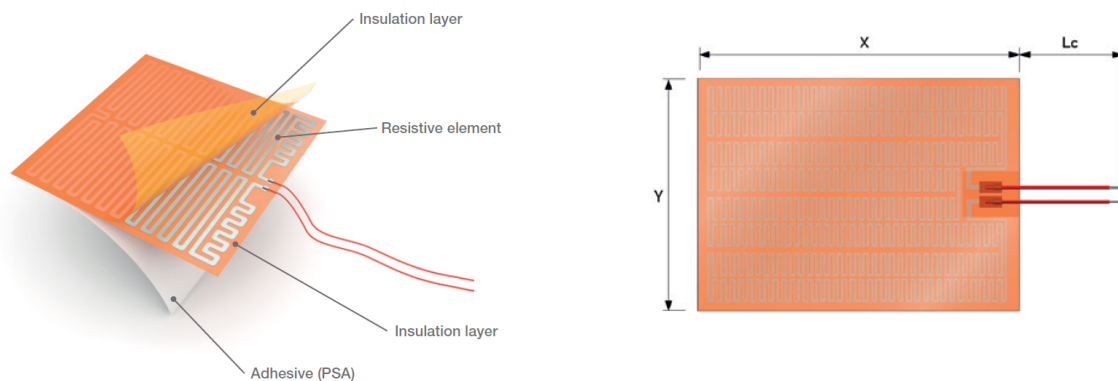


Figure 5.30: Thermal Loss of the Accumulator to the System over the Range of System Temperatures. [32]

Table C.2 in Appendix A shows the different available sizes of these types of heaters along with their corresponding electronic resistance and power. The heater should be placed as far away from the accumulator inlet as possible to prevent gas from escaping. It shall be wrapped around the housing of which the perimeter is equal to approximately 85.5 mm. To avoid the heater from overlapping itself during installation, the 'x' dimension of the heater should be less than the perimeter. The longest possible heater that is available is 75 mm in length and is obtainable in three different width sizes. A smaller width would be the most favourable since this would mean that the gas is being formed further away from the inlet of the accumulator, which reduces the risk of gas escaping the accumulator.

The heater powers are given at 28 V while the satellite avionic will deliver only 12 V. The power of the heaters is calculated using the relation

$$P = \frac{E^2}{R_{el}}, \quad (5.45)$$

in which the power is shown to increase with the square of the voltage. In Table 5.7, a power comparison is made between the different available flexible Zoppas heaters with a length of 75 mm to select the most suitable size.

Table 5.7: Overview of the Power of different Zoppas Flexible Heaters with a Length of 75 mm.

Width [mm]	Resistance [Ω]	Power @28V [W]	Power @12V [W]
12.5	247,2	3.2	0.58
25	110,2	7.1	1.3
50	52,3	15	2.75

Based on this information, it becomes clear that the smallest heater in width is not able to deliver the maximum required power by a factor of three. The heater with a width of 25 mm is also not able to deliver the required power in the worst-case scenario but does get close to reaching it. Lastly, the 50 mm heater is able to deliver enough power with a margin of 166.2%. The most favourable option is selected to be the heater with dimensions of 75 by 25 mm. The main reasons for selecting this heater are because it is smaller in width, which means it is further away from the accumulator inlet and because the larger heater has too much power, which might cause the accumulator to heat up too fast. The 75 by 25 mm heater is not able to deliver the

required power in the worst-case scenario, which is not considered to be a problem since the system will most likely never reach a temperature as low as -40°C and the accumulator will be better isolated than considered in the previous calculations. Additionally, if the system does reach a temperature of -40°C , the heating power of the accumulator, pump, drive electronics and heat source combined will cause the system to quickly rise in temperature at which point the accumulator loses less heat to conduction and is able to deliver enough power again. The worst that could happen due to the accumulator not being able to deliver enough power is that the temperature of the accumulator will slightly drop.

5.4.4 System Filling Method

During the filling process, which is performed at ambient temperature and pressure, the system is fully filled with fluid. If the system were closed at that moment, the incompressible fluid would have no space to expand when the system heats up, which would rapidly increase the system pressure to the point where it would exceed the burst pressure of certain components. To prevent this from happening, some vapour should already be present in the accumulator before closing the system. This way, when the fluid starts to expand, the gas that is already present in the accumulator can compress. Since the gas is compressible, the system pressure will only slightly increase, which will not harm the system. When the system cools down the gas will condense until a vapour pressure balance is found. This will cause the pressure in the system to go slightly below atmospheric pressure, which will not harm the components in the system.

To make sure that gas is present in the system before closing it, the accumulator heater will be turned on after the filling sequence in Figure 4.18 has been finished. This will cause the fluid to heat up and start the evaporation process. When vapour starts to form, the system's volume will expand and push some fluid out. The system will be placed on a scale to measure the amount of fluid that is pushed out of the system. When half the volume of the accumulator is filled with gas, a cap will be welded onto the opening of the system to close the system off. This process will be performed at ambient temperature. The weight reduction that has to be measured to fill half of the accumulator with gas is calculated using the equation

$$\Delta m = \frac{\rho_f V_{\text{acc}}}{2} + \rho_f V_{\text{acc}} \beta_f (T_{\text{vap}} - T_{\text{amb}}). \quad (5.46)$$

The first term in this equation represents half of the weight of the fluid within the accumulator, while the second term represents the thermal expansion of the fluid in the accumulator when it is heated from ambient temperature to its boiling point. Using this equation, the change of mass that has to be measured before closing the system is calculated to be 10.65 g.

5.5 Heat Source Selection

The heat source acts as a dummy representation for the heat-generating electronics that would be present in a real space mission. By combining the equilibrium temperature information found in Chapter 5.1 and the power budget of Chapter 6, the heater power is selected to be between 2.0 and 3.0 W. In this section, several options for a heater type have been researched after which the most suitable heater has been selected. Additionally, a mechanical connection has been designed. This mechanical connection is directly related to the choice of heater since not all heaters have the same connection method.

5.5.1 Heat Source Pre-Selection

After thorough market research, seven heaters from five different suppliers have been selected that could potentially be used as a heat source during the in-orbit demonstration. Table 5.8 provides information about this first selection of heaters. It contains information about the

supplier, heater type, dimensions, power, connection method and temperature range of these heaters. From these heaters, a further selection is made to decide which of them is used in the final design.

Table 5.8: First Selection of possible Heat Sources.

Supplier	Article Number	Heater Type	Dimensions (LxBxH) [mm]	Power @12V [W]	Connection Method	Temperature Range [°C]
DBK Enclosures [33]	HP04-1/04-24	Enclosure Heater	40x35x8.5	2.5	Screw Mounting	-
Omega Engineering [34]	KHLVA-101/(*)-P	Flexible Heater	25.4x25.4x0.25	1.84	Adhesive	-40 to 149
Omega Engineering [35]	HPG-3375	Surface Spot Heater	30x28x7.1	2.0	Screw Mounting	-40 to 70
RS Pro [36]	798-3741	Flexible Heater	25x50x0.2	1.25	Adhesive	-60 to 200
RS Pro [36]	798-3772	Flexible Heater	50x0.2	2.0	Adhesive	-60 to 200
Minco [37]	HAP6944-1	Flexible Heater	12.7x12.7x0.3	3.80	Adhesive	-73 to 177
Minco [37]	HAP6947-1	Flexible Heater	25.4x25.4x0.3	3.80	Adhesive	-73 to 177
Zoppas	SC037037F	Flexible Heater	37.5x37.5x0.2	0.96	Adhesive	-65 to 150

5.5.2 Heat Source Final Selection

The final heat source selection is performed using a decision matrix. This matrix takes several important heater specifications into account to select the best possible option. The criteria used to rank the different options are weight, size, heating power, mountability, temperature range and outgassing. The score on each of these criteria is rated from 1 to 5 and multiplied by the weight factor, which represents the relevancy of the criterion to the design. Finally, the scores of each criterion are summed up to calculate the total score of each option. The heater with the highest score is selected to be added to the in-orbit demonstration. The HS numbers in the matrix correspond to the row in Table 5.8 that the heat source is in.

Heating power is considered to be the most important criterion in the selection since the system is not able to operate according to plan when the available power is lower than 2.0 W. In second place are the temperature range and outgassing, since these are related to the material of the heater and are of high importance for the heater to function in space for over three years and many operating cycles. Size is considered to be less important than the first three criteria because the design of the heat exchanger could be slightly altered to create space for a slightly larger heater. However, a heater that is too big, could block the electrical connections or the inlet and outlet of the heat exchangers, which is why it is still considered more important than weight and connection method. These two criteria are considered the least important because several adjustments can easily be made to compensate for them. For weight, this refers to reducing the weight of other components and for the connection method, it refers to slightly altering the heat exchanger to feature new threaded holes or new surfaces to attach the heater to. The outgassing criterion is rated a one if the method is proven to show too much outgassing, a three if the method is known to be an outgassing risk and a five if the method is proven to have a CVCM lower than 0.1% and a TM lower than 1%.

Table 5.9: Decision Matrix for the Selection of a Heat Source.

Criteria	Weight Factor	HS 1	HS 2	HS 3	HS 4	HS 5	HS 6	HS 7	HS 8
<i>Weight</i>	0.1	3	5	3	5	5	5	5	5
<i>Size</i>	0.15	2	5	3	3	2	5	5	4
<i>Heating Power</i>	0.25	4	3	5	2	5	4	4	1
<i>Connection Method</i>	0.1	3	4	3	4	4	5	5	5
<i>Temperature Range</i>	0.2	1	4	2	5	5	5	5	5
<i>Outgassing</i>	0.2	1	5	1	5	5	5	5	5
Total	100%	2.3	4.2	3.3	3.85	4.45	4.75	4.75	3.85

After rating all heaters based on their specification sheets, the most suitable heaters are found to be the Minco HAP6944-1 and HAP6947-1 heaters. These heaters are capable of delivering 3.0 W of power with a margin of approximately 26.67%, which allows the system to be heated up more quickly if necessary. When the system then reaches its designated temperature, the heaters can be turned on and off to reach an average power of between 2.0 and 3.0 W. The heaters are made of polyimide, which is known to have a very low outgassing rate. In the specifications of the heaters, the outgassing is stated to be 0.36% TML and 0.01% CVCM. This is much lower than the maximum outgassing requirement specified by ESA. The heaters are able to survive the full operating temperature range of -40 °C to 85 °C. Moreover, the size of these heaters certainly fits on the heat exchanger and they weigh only 1 to 3 g. Lastly, the heaters feature an adhesive, which makes them convenient to mount to other surfaces.

To choose between the last two heaters one of the data sheets of Minco is utilized. This data sheet features a graph, which is also shown in Figure 5.31, of the maximum power density that the heater is allowed to dissipate at different heater temperatures. If this power density is surpassed, the data sheet states that the heater might overheat, which could lead to premature failure. The graph features three lines for different mounting techniques. For the selected heaters, #12 PSA is used as the mounting adhesive.

By dividing the generated heat power by the effective area of the HAP6944-1 and HAP6947-1 heaters, their power densities are calculated to be 25 and $4.59 \frac{\text{W}}{\text{inch}^2}$ respectively. At the maximum system temperature of 85 °C, the maximum allowed power density of the heater using the #12 PSA adhesive is found to be approximately $27 \frac{\text{W}}{\text{inch}^2}$. The power density of the HAP6944-1 almost reaches this maximum allowed power density. Due to this finding, it is considered safer to select the HAP6947-1 heater as the most suitable option to prevent the heater from overheating and possibly failing.

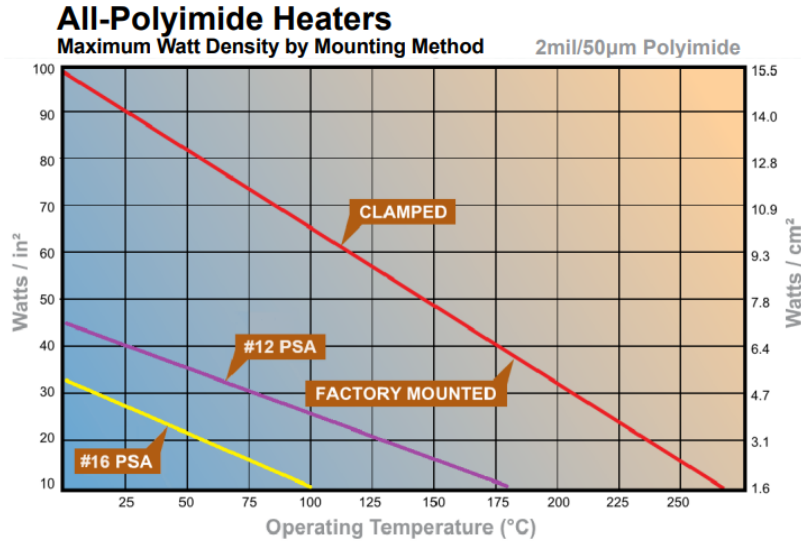


Figure 5.31: Maximum Power Density vs. Temperature for Minco All-Polyimide Heaters. [38]

5.5.3 Mechanical Connection of the Heat Source

To connect the heater to the heat exchanger, its adhesive layer is utilized. The adhesive is described by Minco as # 12 PSA, which is an abbreviation for a pressure-sensitive adhesive. This specific adhesive is silicone-based and has thermosetting properties when properly cured. To make sure that a good connection is made, the surface first has to be prepared to be clean, dry and dust-free. After preparing the surface, the following mounting steps have been described in a mounting document of Minco [39]:

- Remove the protective release backing from the adhesive side of the heater. A quick sharp continuous pull of the release backing at an angle of at least 120° gives the best results. Do not stop until the backing is completely removed.
- Carefully position and apply the heater to the desired surface, making certain that firm, even pressure is applied to the entire bonding area while trying to avoid air entrapment from occurring. To achieve maximum bond strength, allow 72 hours of wet-out time.
- Press the installed heater into close contact with the heat sink surface at ambient temperature using a rubber roller or equivalent. Apply pressure starting at the centre of the heater and roll to each outer edge to remove any entrapped air.
- Place the installed heater with the part in an oven set at approximately 150°C for 10 to 15 minutes to thermally set and cure the adhesive film.
- Allow 72 hours of wet-out time.
- If the mounted heater is to be operated in a vacuum environment, it is recommended that the heating indicated in step 4 be performed in a vacuum chamber to ensure the removal of all entrapped air. The temperature should be set at least as high as the operating temperature, but not exceed 175 °C.

5.6 Housing Design

The final component in the design sequence of the in-orbit demonstration is the housing. The main functions of this component are to connect the other components to the frame and to bring rigidity to the design, which is important to survive vibrational loads during the launch

of the satellite. Another important function of the housing plate is to thermally isolate certain components from the satellite frame to prevent a significant amount of heat from escaping the cooling loop by conductance into the frame.

5.6.1 Mechanical Connections of the Housing

Connections Overview To mechanically connect the housing and the system components to the frame, several different bolted connections are utilized. Figure 5.32 shows a schematic overview of the location of the mechanical connections along with their metric connection sizes.

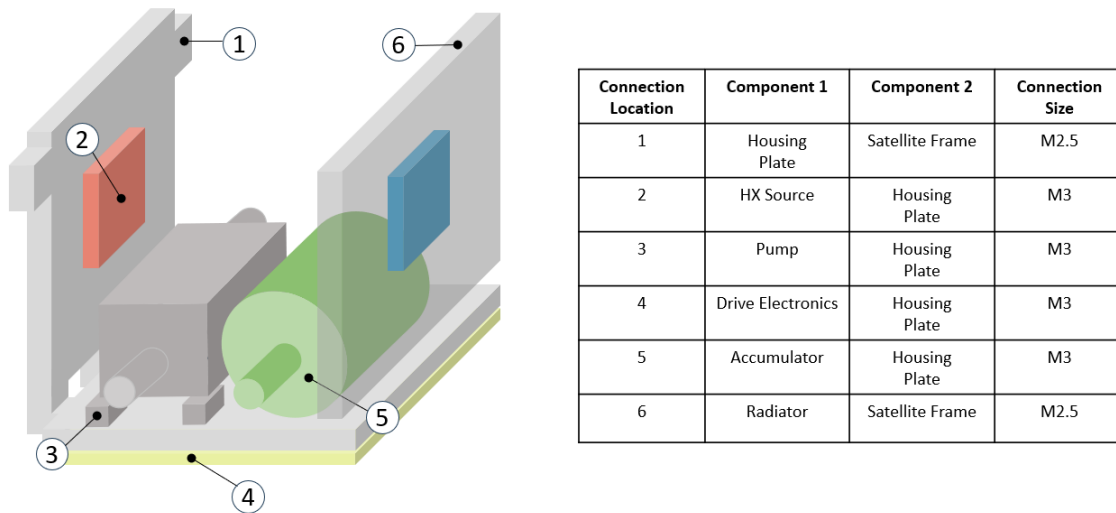


Figure 5.32: Schematic Overview of the Bolted Connections within the System.

From these six different connection locations, there are four main connection types. The first two types of connections are the connections of the housing plate and the radiator plate to the satellite frame, which are performed using a countersunk screw. This type of connection is a result of the countersunk holes on the outside of the frame. The difference between these two connections is that the connection of the housing plate to the satellite frame is made using a self-clinching nut, while the connection of the radiator plate to the frame is made using internal thread within the radiator plate. The third and most occurring connection type is a simple bolt and nut connection that is used to connect the pump, accumulator and heat exchanger at the source to the housing plate. The last connection type is the bolt and nut connection of the drive electronics to the housing plate, where a spacer is placed in between these components to leave space for the electronics components on the PCB.

Thermal Isolation To make sure that most energy that is put into the system is dissipated through radiation at the radiator plate instead of through conduction into the frame, all connections apart from connection four should be thermally isolated to a certain extent. Three ways to do this are to choose bolts that have a low thermal conductivity, use thermal washers/bushings or modify the geometry to have a higher thermal resistance. One of the modifications that can be made to a geometry to gain thermal resistance is to increase the distance between the two conductive surfaces by using thicker washers or a longer supporting structure. Another method could be to decrease the area through which the conductive heat transfer takes place.

Taking all these options into consideration, the bolt and nut material that has been selected to make these connections is selected to be titanium grade 2. This material has many advantages over other fastener materials since it is strong, lightweight, corrosion resistant and has a relatively low thermal conductivity. For the thermal washers and bushings, PEEK is selected to be

the most suitable material, since it has a low thermal conductivity, is a relatively strong thermoplastic polymer and has a low outgassing rate. Additionally, PEEK is proven to perform well in previous space applications, which causes the material selection to be less of a risk [40] [41]. Figure 5.33 shows the dimension parameters of the bushings and the washers, while Table 5.10 shows the actual dimensions for the bushings and washers in each connection location.

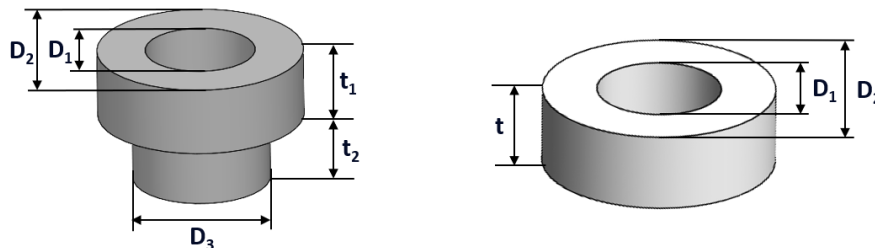


Figure 5.33: Dimension Parameters of the thermally isolating Bushings (left) and Washers (right).

Table 5.10: Thermally isolating Bushing and Washer Dimensions at the several connection locations.

Connection Location	Bushing Dimensions [mm]					Washer Dimensions [mm]		
	D ₁	D ₂	D ₃	t ₁	t ₂	D ₁	D ₂	t
1	-	-	-	-	-	2.6	5.4	1.0
2	3.2	6.0	4.0	2.0	2.0	3.2	6.0	3.0
3	3.2	6.0	4.0	2.0	2.0	3.2	6.0	2.0
5	3.2	6.0	4.0	2.0	2.0	3.2	6.0	2.0
6	-	-	-	-	-	2.6	5.4	3.0

Bolt Calculations Figure 5.34 shows the different types of bolted connection that are present in the system with corresponding numbers to the connection locations in Figure 4.21. Table 5.11 shows an overview of the dimensions and materials of the bolted connections. To make sure that the bolted connections do not loosen during vibrational loads, a glue has to be applied at the bolt and nut thread.

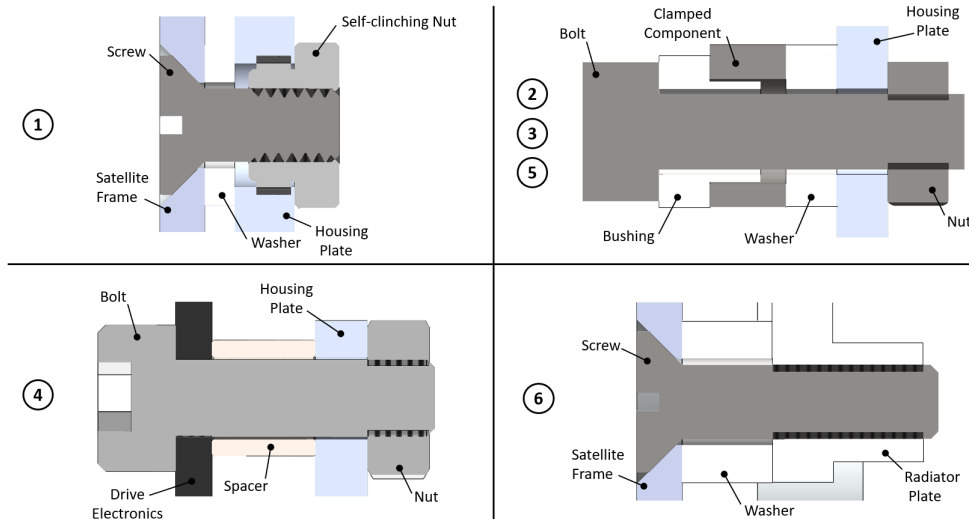


Figure 5.34: Detailed Cross-sectional View of the Four Types of Mechanical Connections of the Housing Plate.

Table 5.11: Bolt Dimensions and Materials for each of the Bolted Connection Locations.

Location	Number of Connections	Dimensions [mm]	Material
1	3	M2.5x8	Titanium Grade 2 (3.7035)
2	2	M3x13	Titanium Grade 2 (3.7035)
3	2	M3x13	Titanium Grade 2 (3.7035)
4	4	M3x12	Stainless Steel A4-70
5	2	M3x12	Titanium Grade 2 (3.7035)
6	4	M2.5x10	Titanium Grade 2 (3.7035)

To determine what torque should be applied to each bolt to create sufficient clamping force, a bolt calculation tool can be used. The most important input values of the bolt calculation tool that are based on the material and dimensions of the connection are the bolt size, bolt material, clamped part material, threaded part material, clamped part size and screw clearance depth. Other important values are the tightening torque, external axial load and the required pretension. Figure 5.35 shows a schematic image of the bolted connection along with its relevant dimensions.

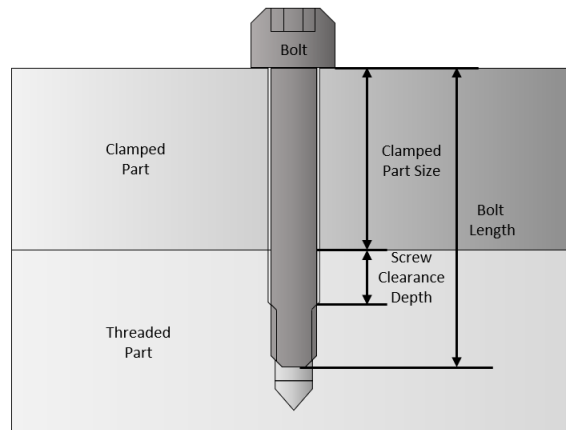


Figure 5.35: Schematic Overview of relevant Bolt Connection Tool Dimensions.

In the specific connection cases in Figure 5.34, connections one and six would not be able to be calculated using a bolt connection tool, because of the countersunk screws. These types of connections make it nearly impossible to determine the exact contact area of the screw with the countersunk hole.

The PEEK washers and bushings create another hurdle in these types of calculations since they are less stiff when compared to the other materials that play a role in the several bolted connections. Additionally, PEEK is prone to creep when a constant force is applied to the material. The amount of creep that takes place is dependent on the stresses and temperatures in the material.

Due to time limitations, the bolt calculations are not performed and require further investigation.

5.6.2 Multi-layer Insulation

To shield the entire system from radiation and to prevent radiation from leaving the system, the entire design apart from the radiator surface is covered in MLI. Figure 5.36 gives a schematic overview of the layout of MLI.

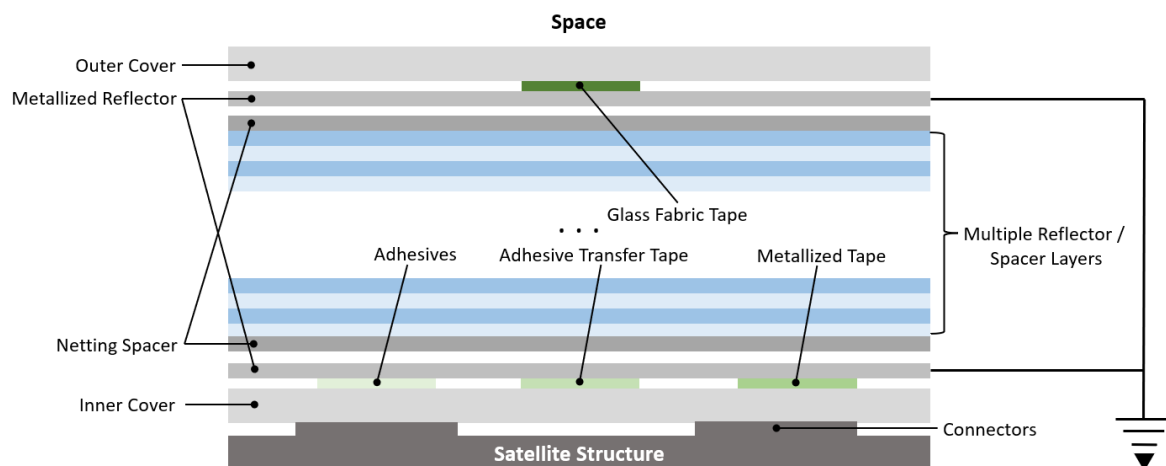


Figure 5.36: Schematic Overview of the Layout of MLI. [42]

The typical build-up of MLI consists of multiple reflector layers that are separated by spacer layers. The reflector layers are thin polymer films with vapour-deposited metal on both sides. These metal layers have a low absorptivity and emissivity to block most radiation from passing

through the material. Between the reflector layers are spacer layers that are made of a low-conducting material to reduce the conductive heat transfer through the MLI sheet. To protect these layers, most MLI sheets contain another netting spacer, a metallised reflector and a cover on both sides. The metallised reflector layers are grounded to prevent electric charge from building up inside the MLI material. To connect the outer cover to the metallised reflector, glass fabric tape could be used. The inner cover could be connected to the metallised reflector using three different methods adhesives, adhesive transfer tape, or metallised tape. All layers are connected using threads. The threads that are used on the space side of the MLI are different from the threads used on the satellite structure side based on the resistance of the threads to atomic oxygen erosion and UV degradation. Finally, the MLI is connected to the satellite structure using several connectors. To prevent air from being entrapped inside the MLI, which might cause ballooning, small perforations could be added to the sheet. [42]

In research by NASA, several possibilities option for each layer are listed. In these lists, the most relevant material properties are stated to gain an overview of for example the strength, temperature range and optical properties of each possible option. [42]

5.7 Sensor Locations

To regulate the system and prevent it from overheating, information on the temperature at several locations within the system is of importance. As has been stated in the requirements, a temperature sensor is placed at the heat sink, the heat source and the accumulator. Furthermore, a temperature sensor is placed on the satellite frame to gain more insight into the heat that the system is losing through conduction into the frame. This information would also be helpful to compare the results of the in-orbit demonstration to the thermal analysis in Chapter 6. The type of sensor that is used to record the temperature and to communicate its readings to the satellite avionics is regarded as out of scope for this research, as it is highly dependent on the software and electrical hardware design, which is also out of scope.

5.8 Final Design Overview

By combining all design choices that have been made throughout Chapters 4 and 5, a final design layout is created. This final design is visualised in Figures 5.37 and 5.38 and serves as the starting point of Chapter 6, in which the design is fluidically, thermally and mechanically analysed. In this figure, all structural elements apart from bolts, nuts, spacers and bushings have a number behind their label that refers to a material number in Table A.1 in Appendix A. The materials of the fasteners are listed in Table 5.11.

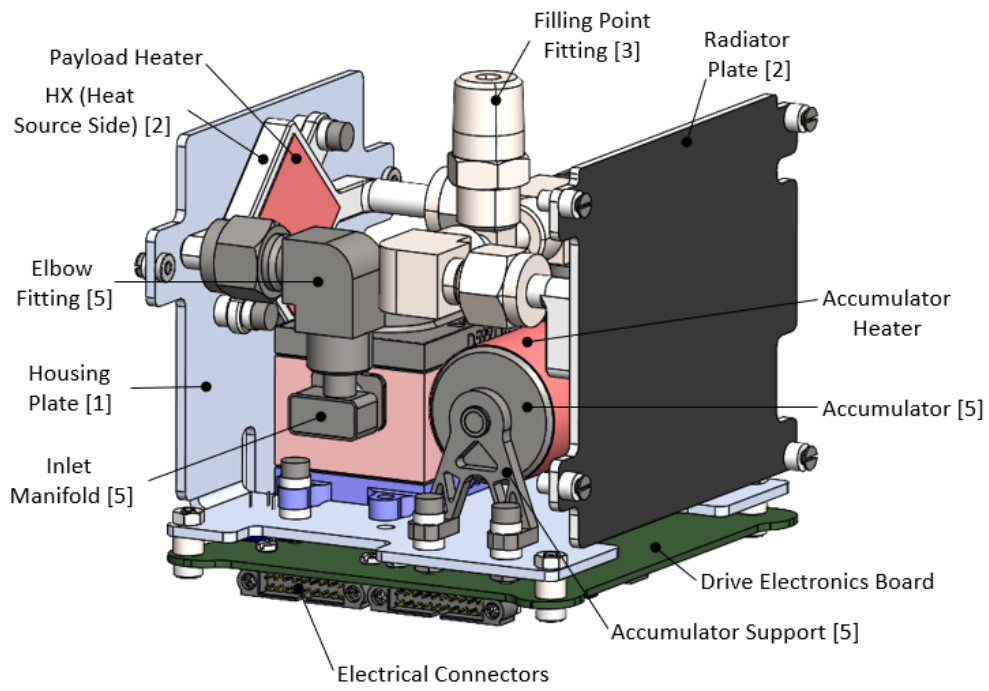


Figure 5.37: Front View of the Final Design.

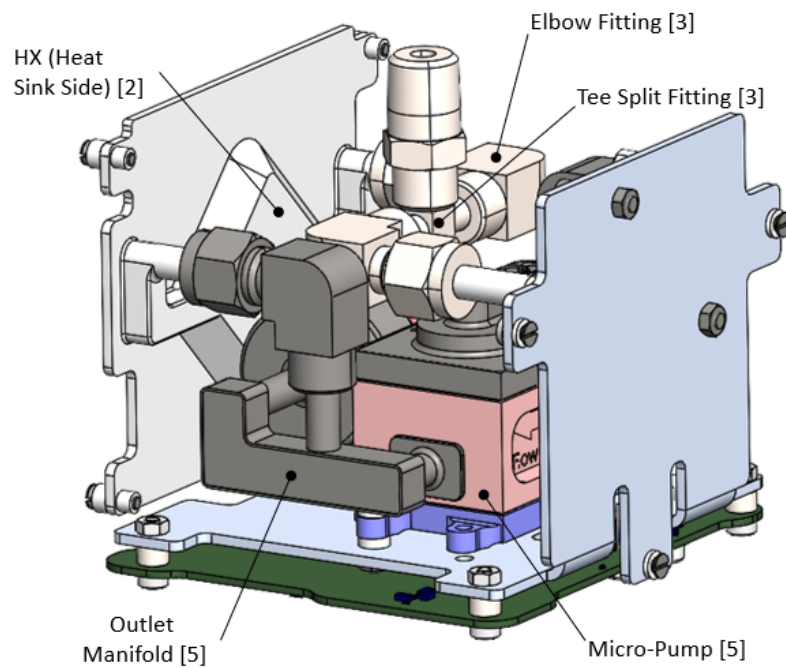


Figure 5.38: Rear View of the Final Design.

6 System Analysis

To validate the design, a full system analysis is carried out. This analysis includes a budget reflection, mechanical analysis, fluidic analysis and thermal analysis. Several simulations and calculations are combined to create an overview of the performance of the system. The main findings of the system analysis are summarized in Chapter 7.

6.1 Budget Reflection

6.1.1 Weight Budget Reflection

Following the weight requirements, the design should weigh less than 1.0 kilogram. Table 6.1 gives an overview of the weight contributions of each component in the system. Using this table, it is found that the total weight is approximately 715 g, which leaves a margin of 285 g that could be spend on sensors and electrical cables or connectors.

Table 6.1: Weight Composition of all Components in the Design.

Category	Components	Quantity	Weight per Component [g]	Total Weight [g]
Main Components	Micro-Pump	1	142.55	142.55
	Drive Electronics	1	53.25	53.25
	Accumulator	1	72.14	72.14
	Radiator Plate / Heat Exchanger	1	55.01	55.01
	Heat Exchanger	1	13.53	13.53
	Housing Plate	1	68.66	68.66
	Pump Inlet Manifold	1	2.53	2.53
	Pump Outlet Manifold	1	7.99	7.99
	Accumulator Heater	1	2.9	2.9
	Heater	1	1.45	1.45
Fittings	Titanium Elbow	2	24.95	49.9
	Compression Fitting 1/4" - Socket Weld 1/4"			
	Stainless Steel Elbow	2	45.21	90.42
	Compression Fitting 1/4" - Socket Weld 1/4"			
	Stainless Steel Tee Split	1	6.51	6.51
	Socket Weld 1/4" - Socket Weld 1/4"			
	Stainless Steel Male Connector Socket Weld 1/4" - Threaded Connection 1/4"	1	27.92	27.92
Fasteners	Jextar Titanium Bolt M3x12	2	0.69	1.38
	Jextar Titanium Bolt M3x14	4	0.75	3.0
	Stainless Steel Bolt M3x10	4	1.11	4.44
	Titanium Nut M3	6	0.23	1.38
	Stainless Steel Nut M3	4	0.41	1.64

Table 6.1: Weight Composition of all Components in the Design.

Category	Components	Quantity	Weight per Component [g]	Total Weight [g]
	Titanium Countersunk Screw M2.5x10	4	0.26	1.04
	Titanium Countersunk Screw M2.5x8	3	0.17	0.51
	Titanium Press-fit Nut M2.5	3	0.05	0.15
Spacers / Bushings	Stainless Steel Spacer M3x4	4	0.65	2.6
	PEEK Spacer M2.5x1	3	0.02	0.06
	PEEK Spacer M2.5x3	4	0.06	0.24
	PEEK Spacer M3x2	4	0.05	0.2
	PEEK Spacer M3x3	2	0.08	0.16
	PEEK Bushing	6	0.06	0.36
Fluid	-	1	102.83	102.83
Total	-	-	-	714.75

6.1.2 Volume Budget Reflection

To fit within 1U of the Cubesat frame, the design has to have maximum outer dimensions of 100 by 100 by 100 mm. However, to actually fit on the inside of the frame, the maximum dimensions have to be reduced even more to fit in the GOMspace satellite frame. Figure 6.1 shows the outer dimensions of the design, including the connectors on the drive electronics board and the outer edge of the screws that attach the design to the satellite frame.

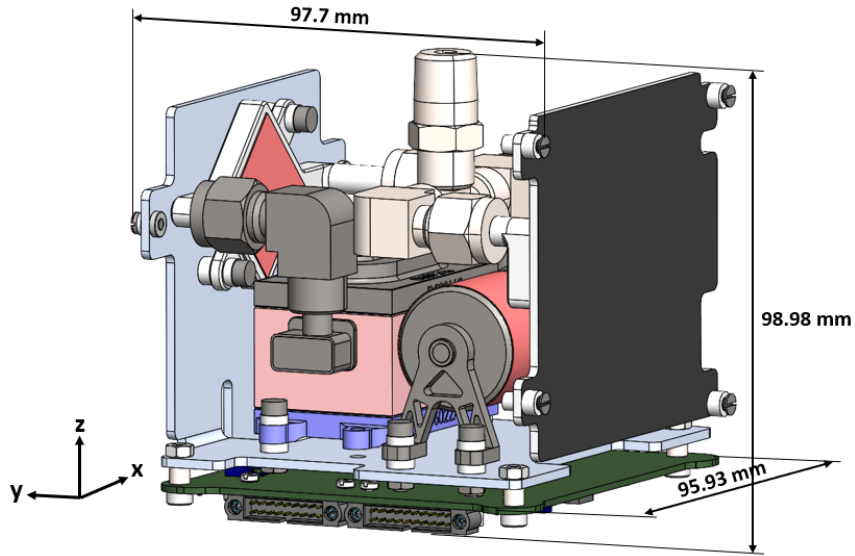


Figure 6.1: Outer Dimensions of the Final Design.

From the figure, it can be seen that the design stays within the boundaries of the maximum dimensions. At first, the margin in the z-direction might seem relatively small, but in reality, the allowed usage of space in this direction is slightly more flexible due to the available space at the top of the satellite frame.

6.1.3 Power Budget Reflection

The power that is available to be used by the system is an average of 5.0 W. By taking into account that one orbit takes approximately 90 minutes, the available energy during one orbit is 7.5 Wh, which is equal to 27 kJ. Table 6.2 gives an overview of all contributions to the total power usage of the system.

Table 6.2: Overview of the Composition of the Power Usage in the System during Operational Mode.

Component	Power Usage @ 12Volt [W]	Average Power Usage [W]	Energy Usage [Wh]
Drive Electronics	0.4	0.4	0.6
Micro-Pump	0.4	0.4	0.6
Heater	3.8	2.0 - 3.0	3.0 - 4.5
Accumulator Heater	1.3	0.3 - 0.6	0.45 - 0.9
Total	5.9	3.1 - 4.4	4.65 - 6.6

As can be seen, the maximum total power usage of the system during one orbit is around 6.6 Wh, which is within the available budget with a margin of 12 %. The variable power usage of the accumulator is based on the thermal analysis in Chapter 6.4. To make sure that the average power usage of the heater and the accumulator heater is equal to the defined usage, these heaters have to be turned on for only a certain percentage of the total orbit time.

6.2 Mechanical Analysis

The mechanical analysis of the system consists of a strength analysis and a vibrational analysis. The strength analysis investigates the ability of the fluidic components to resist the pressure of the fluid, while the vibrational analysis studies the ability of the structural components to withstand the different vibrational loads that the structure is subjected to during its lifetime.

6.2.1 Strength Analysis

To check the ability of the fluidic components to resist the internal pressure build-up of the fluid, a strength analysis is performed. This analysis is based on the pressure that the fluid reaches when its temperature is elevated to 95 °C, which is the maximum temperature that the accumulator is allowed to reach. As can be seen in Figure 4.4, the vapour pressure of the fluid is equal to approximately 3.3 bar at this specific temperature. To perform the analysis, a simulation in Ansys is utilized that uses a distributed pressure over the surface that is in direct contact with the fluid. The components that are taken into account during the strength analysis are the heat exchangers, the accumulator and the manifolds. Other components that are in contact with the fluid are the micro-pump or standard components. The micro-pump is designed to withstand pressures of 3.4 bar during operation and has a burst pressure of 8.5 bar. The standard components like the elbow fittings, the tee splits and the connection fitting are designed to withstand pressures that are two orders of magnitudes higher than the selected pressure.

As an example, the mesh and boundary conditions of the strength simulation of the heat exchanger on the heat source side are visualized in Figure 6.2.

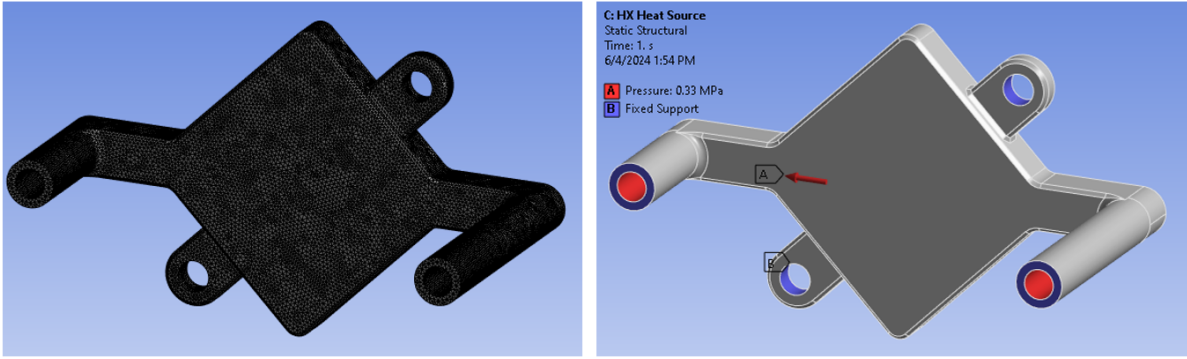


Figure 6.2: The Mesh and Boundary Conditions that are used to perform the Static Structural Analysis in Ansys.

At all locations where the component is fixed to another stiff component, fixed supports are added to make sure that the simulation does not show deformations that are not possible in the assembled design. In reality, the other components are not infinitely stiff like a fixed support, but they are considered stiff enough to model them as a fixed support and still gain valuable insights. On all surfaces where fluid is in contact with the component, a pressure of 3.3 bar or 0.33 MPa is added.

The selected number of mesh elements for the strength analysis in Figure 6.2 is selected to be between 4 and 6 million. In this case, that corresponds to an element size of between 0.2 and 0.3 mm. The selection is made based on a mesh convergence study shown in Figure 6.3, that analyses the convergence of the answer based on the amount of mesh elements used during the simulation. Additionally, the study looks at the simulation time that is needed to perform a simulation based on the amount of mesh elements. It can be seen that the simulation time significantly increases when comparing a simulation with five million elements to a simulation with twelve million elements, while the stress only slightly changes and the changes in deformation are negligible.

The mesh convergence study provides an example of all other simulations that have been performed during this thesis to prevent repetition throughout the report.

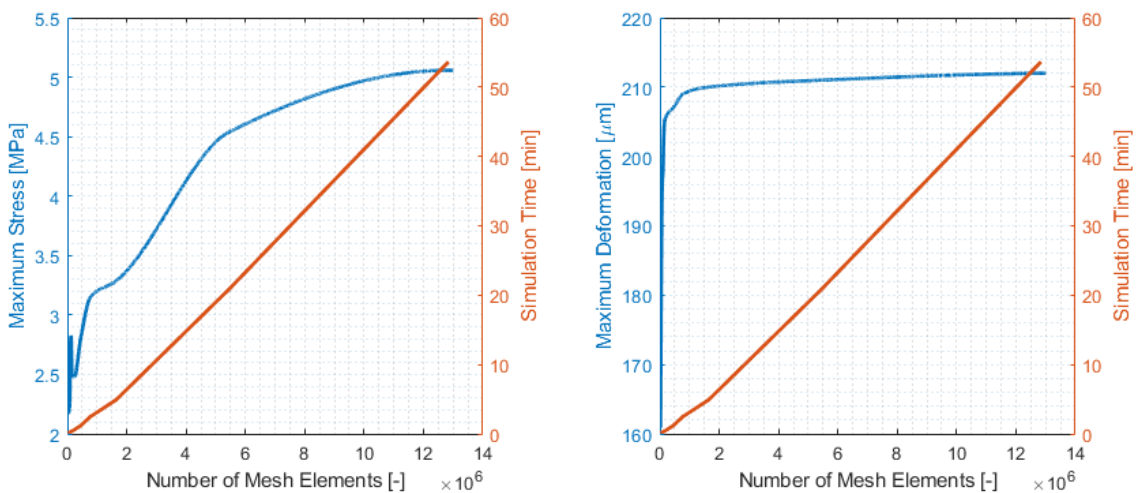


Figure 6.3: Results of the Mesh Convergence Analysis.

The results of the strength analysis for each of the simulated fluidic components can be found in Table 6.3. The table shows the maximum stresses and deformations found in each of the

simulations.

Table 6.3: Maximum Stress and Deformation Results of the Strength Analysis.

Component	Max. Von-Mises Stress [MPa]	Max. Deformation [μm]
Heat Exchanger (Heat Source)	4.51	0.21
Heat Exchanger (Heat Sink)	2.26	0.26
Accumulator	14.12	1.83
Inlet Manifold	24.11	1.37
Outlet Manifold	99.61	9.21

6.2.2 Vibrational Analysis

During handling, transportation, storage, launch and operation of the in-orbit demonstration, its structure is subjected to several vibration loads. Table 6.4 shows an overview of these vibrational loads, directly inherited from the design definition and justification document of the mini-MPL project [9]. Due to computational limitations, the shock vibrations and quasi-static vibrations could not be performed. These transient simulations would take several days and are therefore not included in this report.

Table 6.4: Vibrational Load to which the In-Orbit Demonstration is subjected during Transportation, Storage, Launch and Operation.

Vibration Environment	Frequency Levels [Hz]	Acceleration Levels / Spectral Density
Sine Vibrations	5-100	5-8 Hz \rightarrow 1.7g 8-100 Hz \rightarrow 4.5g
Random Vibrations	20-2000	20 Hz \rightarrow 0.026 g^2/Hz 20-50 Hz \rightarrow +6dB/oct 50-800 Hz \rightarrow 0.16 g^2/Hz 800-2000 Hz \rightarrow -6dB/oct 2000 Hz \rightarrow 0.026 g^2/Hz Overall Level (RMS): 14.1g
Shock Vibrations	0-10000	100 Hz \rightarrow 30g 1000 Hz \rightarrow 1000g 3000 Hz \rightarrow 1000g 5000 Hz \rightarrow 1000g 10000 Hz \rightarrow 1000g
Quasi-static Vibrations	< 1/3 Satellite Resonance Frequency	15g

This section covers each vibration type to take a more detailed look at the vibration type and to simulate the maximum deformations and stresses that occur for the simulated vibrations. To do so, the connections of the design to the satellite frame are assumed to be fixed supports. Additionally, the fluid is modelled as a distributed mass at the components in the system that contain a significant amount of fluid. The mass of the fluid is added to the system, since this influences the inertia of the system and therefore also its dynamic behaviour. The location of the fixed supports and the distributed masses can be seen in Figure 6.4.

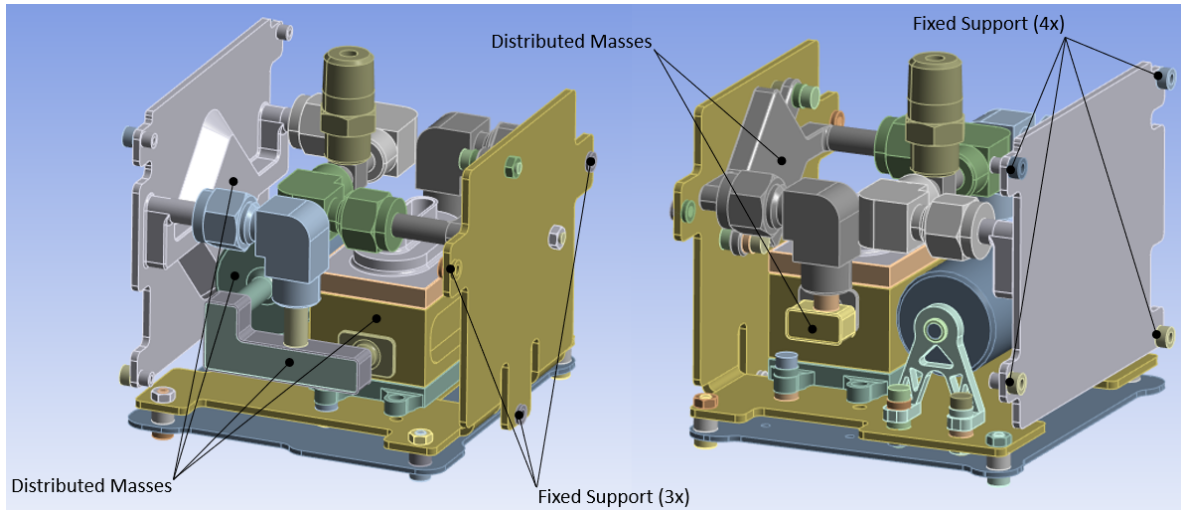


Figure 6.4: Setup of the Vibrational Analysis.

As a first step in the vibration analysis, a modal analysis is performed. This type of analysis simulates the eigenmodes of the structure at the calculated eigenfrequencies that form the basis of the dynamic behaviour of the structure. Table 6.5 shows the eigenfrequencies of the design up to 2000 Hz.

Table 6.5: Eigenfrequencies of the Design between 0 - 2000 Hz.

Mode	Frequency [Hz]	Mode	Frequency [Hz]	Mode	Frequency [Hz]
1	160.17	14	649.85	27	1352.7
2	188.73	15	706.31	28	1391.5
3	255.1	16	756.43	29	1422.5
4	273.29	17	764.49	30	1437.7
5	337.87	18	816.87	31	1521.6
6	398.6	19	914.16	32	1563.1
7	421.83	20	956.55	33	1666.4
8	480.33	21	985.97	34	1697.9
9	515.0	22	1076.6	35	1717.7
10	526.53	23	1087.1	36	1751.3
11	553.88	24	1108.9	37	1933.
12	599.64	25	1187.8	38	1958.5
13	637.34	26	1246.5	39	2003.9

Sine Vibrations Sine vibrations subject the model to a swept sine input over a specified frequency range, which in this case is from 5 to 100 Hz. These types of vibrations represent the low-frequency launch environment during take-off [43]. To gain all relevant information about the maximum deformations and stresses, three different simulations are performed in which the direction of the input acceleration is changed for each simulation to cover all three axes. Figure 6.5 gives an overview of the maximum deformations and stresses that occur in the system for each of the three axes.

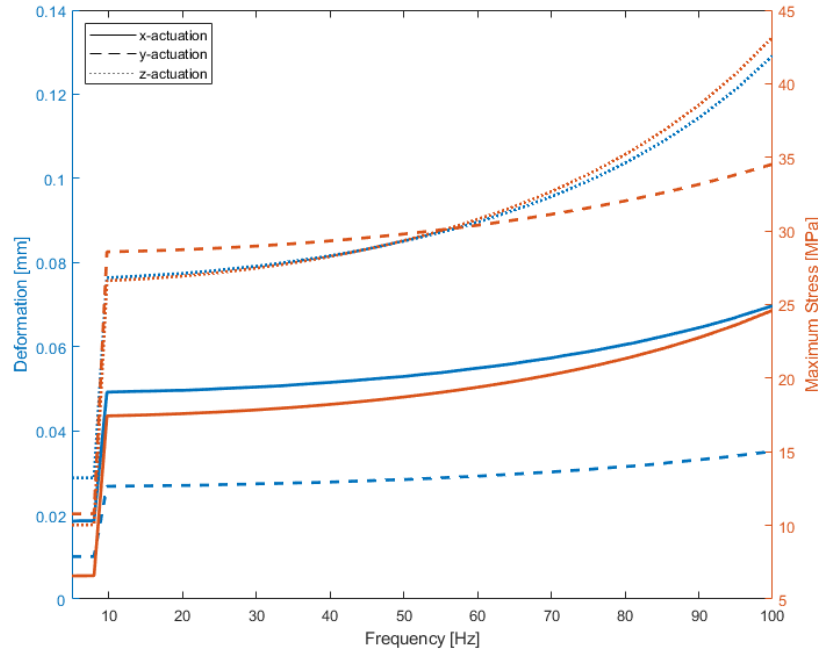


Figure 6.5: Maximum Stress and Deformations of the design when subjected to Sine Vibrations as specified in Table 6.4.

From this figure, it becomes clear that the largest deformations and stresses occur when the acceleration is applied in the z-direction. Something that stands out from the results is that the deformations caused by accelerations in the y-axis are the lowest of the three axes, while the stresses caused by this type of actuation are among the highest found in the simulations. This could indicate that the structure is relatively stiff in the y-direction, while still being vulnerable for stress concentrations.

Although the stresses seem to increase for higher frequency acceleration cycles, the stresses do not get close to the yield stress of any of the involved materials. Therefore, it can be assumed that the design can safely withstand the sine vibrations environment.

Random Vibrations Random vibrations are a type of vibrations in which the amplitude does not follow a regular pattern. The random vibrations are described by an acceleration spectral density, which can be found in Table 6.4. The results of such an analysis is interpreted using a confidence interval, which describes the likelihood that the actual results will stay within a certain range. Figure 6.6 gives a visual representation of the confidence interval of the three sigma method. In this method the standard deviation of the results is added on both sides of the mean once or multiple times to create a confidence interval of 68.27%, 95.45% or 99.73%.

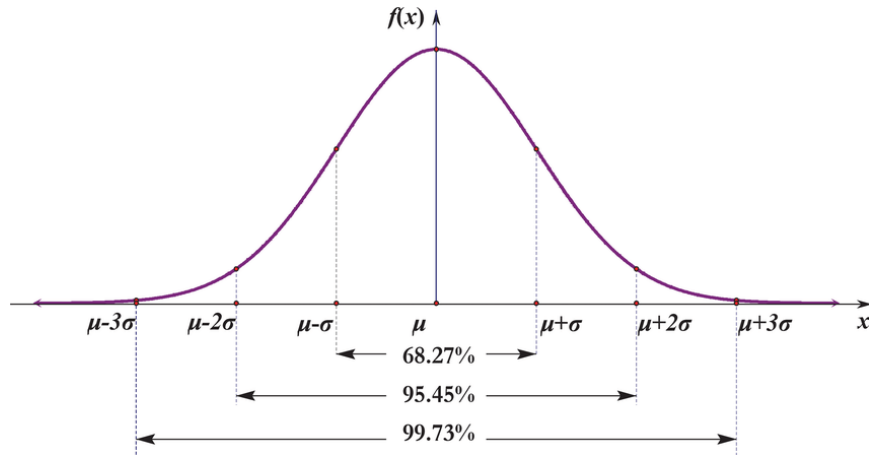


Figure 6.6: Visual Representation of the Confidence Interval of the Three Sigma Method. [44]

The final results of the analysis can be found Table 6.6. Just like for the sine vibrations, the simulation is performed for actuation in all three axes to get a full picture of the response of the structure to these type of vibrations. Additionally, the deformation results are split in directional deformations for all three axes as well.

Table 6.6: Overview of the Results of the Random Vibrations Analysis.

Confidence Interval	Actuation Axis	Max. Deformation x-axis [mm]	Max. Deformation y-axis [mm]	Max. Deformation z-axis [mm]	Max. Von-Mises Stress [MPa]
One Sigma	x-axis	0.40	0.33	0.27	191.3
	y-axis	0.24	0.21	0.30	190.86
	z-axis	0.18	0.20	0.58	279.05
Two Sigma	x-axis	0.80	0.65	0.54	382.61
	y-axis	0.47	0.42	0.60	381.71
	z-axis	0.37	0.41	1.15	558.11
Three Sigma	x-axis	1.19	0.98	0.81	573.91
	y-axis	0.71	0.63	0.90	572.57
	z-axis	0.55	0.61	1.73	837.17

From these results it becomes clear that these type of vibrations have a larger impact on the design compared to the sine vibrations. The highest directional deformations and stresses are found in the z-direction when the design is subjected to random vibrations in the z-axis.

These high stresses mainly show up at the interfaces of the titanium parts, as these are modelled to have chamfers at the connection points. These chamfers act as a way to make welding more convenient during the welding process of the titanium parts. However, in reality, these welding locations will be stronger due to the extra material that is added when welding the part. Therefore, the stress concentrations in these specific locations will not be a concern during the real shaker tests. Next to these stresses, other stress concentrations can be found in the overhanging tubes that fluidically connect the two heat exchangers. In the three sigma case, these stresses reach between 200 and 300 MPa, which will not cause the stainless steel tubes to yield.

Shock Vibrations To test the resistance of the design structure to shock vibrations, a shock vibration simulation has to be performed. Such a shock vibration is represented by a relatively large acceleration that occurs within a fraction of a second and has to be simulated using a transient simulation. Figure 6.7 visualizes the acceleration profile of a shock vibration.

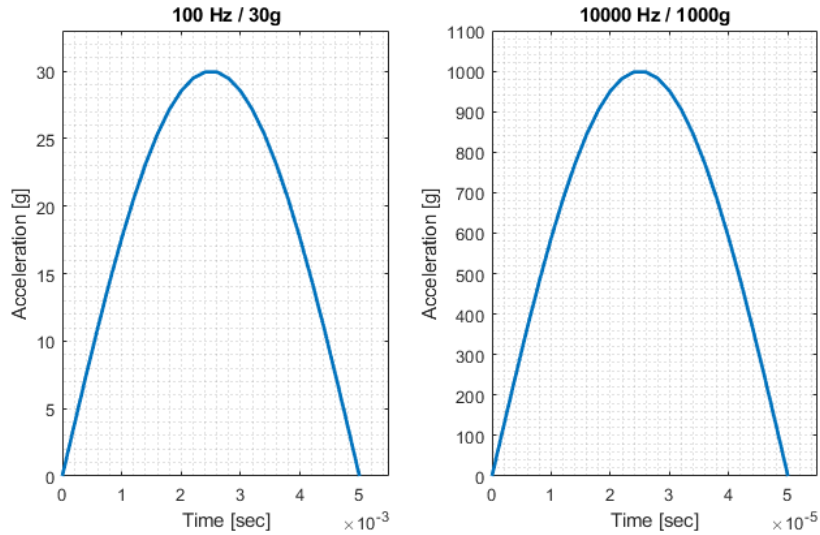


Figure 6.7: Shock Vibration Acceleration Profile for the 100 Hz and 10000 Hz Load Cases.

As has been stated before, this vibration type could not be simulated due to limitations in computing power available in this research.

Quasi-static Vibrations To test the ability of a structure to deal with static loading, multiple methods can be used. Two of these methods are centrifuge testing and sine-burst testing. The first method, in which a structure is placed in a centrifuge and rotates to imitate static loading, requires an expensive test setup. In the second method, the structure is subjected to multiple cycles of sine-burst waves, one of which is visualized in Figure 6.8. This type of quasi-static testing can be performed using the same shaker setup that is used to perform the sine and random vibration testing, which makes testing more efficient and cost-effective.

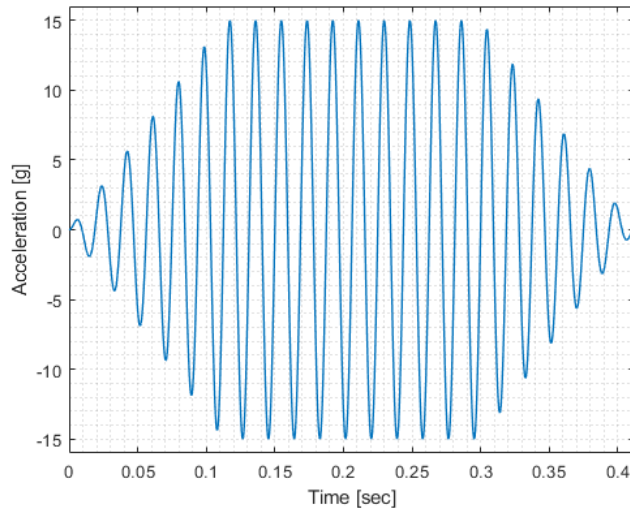


Figure 6.8: Sine-burst acceleration Profile at one-third of the resonance Frequency and 15g Acceleration.

To prevent resonance from taking place, the frequency of the sine-burst cannot be higher than one-third of the first resonance frequency of the structure. In this case, that would result in a maximum sine-burst frequency of 53.33 Hz [45,46]. As has been stated before, this vibration type could not be simulated due to limitations in computing power available in this research.

6.3 Fluidic Analysis

As has been mentioned in Section 4.1.3, the pump is able to deliver around $0.7 \frac{g}{s}$ of flow at a pressure head of 25 mbar. To make sure that the pump is able to deliver this performance in the final design, an analysis of the fluidic resistance is made. In Section 5.3.1, a preliminary analysis has already been performed in the selection process of the tubing. Within this section, a more extensive fluidic analysis that takes into account the straight tubing, fittings, heat exchangers, micro-pump, manifolds and changes in flow area. Figure 6.9 shows an overview of all the different fluid resistances that should be added up to get to the final fluidic resistance of the system.

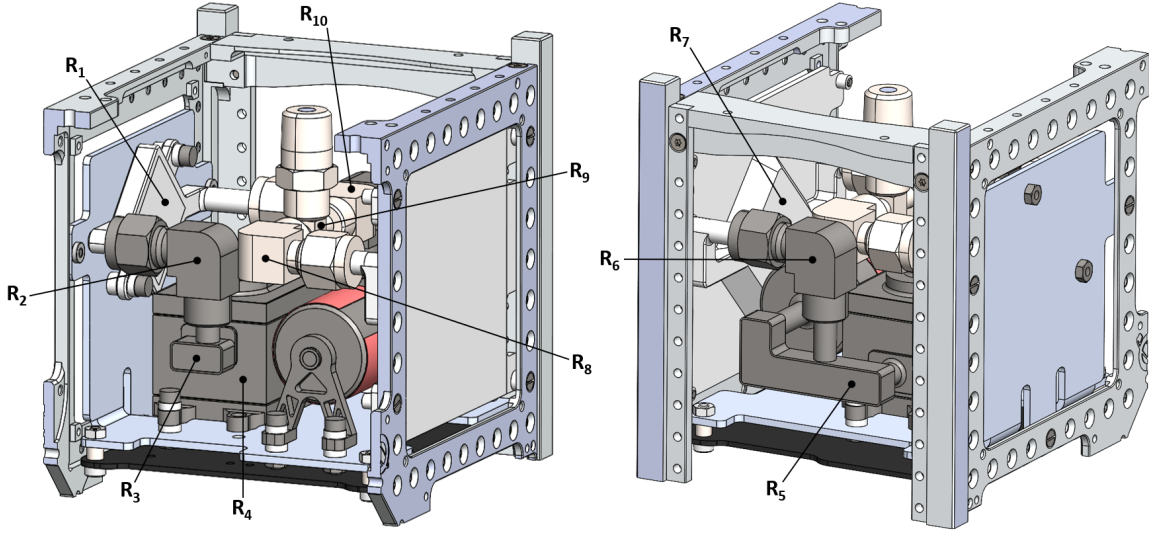


Figure 6.9: Overview of the locations of all Fluid Resistances within the System

Table 6.7 lists all fluidic resistances and gives a more detailed overview of the composition of these resistances. For example, it lists the different bends, expansions / reductions and straight tubing of each component. Only the pump does not have any further specifications, since its pressure drop is already known. The pressure drop due to expansion or reduction of the flow path is calculated using the equation

$$\Delta p = K_{\text{exp/red}} \frac{\langle v \rangle^2}{2g}. \quad (6.1)$$

The value of K depends on the geometry and connection type of the two tubes in question as well as whether expansion or reduction takes place. All types of expansions and reductions in the final design are square expansions and reductions. The values of K for the square type expansions are calculated using the equation

$$K_{\text{exp}} = 2 \left[1 - \left(\frac{D_{h1}}{D_{h2}} \right)^4 \right], \quad (6.2)$$

while the loss factors for reductions are calculated using the equation

$$K_{\text{red}} = \left(1.2 + \frac{160}{\text{Re}_1} \right) \left[\left(\frac{D_{h1}}{D_{h2}} \right)^4 - 1 \right]. \quad (6.3)$$

In both equations, the subscript one represents the inlet channel and two represents the outlet channel. Equation 6.2 is valid for Reynolds numbers below 2500, while Equation 6.3 is valid for Reynolds numbers below 4000. In the current system, the Reynolds number does not exceed these values.

Table 6.7: Overview and Composition of Fluidic Resistances within the System.

Number	Description	Composition	Number	Description	Composition
R1	Heat Exchanger Source	- Fin Geometry	R6	Titanium Fitting 2	- Bends:
		- Bends:			- 45 Mitered Bend (1x)
		- Round Bend (2x)			- Straight Tubing:
		- Straight Tubing:			- 19.3 mm / \varnothing 4.82 mm
		- 78.2 mm / \varnothing 4.0 mm			- Reduction (1x)
		- Expansion / Reduction (4x)			
R2	Titanium Fitting 1	- Bends:	R7	Heat Exchanger Sink	- Fin Geometry
		- 45 Mitered Bend (1x)			- Bends:
		- Straight Tubing:			- Round Bend (4x)
		- 19.3 mm / \varnothing 4.82 mm			- Straight Tubing:
		- Reduction (1x)			- 113.7 mm / \varnothing 4.0 mm
					- Expansion / Reduction (4x)
R3	Inlet Manifold	- Bends:	R8	Stainless Steel Fitting 1	- Bends:
		- 90 Mitered Bend (2x)			- 45 Mitered Bend (1x)
		- Straight Tubing:			- Straight Tubing:
		- 13 mm / \varnothing 4.57 mm			- 19.3 mm / \varnothing 4.82 mm
		- 5.2 mm / 6.0x6.5 mm			- Reduction (1x)
		- Expansion / Reduction (2x)			
R4	Micro-pump	-	R9	Three-way Fitting	- Straight Tubing:
					- 35.4 mm / \varnothing 4.57 mm
					- Expansion (1x)
R5	Outlet Manifold	- Bends:	R10	Stainless Steel Fitting 2	- Bends:
		- 90 Mitered Bend (2x)			- 45 Mitered Bend (1x)
		- Straight Tubing:			- Straight Tubing:
		- 14.8 mm / 6.0x6.5 mm			- 19.3 mm / \varnothing 4.82 mm
		- 20.0 mm / \varnothing 4.57 mm			
		- Expansion / Reduction (3x)			

By adding the pressure drop of expansions and reductions to the pressure drop of straight tubing and bends, the total pressure drop is calculated using the equation

$$\Delta p_{\text{tot}} = \sum K_L \frac{\rho_f \langle v \rangle^2}{2} + \sum f \frac{L}{D_h} \frac{\rho_f \langle v \rangle^2}{2} + \sum K_{\text{exp/red}} \frac{\langle v \rangle^2}{2g}. \quad (6.4)$$

Results Figure 6.10 shows the total pressure drop of the system as a function of the fluid temperature at the mass flow of $0.7 \frac{\text{g}}{\text{s}}$. Additionally, it shows the share of each type of pressure drop that contributes towards the total pressure drop. The figure shows that the expansions and reductions of the flow path at different points in the loop have a relatively small influence on the total pressure drop in the system. The largest contributor to the pressure drop throughout the system is the different types of bends. The straight tubing and heat exchanger fin geometry have a similar contribution, which is relatively small.

In a worst-case scenario, the total pressure drop throughout the loop is only around 3.4 mbar, which is only 13.6% of the allowed pressure drop of 25 mbar. Therefore, the pump is considered to have no difficulties with the pressure drop in the system and will adjust its mass flow to find the operating point of the pump. Figure 6.11 shows a schematic representation of how the system and the pump find their equilibrium operating point. Depending on the pressure drop in the system, the pump will operate at a certain point along the pump curve that matches the pressure drop.

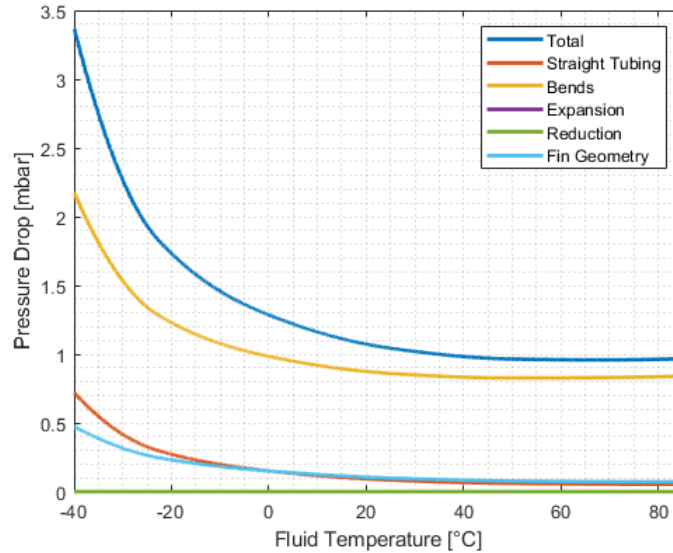


Figure 6.10: Total Pressure Drop within the System vs. System Temperature at a Mass Flow Rate of $0.7 \frac{\text{g}}{\text{s}}$.

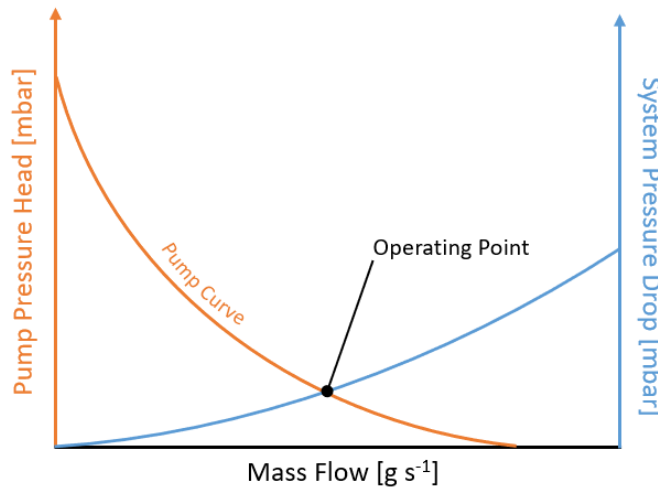


Figure 6.11: Operating Point of the Closed Loop.

6.4 Thermal Analysis

To gain more insight into the thermal performance of the system, two separate thermal analyses are carried out. The first analysis is based on a simplified thermal network that utilises theoretical calculations to determine thermal resistances within the system. The second analysis is based on a thermal simulation using Ansys steady-state thermal. Both analyses are compared to validate the outcomes. Both of these analysis types use the same boundary conditions, that are shown in Figure 6.12. As boundary conditions, four incoming heat sources are defined at the dummy heat source, the drive electronics, the micro-pump and the radiator plate. Additionally, three constant temperatures are defined at the accumulator, the frame and space. The accumulator is kept at a constant temperature of $90 \text{ }^\circ\text{C}$ using the accumulator heater. The frame is found to have a temperature between $-5 \text{ }^\circ\text{C}$ and $35 \text{ }^\circ\text{C}$, based on calculations of the system integrator over the full orbit of the satellite during different times of the year [18]. Deep space is assumed to have a temperature of $-269.15 \text{ }^\circ\text{C}$. Out of all these conditions, the heat flux at the heater and the constant frame temperature will be modified between simulations to analyse different configurations.

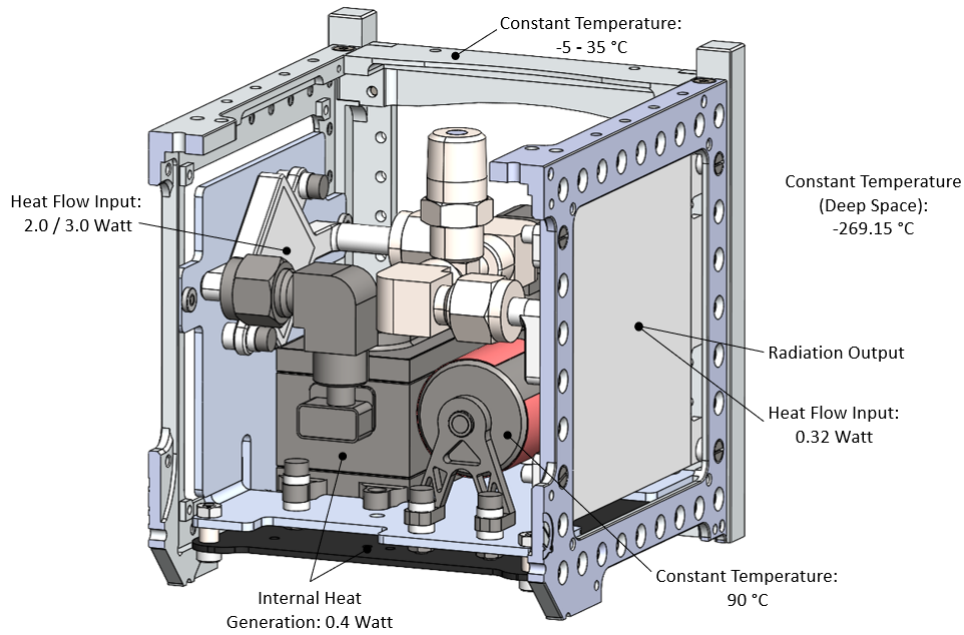


Figure 6.12: Overview of the Setup of the Thermal Analysis Boundary Conditions.

An important simplification within the thermal analysis is that the components do not radiate to each other and the only body that radiates into space is the radiator plate. The other components are assumed to be isolated from radiating into space by the layer of MLI that is wrapped around the in-orbit demonstration.

Interesting results from these two types of analyses are the temperatures throughout the system, the heat fluxes between the components and the fraction of heat that leaves the system through radiation compared to conduction into the frame.

6.4.1 Theoretical Approach on the System Thermal Analysis

When taking a look at the CAD model of the full design, it can be simplified to a one-dimensional thermal network consisting of eight temperature locations that are connected using thermal resistances. Figure 6.13 shows the temperatures and the thermal resistances that are used to create the simplified thermal model.

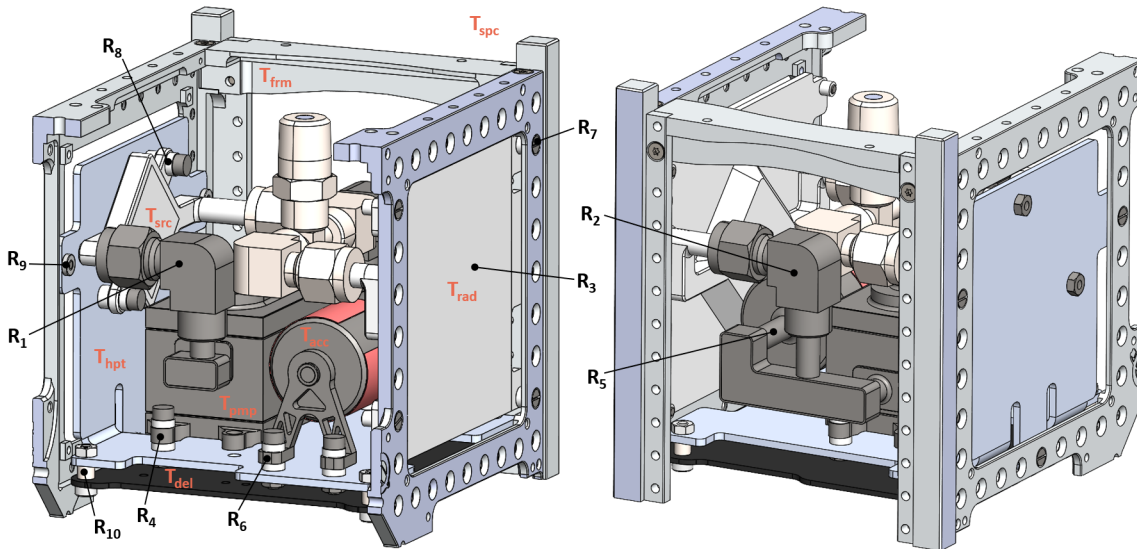


Figure 6.13: Temperature Points and Thermal Resistances that are used to build the Simplified Thermal Network

Using the temperature points and thermal resistances of Figure 6.13 and combining them with the boundary conditions of Figure 6.12, the thermal network is created. This thermal network, which is visualized in Figure 6.14, represents the entire system and assumes that each component has a constant temperature throughout the entire body. This is a simplification of reality, which indicates that the model is used as an estimation. As has been stated before, the actual validity of this method is tested using Equation 5.14, which calculates the Biot number. When the Biot number is much smaller than one, which is common for relatively small metal structures in the vacuum of space, the method is known to be sufficiently accurate.

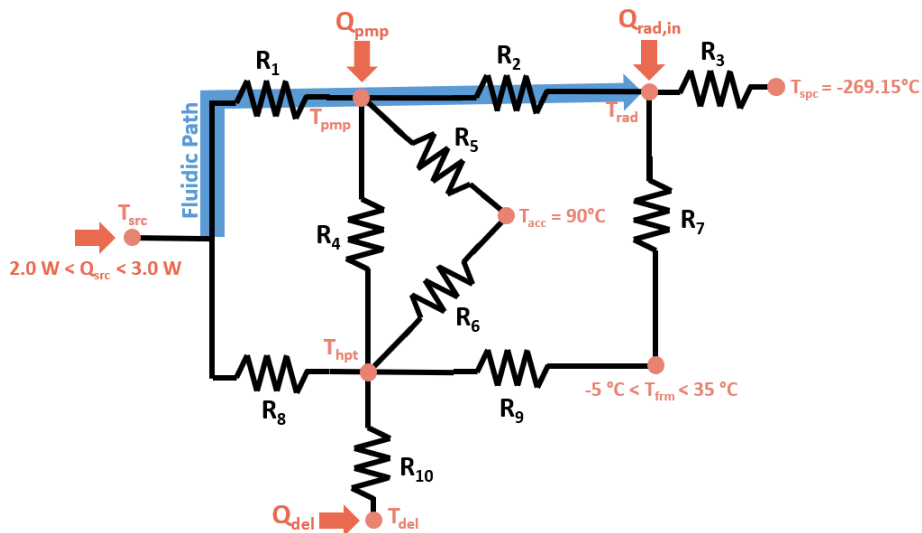


Figure 6.14: One dimensional Thermal Network that represents the simplification of the 3D model.

Thermal Resistance Calculations Within the system, several different types of thermal resistances are present. The most occurring thermal resistance is a conductive resistance, which is present at all bolted connections. Two more thermal resistances are a radiative resistance at the radiator plate and conductive resistances at the interface of the fluid with the heat exchangers

at the heat source and the heat sink.

The conductive resistances at the heat exchangers are included in the total fluidic thermal resistance, which is represented by resistances one and two, as can be seen in Figure 6.14 where the fluidic path is marked in blue. Furthermore, thermal resistances five and six represent the losses of the accumulator to the system and resistances seven and nine represent the thermal losses of the system to the satellite frame.

To calculate resistances one and two, the total fluidic thermal resistance, which can be calculated using Equation 5.26 is split in two parts. The first part is the fluidic path from the heat source to the micro-pump, while the second part is the path that the fluid takes from the pump to the heat sink. Added to this are the resistances of the heat exchangers and the fluid.

The only radiative resistance in the system is variable, since it depends on the temperature of the radiator plate. To calculate this resistance for a certain moment in time, the equation

$$R_{\text{rad}} = R_3 = \frac{T_{\text{rad}} - T_{\text{spc}}}{\epsilon_{\text{rad}} \sigma_b F_{\text{rad}} A_{\text{rad}} (T_{\text{rad}}^4 - T_{\text{spc}}^4)}, \quad (6.5)$$

is used. All other resistances are conductive and are calculated in a similar manner that assumes perfect thermal contact between all participating surfaces. Resistances five and six have already been partially calculated before in Section 5.4, where an estimation of the accumulator losses are made. Although, due to the bolted connection of the accumulator support to the housing plate an additional resistance is added.

To show the manner in which the conductive thermal resistances of the bolted connections have been calculated, the connection of the accumulator to the housing plate is used as an example. Figure 6.15 shows the simplified model of the bolted connection that is used to calculate the thermal resistance.

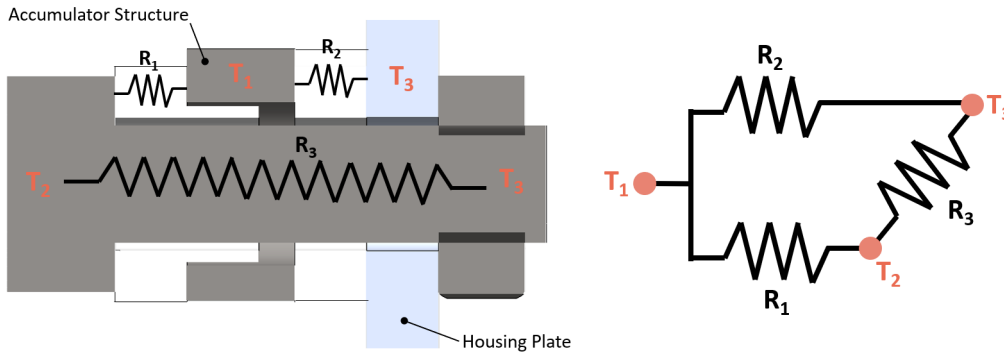


Figure 6.15: Simplified Model that is used to calculate the Thermal Resistances of the Bolted Connections.

In this model, the major resistances are used to calculate the temperature differences throughout the connection. In reality, additional resistances would be in place at the interfaces of the different materials and at the bolt head and bolt nut where the heat would have to travel around the corner. However, for an estimation of the thermal resistance, the simplified model is considered to be sufficient. Moreover, in the real world, these extra resistances would only be beneficial to the design, which means that the model acts as the analysis of a worst-case scenario.

The thermal resistance in the bolted connections is calculated using the equation

$$R_{\text{cond}} = \frac{L}{k A}. \quad (6.6)$$

This equation takes both the geometry of the connection and the material properties into account. The numerator consists of the length through which the heat has to travel. The denominator contains the thermal conductivity of the material through which the heat is travelling as well as the area through which the two materials are connected. During these calculations the thermal conductivity is assumed to be constant, while in reality, it varies for temperature. However, the assumption can be justified as the thermal conductivity of the used materials does not vary much in the temperature range $-45\text{ }^{\circ}\text{C}$ to $85\text{ }^{\circ}\text{C}$ of the in-orbit demonstration [47–51]. Using this method, all conductive resistances in Figure 6.14 have been calculated and can be found in Table 6.8.

Table 6.8: Overview of the Thermal Resistances of the Simplified Thermal Model.

Number	Type	Thermal Resistance [K/W]	Remarks
R1	Conductive / Convective	1.075	Heat exchanger thermal resistance plus half of the total fluid thermal resistance.
R2	Conductive / Convective	1.075	Heat exchanger thermal resistance plus half of the total fluid thermal resistance.
R3	Radiative	Variable	Thermal resistance depends on the temperature of the radiator plate.
R4	Conductive	137.5	-
R5	Conductive	415	-
R6	Conductive	325	Accumulator support thermal resistance plus bolted connection thermal resistance.
R7	Conductive	23	-
R8	Conductive	150	-
R9	Conductive	21	-
R10	Conductive	6	-

Using all the known boundary conditions and thermal resistances, Simulink is used to solve the system and calculate all equilibrium temperatures and heat fluxes in the system.

Results Figure 6.16 shows the equilibrium temperatures of the heat sink and heat source related to the satellite frame temperature for a 2.0 and a 3.0 W heater.

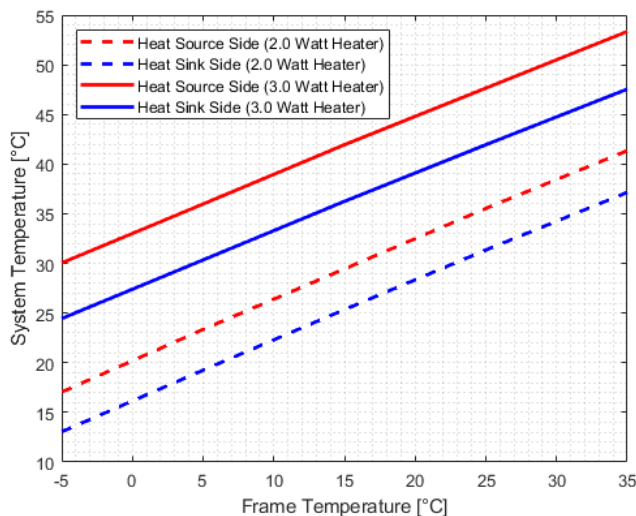


Figure 6.16: Equilibrium Temperatures of the Heat Sink and Heat Source vs. Satellite Frame Temperature during Operational Mode.

This figure shows that the maximum system temperature of 85 °C will not be exceeded in any case. It also shows that the temperature difference between the heat source and heat sink is approximately 5 to 6 °C.

In Figure 6.17, the most important heat fluxes are shown for a 2.0 and 3.0 W heater. These most important heat fluxes are the total input power, the energy that is radiated into space via the radiator plate, the energy that is lost to conduction into the satellite frame and the energy that is lost by the accumulator by conduction through its inlet and support structure.

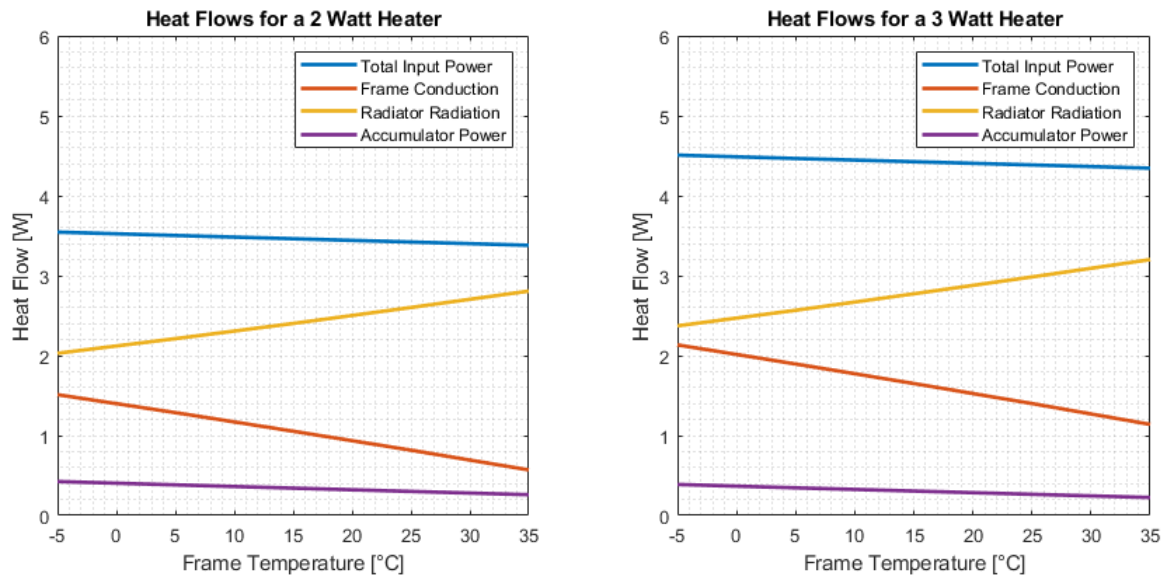


Figure 6.17: Equilibrium Heat Flows vs. Satellite Frame Temperature during Operational Mode.

The efficiency of this design is defined as the percentage of the total input heat that is removed from the system using the radiator plate. Figure 6.18 shows this efficiency related to the temperature of the satellite frame.

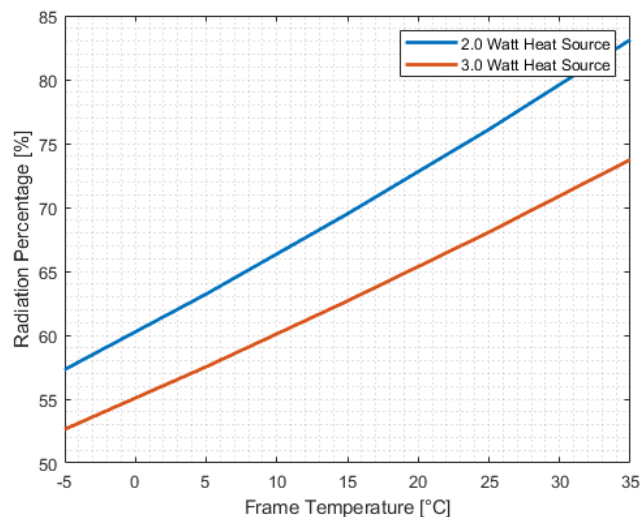


Figure 6.18: System Efficiency vs. Satellite Frame Temperature during Operational Mode.

Two important findings from this figure are that the efficiency of the system increases if the frame temperature increases and that the system is more efficient for a 2.0 W heater compared to a 3.0 W heater. The first finding can be explained by the fact that a higher frame temperature causes the temperature difference between the system and the frame to be lower, causing less heat to

be lost into the frame to conduction. The same reasoning applies to the second finding, since a higher heater power causes the temperature of the system to increase, which also increases the temperature difference between the system and the frame. This causes the loss of energy through conduction into the satellite frame to increase, which decreases the efficiency of the design.

6.4.2 FEM Simulations on the System Thermal Analysis

To confirm the simplified thermal analysis of Section 6.4.1, a second thermal analysis is performed using Ansys steady-state thermal. This type of analysis can provide a high resemblance to reality since the model uses the finite element method that splits the model into many small elements and creates an energy balance over each of the elements separately. To make sure that the model is defined in exactly the same way as the simplified model, the same boundary condition, that can be found in Figure 6.12, are utilized.

Figure 6.19 shows the mesh that is created to divide the entire model into small elements. The mesh is automatically generated by Ansys, which modifies the size of the elements based on the size of the component that it is meshing. For this mesh, the highest possible default resolution is selected to gain the most accurate results. The mesh consists of over 1.5 million nodes and around 0.85 million elements. The figure also shows the boundary conditions as they show in Ansys. The thermal contact between the components is considered to be perfect to analyse the worst-case scenario, where maximum conduction into the satellite frame will take place.

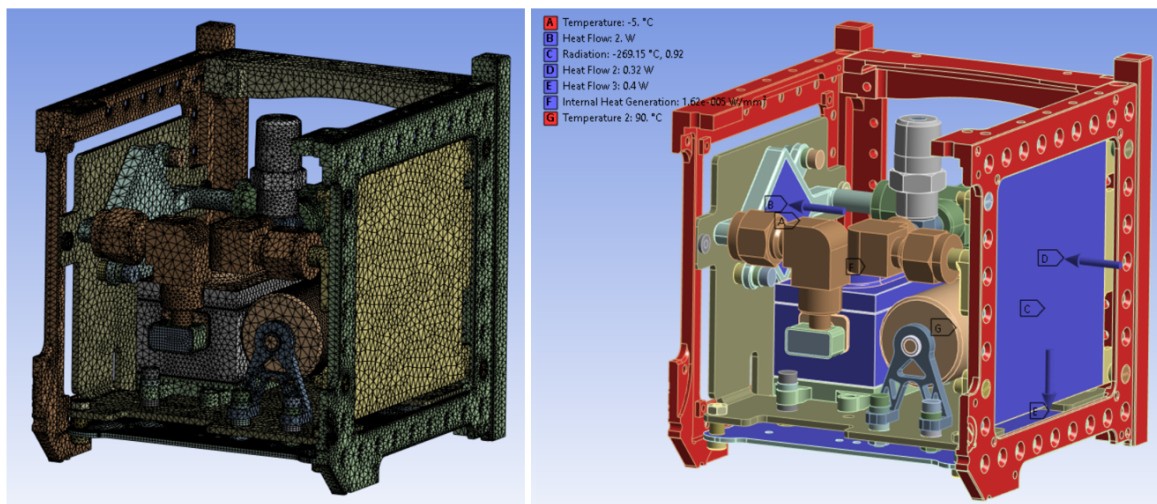


Figure 6.19: The Mesh and Boundary Conditions that are used to perform the Steady-state Thermal Analysis in Ansys.

To model the fluid, a solid is added within the fluidic loop that has a thermal resistance equal to the fluid thermal resistance that is calculated in Section 6.4.1. To do so, the thermal conductivity of the solid material that represents the fluid is modified to equal this thermal resistance using Equation 6.7.

$$k_f = \frac{L_f}{R_f A_f} \quad (6.7)$$

In this equation L_f , R_f and A_f represent the length, thermal resistance and average cross-sectional area of the fluidic connection between the heat sink and heat source respectively. To make sure that the model does not transfer a relevant amount of heat from the heat source to the heat sink against the flow of fluid, the fluidic connection between the heat sink outlet and the heat source inlet is removed.

An addition to the state in which the system is pumping the fluid around, which is defined as the operational mode, another simulation is carried out using Ansys where both the heat source and the pump are turned off. In this case, which is defined as the rest state, only the accumulator heater and the drive electronics produce heat.

Results Figures 6.20 and 6.21 show the equilibrium temperatures of the heat sink and heat source and the most relevant heat fluxes in the system related to the satellite frame temperature for a 2.0 and 3.0 W heater. Figure 6.22 shows the efficiency of the system which is defined as the percentage of the total heat input that leaves the system through the radiator plate.

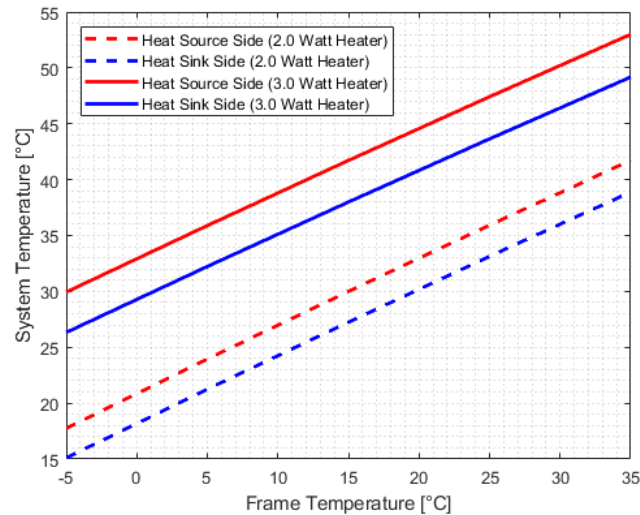


Figure 6.20: Equilibrium Temperatures of the Heat Sink and Heat Source vs. Satellite Frame Temperature during Operational Mode.

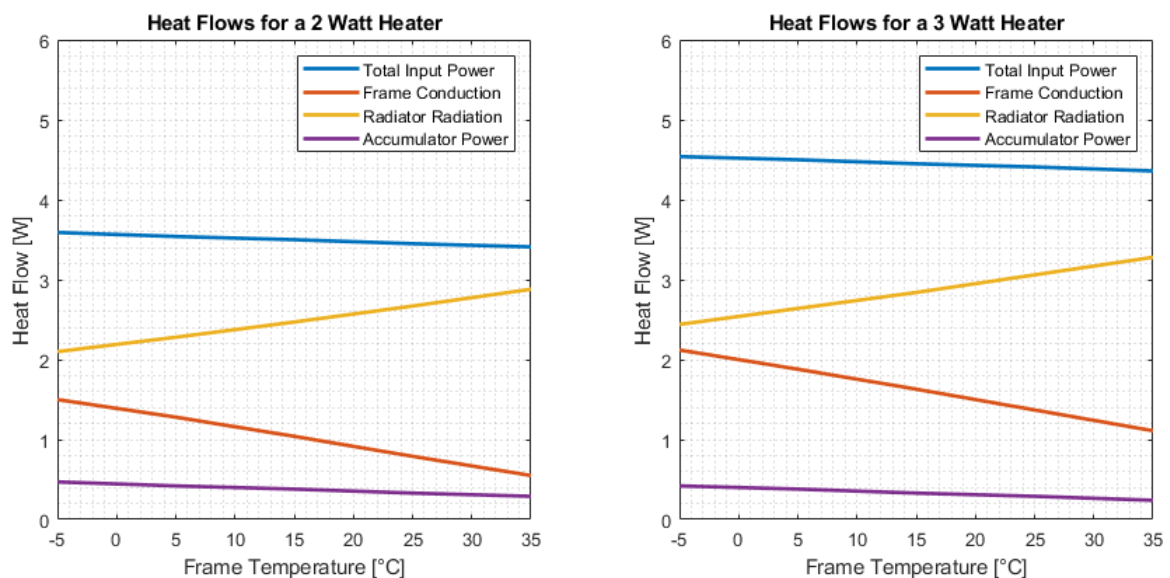


Figure 6.21: Equilibrium Heat Flows vs. Satellite Frame Temperature during Operational Mode.

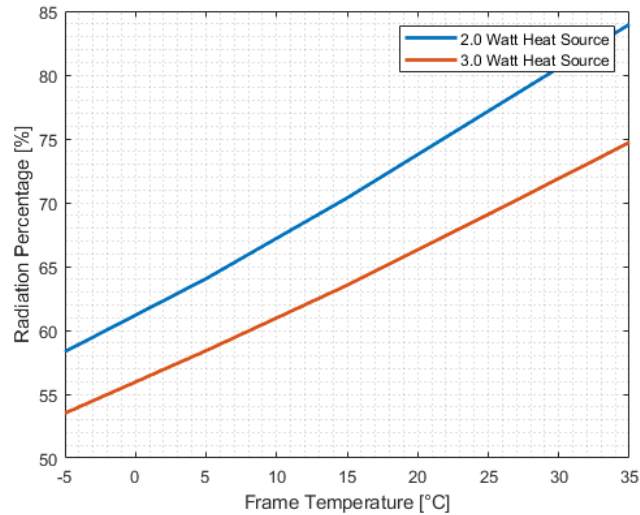
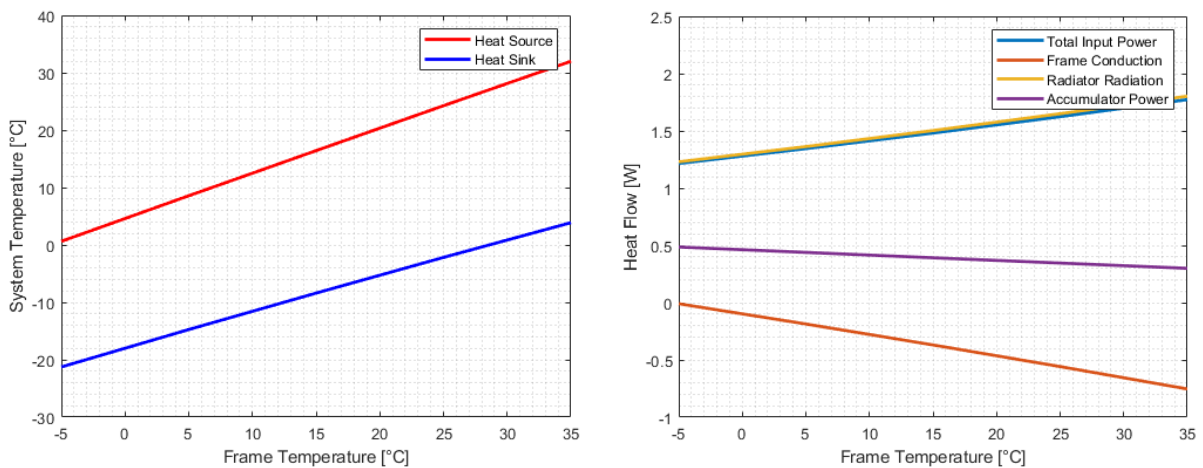


Figure 6.22: System Efficiency vs. Satellite Frame Temperature during Operational Mode.

When comparing the results of the Ansys model to the simplified thermal model of Section 6.4.1, many similarities can be found. One of the major differences in the results is that the simplified model finds a temperature difference between the heat source and the heat sink of five to six degrees, while the simulation in Ansys finds a temperature difference of approximately three degrees. The reasoning behind this could be that the thermal resistance of the heat exchangers or the fluid is not modelled accurately. Another reason could be the thermal link between the heat source and the heat sink in the opposite fluid flow direction that is present in the Ansys model, but not in the simplified model.

Although the two models do not line up perfectly for the temperature difference between the heat source and heat sink, the heat fluxes and system efficiency show a difference of only 0 - 5 %.

Figures 6.23a and 6.23b shows the system temperatures and the relevant heat fluxes if both the heat source and the pump are turned off, which is known as the rest mode.



(a) System Temperature vs. Satellite Frame Temperature. (b) Heat Flows vs. Satellite Frame Temperature.

Figure 6.23: Equilibrium Temperatures (left) and Heat Flows (right) vs. Satellite Frame Temperature during Idle Mode.

If the fluid is not being circulated using the pump, it can be seen that the difference in temperature between the heat source and heat sink is higher compared to the operational mode, where

the pump is turned on. This can be explained by the increase in thermal resistance between these two points in the system when the fluid is not circulating but is stationary instead.

Another difference between rest mode and operational mode is that the temperatures in rest mode are lower. This is a logical consequence of less heat being added into the system when the heat source and the pump are turned off.

A consequence of the temperature of the system being lower is that the temperature at the heat sink is lower than the frame temperature, which causes heat to flow from the frame into the radiator plate. This phenomenon is represented by the negative heat flux into the frame in Figure 6.23b. Since more energy is entering the system from the frame than it is leaving the system into the frame, the only net energy outgoing source is the radiation into space at the radiator plate. Therefore, the total input power is equal to the radiator radiation.

7 Conclusion

During this research, a design is created for an in-orbit demonstration of a mechanically pumped cooling loop that facilitates a micro-pump designed by Demcon Kryoz and NLR. The goal of the in-orbit demonstration is to create a manner of testing the performance of the micro-pump in a space environment, since the pump has only been tested in ambient conditions at the time of writing. To arrive at a final design that is able to cope with the launching loads and the harsh conditions of space, the full design process is carried out. Starting at the requirements, boundary conditions are set. These boundary conditions lead to concepts that shape the simplified build-up of the design and create a structured overview of the main challenges that have to be faced. In the detailed design phase that follows, these challenges are tackled one by one to gain increasingly more information about the limits and possibilities of the project. Finally, a system analysis is carried out that creates an overview of the expected performance of the in-orbit demonstration. By comparing this expected performance to the set requirements at the start of the design process, it becomes clear whether the design is ready to be built and tested or whether some aspects need more thorough inspection.

All requirements stated in Chapter 3 are analysed for completion in Chapters 5 and 6 and are used as the basis of the conclusion. The final design of the in-orbit demonstration contains all components specified in the requirements to build the coherent system that was envisioned at the start of the process. All these components are located and oriented as described in the requirements and are designed to fit within the 1U volume while being compatible with the GOMSpace 6U structure assembly hole patterns. Additionally, the final design, including the weight of the fluid, has a total weight of approximately 715 g, which is compliant with the maximum weight requirement of 1.0 kg. The temperature sensors are designed to be placed in critical locations to monitor the system and to compare the real-life tests to the simulations.

The fluidic components of the system are designed to withstand pressure build-up when the accumulator reaches its highest allowable temperature of 95 °C. This temperature relates to a vapour pressure of 3.3 bar, which indicates that the system pressure will never exceed a pressure of 4 bar. To fill the system, a reversible filling interface is added to the fluidic design.

The in-orbit demonstration is shown to withstand the sine- and random vibrations that it is subjected to during its lifetime with a positive yield margin.

At a flow rate of $0.7 \frac{\text{g}}{\text{s}}$, the total pressure drop of the fluidic loop is 3.4 mbar at the minimum system temperature of -40 °C. This pressure drop suits the micro-pump well since it is capable of operating with pressure drops of an order of magnitude higher.

In the worst-case scenario, when all electric components are powered on, the system uses between 4.65 and 6.6 Wh of energy per orbit depending on the temperature of the satellite frame. This power consumption complies with the maximum power usage requirement of 7.5 Wh per orbit. In operational mode, when using a heat source of 3.0 W, the amount of incoming energy that leaves the system through radiation at the radiator plate is between 2.5 and 3.3 W, which amounts to approximately 54 - 75 % of the total input power depending on the satellite frame temperature. Moreover, the system is expected to never reach a temperature above 85 °C, while never dropping below -40 °C, which ensures that all components in the system will never experience temperature-related issues. Therefore, the design is proven to never overheat, even when all electronic components are powered on.

Overall the design of the in-orbit demonstration is shown to provide a manner of testing the performance of the micro-pump developed by NLR and Demcon in a space environment. This will be a step in the right direction for Demcon Kryoz to broaden their knowledge in providing space-proof systems to their customers.

8 Discussion

The main findings of the mechanical analysis of the final design are that the design is shown to withstand the internal pressure build-up and the sine- and random vibrations that it is subjected to during its lifetime. The resistance of the structure to shock- and quasi-static vibrations could not be further examined due to a lack of computing power, which limits the mechanical analysis to not feature all vibration types that the design is subjected to. The same computing power limitation limits the amount of mesh elements that can be used during the vibrational analysis. This might cause the stresses found in this analysis to be marginally off compared to the stresses found in reality. Additionally, the found stresses in the random vibrations show to be at their maximum around weld lines. This could be caused by the absence of the additional weld material, which causes stress singularities at these weld interfaces. To avoid these singularities, the weld material could be added to the CAD model to add additional stiffness. The vibrational analyses could be performed using a cluster that harnesses more computing power to be able to perform the transient shock- and quasi-static vibrations and to perform the simulations with a finer mesh.

In the fluidic analysis, the maximum pressure drop over the entire system is found to be 3.4 bar, which is significantly less than the pressure drop of 25 mbar at which the micro-pump is able to deliver a flow rate of $0.7 \frac{\text{g}}{\text{s}}$ according to the pump performance tests. The findings of these calculations are all based on the limited information that is available about the used working fluid. Therefore, to make sure that the calculations represent reality, more information should be found on the working fluid properties. Since this information, like the exact temperature and pressure dependence of several fluid properties, is not available on the internet, experiments would have to be performed. Another option could be to pick a working fluid of which the full temperature and pressure dependence of all fluidic properties is known.

Additionally, the fluidic analysis is limited to steady laminar flow, since there will be no turbulent flow throughout the fluidic components. However, if an additional pump would be used or if the tubing size would be decreased, turbulent flow might occur, which would make the analysis insufficient.

One of the main findings of the thermal analysis is that the system will never exceed the temperature range boundaries in operational mode and idle mode. Moreover, the percentage of power that is dissipated by the system through the radiator plate is between 50% and 85% dependent on the satellite frame temperature and the heat source power. These findings are based on the assumption that the system will only radiate energy into space at the radiator surface since the rest of the system is shielded by MLI. In reality, this ideal insulation is hard to reach, but if the right MLI material is used in the correct manner, the radiation shielding can get close to 100%. Moreover, both the simplified thermal network and the simulation use multiple simplifications that are not exactly equal to reality. In the case of the simplified thermal network, each component is assumed to be at a constant temperature throughout its entire body, which is not exactly the case in reality. The thermal simulation in Ansys assumes that the fluid is a solid with a very high conductivity that mimics its thermal resistance as if it were flowing. This is not exactly similar to reality, but since both the simplified calculations and the simulations show similar results, the outcomes are likely to be accurate.

A general point that requires more attention is the detailed selection of MLI material. By selecting the MLI material, the radiative behaviour of the design can be set in stone, which allows for more conclusive claims about the thermal behaviour of the design.

Another group of components that requires more attention are the fasteners. Especially the bolted connections could be further analysed to make sure that they offer the required pre-

tension at a specified torque. Additionally, a glue could be selected that is used to make sure that the bolts do not come loose when subjected to vibrations.

Finally, the micro-pump requires further studying to accurately predict its performance before sending it into space. In this research, the micro-pump is treated as a black box with a certain flow rate, which is not the case in reality. Only when the behaviour of the pump is fully understood, can the performance of the in-orbit demonstration be accurately predicted.

9 References

- [1] M. Lifson, A. D'Ambrosio, D. Arnas, and R. Linares, "How many satellites can we fit in low earth orbit?: Capacity integrating risk-based and intrinsic methods," 2022.
- [2] M. Swartwout, "Cubesats/smallsats/nanosats/picosats/rideshare(sats) in 2022: Making sense of the numbers," pp. 1–10, 2022.
- [3] J. D. Liddle, A. P. Holt, S. J. Jason, K. A. O'Donnell, and E. J. Stevens, "Space science with cubesats and nanosatellites," *Nature Astronomy*, vol. 4, pp. 1026 – 1030, 2020.
- [4] Kongsberg, "How many satellites are in space?." <https://nanoavionics.com/blog/how-many-satellites-are-in-space/#:~:text=As%20of%20May%20the%204th,satellites%20in%20various%20Earth%20orbits.>, 2023. Accessed: 09-12-2023.
- [5] NASA, "What are smallsats and cubesats?." <https://www.nasa.gov/what-are-smallsats-and-cubesats/>. Accessed: 09-12-2023.
- [6] A. Johnstone, "Cubesat design specification," *The Cubesat Program*, pp. 10 – 13, 2023.
- [7] Jet Propulsion Laboratory - California Institute of Technology, "Cubesats and smallsats: A new revolution in spacecraft." <https://www.jpl.nasa.gov/topics/cubesats>. Accessed: 23-06-2024.
- [8] Demcon, "About demcon: high-quality technology for our future." <https://demcon.com/about-demcon/>, 2024. Accessed: 21-02-2024.
- [9] Demcon Kryoz and NLR, "TN6 - Detailed design definition and justification file," 2024. Note: This is an internal document of Demcon and NLR.
- [10] Swagelok, "Stainless steel 1-piece 40g series ball valve, 1.4 cv, 1/4 in. swagelok tube fitting, red handle." <https://products.swagelok.com/en/c/2-way-straight-pattern/p/SS-43GS4-RD?q=:relevance:connection1Size:1%2F4+in.:connection1Type:Swagelok%C2%AE+Tube+Fitting:connection2Type:Swagelok%C2%AE+Tube+Fitting>. Accessed: 24-03-2024.
- [11] Beswick, "Quick disconnects quick couplers for fluid power designs." <https://www.beswick.com/catalog/product-category/quick-disconnects/>. Accessed: 28-03-2024.
- [12] Swagelok, "316 stainless steel tube socket weld male connector, 1/4 in. od x 1/4 in. male npt." <https://products.swagelok.com/en/c/straights/p/SS-4-TSW-1-4>. Accessed: 24-03-2024.
- [13] S. Tachikawa, H. Nagano, A. Ohnishi, and Y. Nagasaka, "Advanced passive thermal control materials and devices for spacecraft: A review," *International Journal of Thermophysics*, vol. 43, 06 2022.
- [14] D. L. Hartmann, "Chapter 2 - the global energy balance," in *Global Physical Climatology (Second Edition)* (D. L. Hartmann, ed.), pp. 25–48, Boston: Elsevier, second edition ed., 2016.
- [15] A. B. Uygur, "A complete methodology for the computation of external heat fluxes for the transient thermal analysis of satellites," *Journal of Aeronautics and Space Technologies*, vol. 11, pp. 17–27, 01 2018.
- [16] I. Martinez, "Radiative view factors." <http://imartinez.etsiae.upm.es/~isidoro/tc3/Radiation%20View%20factors.pdf>, 2015. Accessed: 20-01-2024.

- [17] J. Howell and M. P. Mengüç, “Radiative transfer configuration factor catalog: A listing of relations for common geometries,” *Journal of Quantitative Spectroscopy Radiative Transfer*, vol. 112, pp. 910–912, 2011.
- [18] Deimos-Space, “Cassini demcon radiator temperature.” Note: This is an internal document of Deimos.
- [19] S. Miller, “Tutorial on atomic oxygen effects and contamination,” 2017.
- [20] J. A. Dever, “Low earth orbital atomic oxygen and ultraviolet radiation effects on polymers,” 02 1991.
- [21] G. A. Zerlaut, J. E. Gilligan, and Y. Harada, “Stable white coatings,” 06 1965.
- [22] J. R. Grammer and G. R. Cunnigton, “Emissivity coatings for low-temperature space radiators,” 12 1966.
- [23] AZ-Technology, “Az-93 white thermal control, inorganic paint / coating.” <https://www.aztechnology.com/product/1/az-93>. Accessed: 24-06-2024.
- [24] T. Ganzeboom, J. van Es, L. Formisani, and S. Elvik, “Development of a miniature heat exchanger for mechanically pumped loop systems for active thermal control of cubesats,” 2022.
- [25] R. M. Manglik and A. E. Bergles, “Heat transfer and pressure drop correlations for the rectangular offset strip fin compact heat exchanger,” *Experimental Thermal and Fluid Science*, vol. 10, no. 2, pp. 171–180, 1995.
- [26] S. Ndao, Y. Peles, and M. K. Jensen, “Multi-objective thermal design optimization and comparative analysis of electronics cooling technologies,” *International Journal of Heat and Mass Transfer*, vol. 52, no. 19, pp. 4317–4326, 2009.
- [27] R. Darby, “Correlate pressure drops through pipe fittings (vol 106, pg 101, 1999),” *Chemical Engineering -New York- Mcgraw Hill Incorporated then Chemical Week Publishing Llc-*, vol. 106, pp. 9–9, 09 1999.
- [28] Swagelok, “Stainless steel swagelok tube fitting, tube socket weld elbow, 1/4 in. tube od x 1/4 in. tube socket weld.” <https://products.swagelok.com/en/c/90-degree-elbows/p/SS-400-9-4W?q=:relevance>. Accessed: 22-03-2024.
- [29] E. Shoemake, “The hyper lab tube fitting guide.” <https://hydrogen.wsu.edu/2016/10/10/the-hyper-lab-tube-fitting-guide/>, 2016. Accessed: 26-06-2024.
- [30] W. Terry, “Performance and compatibility of two brands of 1/4” compression tube fittings.” https://www.parker.com/literature/Instrumentation%20Products%20Division/TEST%20Documents/TEST_FSI_Report_%20ALOK.pdf. Accessed: 18-04-2024.
- [31] J. Amesz, “Conversion of leak flow-rates for various fluids and different pressure conditions,” 1966.
- [32] Zoppas-Industries, “Stock flexible heater for space market (satellite - vehicle - launcher and ground segment).” Note: This information is received from the supplier by mail.
- [33] DBK, “Ptc conductive heating elements.” <https://docs.rs-online.com/c0cd/0900766b81422503.pdf>. Accessed: 12-05-2024.
- [34] Omega-Engineering, “Polyimide film insulated flexible heaters.” <https://br.omega.com/omegaFiles/heaters/pdf/KHRA-KHLVA-KHA-SERIES.pdf>. Accessed: 12-05-2024.

- [35] Omega-Engineering, “Surface spot heaters.” <https://br.omega.com/omegaFiles/heaters/pdf/HPG.pdf>. Accessed: 12-05-2024.
- [36] RS-Pro, “Datasheet polyamide heating element.” <https://docs.rs-online.com/51ba/0900766b8158379d.pdf>. Accessed: 13-05-2024.
- [37] Minco, “Hap6944 - category: All-polyimide thermofoil heaters.” [https://www.minco.com/catalog/?catalogpage=search&cid=3_6-all-polyimide-thermofoil-heaters&filter=mounting%3A2%3ASilicone%20Adhesive%20\(%2312%20PSA\)#cde-attribute-mounting](https://www.minco.com/catalog/?catalogpage=search&cid=3_6-all-polyimide-thermofoil-heaters&filter=mounting%3A2%3ASilicone%20Adhesive%20(%2312%20PSA)#cde-attribute-mounting). Accessed: 13-05-2024.
- [38] Minco, “Maximum watt density.” <https://dpk3n3gg92jwt.cloudfront.net/domains/minco/pdf/Watt%20Density%20Chart%20Guide.pdf>. Accessed: 13-05-2024.
- [39] Minco, “Mounting thermofoil heaters thermal-ribbon sensors with 12 pressure-sensitive adhesive.” <https://dpk3n3gg92jwt.cloudfront.net/domains/minco/pdf/SPI%2000-0598%20Mounting%20Thermofoil%20Heaters%20&%20Thermal-Ribbon%20Sensors%20with-12%20Pressure-Sensitive%20Adhesive.pdf>. Accessed: 13-05-2024.
- [40] S. Kalra, B. Munjal, V. R. Singh, M. Mahajan, and B. Bhattacharya, “Investigations on the suitability of peek material under space environment conditions and its application in a parabolic space antenna,” *Advances in Space Research*, vol. 63, no. 12, pp. 4039–4045, 2019.
- [41] M. Rinaldi, F. Cecchini, L. Pigliaru, T. Ghidini, F. Lumaca, and F. Nanni, “Additive manufacturing of polyether ether ketone (peek) for space applications: A nanosat polymeric structure,” 2020.
- [42] M. Finckenor, “Multilayer insulation material guidelines.” <https://ntrs.nasa.gov/api/citations/19990047691/downloads/19990047691.pdf>, 1999. Accessed: 15-06-2024.
- [43] NASA Engineering and Safety Center, “Best practices for use of sine vibration testing.” [https://www.nasa.gov/wp-content/uploads/2015/04/nesc-tb-15-03-best-practices-for-use-of-sine-vibration-testing.pdf?emrc=64c792#:~:text=Sine%20Vibration%20\(SV\)%20Testing%20involves,but%20mainly%20on%20flight%20articles](https://www.nasa.gov/wp-content/uploads/2015/04/nesc-tb-15-03-best-practices-for-use-of-sine-vibration-testing.pdf?emrc=64c792#:~:text=Sine%20Vibration%20(SV)%20Testing%20involves,but%20mainly%20on%20flight%20articles). Accessed: 07-05-2024.
- [44] B. Wang, W. Shi, and Z. Miao, “Confidence analysis of standard deviational ellipse and its extension into higher dimensional euclidean space,” *PloS one*, vol. 10, p. e0118537, 03 2015.
- [45] NASA, “Sine-burst load test.” <https://llis.nasa.gov/lesson/730>. Accessed: 11-05-2024.
- [46] NASA Engineering and Safety Center, “Best practices for use of sine burst testing.” [https://www.nasa.gov/wp-content/uploads/2015/04/nesc-tb-15-02-best-practices-for-use-of-sine-burst-testing.pdf?emrc=e1924f#:~:text=Sine%20Burst%20\(SB\)%20Testing%20is,the%20shaker%20for%20other%20tests](https://www.nasa.gov/wp-content/uploads/2015/04/nesc-tb-15-02-best-practices-for-use-of-sine-burst-testing.pdf?emrc=e1924f#:~:text=Sine%20Burst%20(SB)%20Testing%20is,the%20shaker%20for%20other%20tests). Accessed: 10-05-2024.
- [47] R. Powell, C. Y. Ho, and P. E. Liley, *Thermal conductivity of selected materials*, vol. 8. US Department of Commerce, National Bureau of Standards Washington, DC, 1966.
- [48] A. L. Woodcraft, “Recommended values for the thermal conductivity of aluminium of different purities in the cryogenic to room temperature range, and a comparison with copper,” *Cryogenics*, vol. 45, no. 9, pp. 626–636, 2005.
- [49] R. Bogaard, P. Desai, H. Li, and C. Ho, “Thermophysical properties of stainless steels,” *Thermochimica Acta*, vol. 218, pp. 373–393, 1993.

- [50] R. Powell and R. Tye, “The thermal and electrical conductivity of titanium and its alloys,” *Journal of the Less Common Metals*, vol. 3, no. 3, pp. 226–233, 1961.
- [51] J. Ekin, *Experimental Techniques for Low-Temperature Measurements*. 2006.
- [52] Alfafilters, “Sintered powder cup specifications.” Note: This information is received from the supplier by mail.
- [53] Solvay, “Galden ht pfpe - heat transfer fluids.” https://www.behlke.com/pdf/datasheets/galden_ht135.pdf. Accessed: 11-12-2024.

A Material and Component Properties

Table A.1: Overview of the Structural Materials present in the Final Design.

Material	Density [$\frac{\text{kg}}{\text{m}^3}$]	Brinell Hardness	Young's Modulus [GPa]	Ultimate Tensile Strength [MPa]	Yield Tensile Strength [MPa]	Specific Heat Capacity [$\frac{\text{J}}{\text{kg K}}$]	Thermal Conductivity [$\frac{\text{W}}{\text{m K}}$]	Thermal Expansion [$\frac{\mu\text{m}}{\text{m K}}$]
Aluminium (7075-T6)	3000	150	70	560	480	870	130	23
AlSi10Mg	2670	124	73 - 74	450	271 - 297	910 - 920	130 - 150	19 - 25.2
Stainless Steel (AISI 316)	8000	219	193	580	290	500	18.9	16.5
Titanium (Grade 2)	4510	200	103	344	276	523	16.4	8.6
Titanium (Grade 5)	4430	334	113.8	950	880	526	6.7	8.6
PEEK	1510	-	11.5	185	-	320	0.3	45

Table A.2: Overview of the Radiator Coating Properties. [23]

Thermal Emittance [-]	0.91 ± 0.02
Solar Absorptance [-]	0.15 ± 0.02
Temperature Range [°C]	-180 to 1400
Appearance / Color	Nonspecular white
Nominal Dry Thickness [μm]	127 ± 38
ASTM D3359A Adhesion Grade	Not less than 3A
Full Cure [days]	7

Table A.3: Overview of Wick Material Properties. [52]

Filter Grade	Porosity [%]	Permeability Coefficients [m^2]		Grade Efficiency [μm]	Bubble- Point Pressure [Pa]	Ring Tensile Strength [MPa]
	ϵ	α	β	$X_{T=98\%}$	BP	R_m
XLKA-R 0.5/S	17	0.05	0.01	3.2	13000	180
XLKA-R 1/S	20	0.15	0.06	4.3	10000	140
XLKA-R 3/S	31	0.55	0.56	5.1	5800	110
XLKA-R 5/S	30	0.80	0.90	6.5	4700	100
XLKA-R 8/S	30	1.20	1.20	8.7	4100	90
XLKA-R 10/S	32	1.80	1.70	12.6	3000	80
XLKA-R 15/S	36	4.00	11.00	18.4	1900	60
XLKA-R 20/S	45	10.00	30.00	23.9	1700	55
XLKA-R 30/S	44	17.00	25.00	38.0	1100	50
XLKA-R 50/S	44	25.00	32.00	45.0	800	35
XLKA-R 80/S	48	40.00	50.00	78.0	700	17
XLKA-R 100/S	45	65.00	93.00	92.0	550	15
XLKA-R 150/S	44	150.00	110.00	132.0	400	10
XLKA-R 200/S	54	258.00	137.00	173.0	350	5
Applied Standard	DIN-ISO 30911-3	DIN-ISO 4022		ASTM F795	ISO 4003	DIN-ISO 30911-6

B Fluid Properties

Table B.1: General Specifications for the different Galden Fluids at 25 °C and Atmospheric Pressure. [53]

Properties	HT55	HT70	HT80	HT110	HT135	HT170	HT200	HT230	HT270
Boiling Point [°C]	55	70	80	110	135	170	200	230	270
Pour Point [°C]	< -125	< -110	-110	-100	-100	-97	-85	-77	-66
Density [$\frac{g}{cm^3}$]	1.65	1.68	1.69	1.71	1.72	1.77	1.79	1.82	1.85
Kinematic Viscosity [cSt]	0.45	0.50	0.57	0.77	1.00	1.80	2.40	4.40	14.00
Vapor Pressure [torr]	225	141	105	17	5.8	0.8	0.2	0.03	< 10 ⁻²
Specific Heat [$\frac{cal}{g \cdot ^\circ C}$]	0.23	0.23	0.23	0.23	0.23	0.23	0.23	0.23	0.23
Heat of Vaporization at Boiling Point [$\frac{cal}{g}$]	22	17	17	17	16	16	15	15	15
Refractive Index	1.280	1.280	1.280	1.280	1.280	1.280	1.281	1.283	1.283
Coefficient of Thermal Expansion	0.0011	0.0011	0.0011	0.0011	0.0011	0.0011	0.0011	0.0011	0.0011
Surface Tension [$\frac{dyne}{cm}$]	14	14	16	16	17	18	19	19	20
Thermal Conductivity [$\frac{W}{m \cdot K}$]	0.065	0.065	0.065	0.065	0.065	0.065	0.065	0.065	0.065
Dielectric Strength [kV] (2.54 mm gap)	40	40	40	40	40	40	40	40	40
Dielectric Constant [-]	1.86	1.86	1.89	1.92	1.92	1.94	1.94	1.94	1.94
Volume Resistivity [$\Omega \cdot cm$]	1 · 10 ¹²	1 · 10 ¹⁵	1.5 · 10 ¹⁵	1.5 · 10 ¹⁵	1.5 · 10 ¹⁵	1.5 · 10 ¹⁵	6 · 10 ¹⁵	6 · 10 ¹⁵	6 · 10 ¹⁵
Average Molecular Weight [amu]	340	410	430	580	610	760	870	1020	1550
Dissipation Factor [-]	2 · 10 ⁻⁴	2 · 10 ⁻⁴	2 · 10 ⁻⁴	2 · 10 ⁻⁴	2 · 10 ⁻⁴	2 · 10 ⁻⁴	2 · 10 ⁻⁴	2 · 10 ⁻⁴	2 · 10 ⁻⁴
Solubility of Water (wt) [ppm]	< 10	< 10	< 10	< 10	< 10	< 10	< 10	< 10	< 10
Solubility of Air [$\frac{cm^3 \text{ gas}}{100cm^3 \text{ liquid}}$]	26	26	26	26	26	26	26	26	26

Suggested operating temperature range

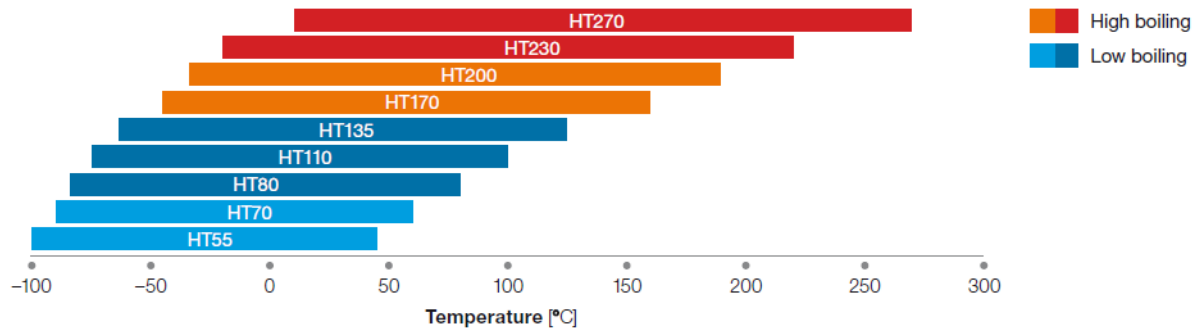


Figure B.1: Operating Temperature Range for the different Galden Fluids at Atmospheric Pressure. [53]

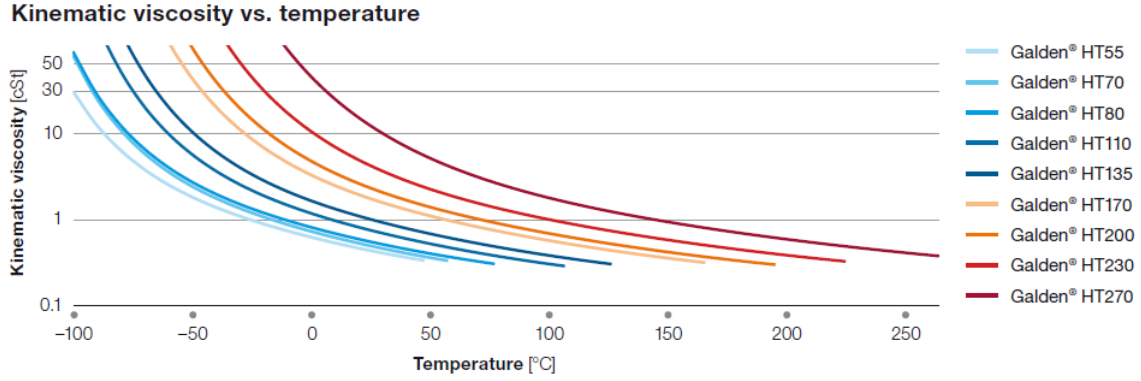


Figure B.2: Viscosity vs. Temperature for different Galden Fluids at Atmospheric Pressure. [53]

C Accumulator Heater Specifications

Table C.1: General Component Specifications of the Accumulator Heater. [32]

Insulation Material	Polyimide + Acrylic
Resistance Tolerance	+/- 10%
Reference Maximum Power Density at 100°C [$\frac{W}{cm^2}$]	1.0 (*)
Type	Single Layer, Single Circuit
Thickness [mm]	max 0.2
Patch	Acrylic, Exit Side Type A
Welded Wires	FM: 3901-020-03 AWG 25, Red, Unshielded, $L_c = 500$ mm QM: MIL 22759/11 AWG 26, Red, Unshielded, $L_c = 500$ mm
Minimum Operating Temperature [°C]	- 65
Maximum Operating Temperature [°C]	150
Optional Layers	PSA Adhesive Layer
RoHS	Compliant
Minimum Bending Radius [mm]	1.0
(*) Please note that the maximum power density is both application and design specific, and the indicated value is intended to be applied to the heater when correctly mounted, respecting all provided instructions in the applicable conditions. Moreover, please also note that voltage and wattage values indicated in the Table are for reference only: you can apply whichever lever your mission needs, pending that the maximum operating temperature indicated in the technical drawing (and applicable derating rules, if any) is not exceeded.	
(**) ECSS-Q-ST-30-11C for ESCCH	

Table C.2: Different Size Options of the Accumulator Heater. [32]

P/N QM Heaters	P/N FM Heaters	Size Y [mm]	Size X [mm]	Lead Exit Size [mm x mm]	Net Heating Area [cm ²]	Resistance [Ω]	Wire Length [mm]	Typical Power @ 28 V [W]
SC012037Q	SC012037F	12.5	37.5	10 x 11	2.63	313.6	500.0	2.5
SC012075Q	SC012075F	12.5	75.0	10 x 11	6.56	247.2	500.0	3.2
SC012125Q	SC012125F	12.5	125.0	10 x 11	11.81	139.4	500.0	5.6
SC025025Q	SC025025F	25.0	25.0	10 x 14	3.61	392.0	500.0	2.0
SC025037Q	SC025037F	25.0	37.5	10 x 14	6.49	239.1	500.0	3.3
SC025050Q	SC025050F	25.0	50.0	10 x 14	9.36	172.0	500.0	4.6
SC025075Q	SC025075F	25.0	75.0	10 x 14	15.29	110.2	500.0	7.1
SC025100Q	SC025100F	25.0	100.0	10 x 14	20.97	81.1	500.0	9.7
SC037037Q	SC037037F	37.5	37.5	10 x 14	11.18	150.1	500.0	5.2
SC037050Q	SC037050F	37.5	50.0	10 x 14	15.44	109.4	500.0	7.2
SC037100Q	SC037100F	37.5	100.0	10 x 14	33.27	52.5	500.0	14.9
SC050050Q	SC050050F	50.0	50.0	10 x 14	21.36	80.2	500.0	9.8
SC050075Q	SC050075F	50.0	75.0	10 x 14	33.36	52.3	500.0	15.0

D 3-K Method Loss Coefficients

Table D.1: Overview of the Loss Factors for different types of Fittings. [27]

Category	Fitting		(L/D_{eq})	K_m	K_i	K_d
Elbows - 90 Degrees	Threaded, Standard	$r/D = 1.0$	30	800	0.14	4.0
	Threaded, Long Radius	$r/D = 1.5$	16	800	0.071	4.2
	Flanged, Welded, Bend	$r/D = 1.0$	20	800	0.091	4.0
	Flanged, Welded, Bend	$r/D = 2.0$	12	800	0.056	3.9
	Flanged, Welded, Bend	$r/D = 4.0$	14	800	0.066	3.9
	Flanged, Welded, Bend	$r/D = 6.0$	17	800	0.075	4.2
	Mitered	1 Weld, 90 Degrees	60	1000	0.27	4.0
	Mitered	2 Welds, 45 Degrees	15	800	0.068	4.1
	Mitered	3 Welds, 30 Degrees	8	800	0.035	4.2
Elbows - 45 Degrees	Threaded, Standard	$r/D = 1.0$	16	500	0.071	4.2
	Long Radius	$r/D = 1.5$	None	500	0.052	4.0
	Mitered, 1 Weld	45 Degrees	15	500	0.086	4.0
	Mitered, 2 Welds	22.5 Degrees	6	500	0.052	4.0
Elbows - 180 Degrees	Threaded, Close Return Bend	$r/D = 1.0$	50	1000	0.23	4.0
	Flanged	$r/D = 1.0$	None	1000	0.12	4.0
	All	$r/D = 1.5$	None	1000	0.10	4.0
Tees	Through-branch (as elbow)					
	Threaded	$r/D = 1.0$	60	500	0.274	4.0
	Threaded	$r/D = 1.5$	None	800	0.14	4.0
	Flanged	$r/D = 1.0$	20	800	0.28	4.0
	Stub-in Branch		None	1000	0.34	4.0
	Run Trough Threaded	$r/D = 1.0$	20	200	0.091	4.0
	Flanged	$r/D = 1.0$	None	150	0.017	4.0
	Stub-in Branch		None	100	0.0	0.0